

國立交通大學

材料科學與工程學系

博士論文

利用原子層化學氣相法在 TiO_2 電極上沉積 Al_2O_3 覆層
以改進染料敏化太陽能電池之光電效能

Atomic layer deposition of an Al_2O_3 overlayer on the TiO_2 electrode
to improve
the photovoltaic performance of dye sensitized solar cells



研究生：田大昌

指導教授：潘扶民 教授

中華民國一百年六月

利用原子層化學氣相法在 TiO_2 電極上沉積 Al_2O_3 覆層
以改進染料敏化太陽能電池之光電效能

Atomic layer deposition of an Al_2O_3 overlayer on the TiO_2 electrode to improve
the photovoltaic performance of dye sensitized solar cells

研 究 生：田大昌

Student : Ta-Chang Tien

指導教授：潘扶民

Advisor : Fu-Ming Pan

國 立 交 通 大 學
材 料 科 學 與 工 程 學 系
博 士 論 文



Submitted to Department of Materials Science and Engineering
College of Engineering

National Chiao Tung University

in partial Fulfillment of the Requirements

for the Degree of

Doctor of Philosophy

in

Materials Science and Engineering

Jun 2011

Hsinchu, Taiwan, Republic of China

中華民國一 百 年 六 月

利用原子層化學氣相法在 TiO_2 電極上沉積 Al_2O_3 覆層

以改進染料敏化太陽能電池之光電效能

學生：田大昌

指導教授：潘扶民

國立交通大學

材料科學與工程學系博士班

摘 要

本論文研究原子層沉積法在染料敏化太陽電池之二氧化鈦電極鍍上超薄之氧化鋁膜層。此太陽電池之效率(PCE)因二氧化鈦電極鍍上一層約 0.2 nm 厚之氧化鋁而從 5.75%增加到 6.5%，比未鍍氧化鋁時之效率增進了 13%。在本研究中，我們研究了此太陽電池之氧化鋁(殼)/二氧化鈦(核)電極之能階、覆蓋率與成長模式三大題目。主要成果依序敘述如下：

我們發現介面 Ti-O-Al(OH)_2 及極性層對氧化鋁/二氧化鈦電極之功函數有極大之影響，且氧化鋁厚度愈厚則氧化鋁/二氧化鈦電極之價電子能帶最大值及能隙就愈接近氧化鋁體材之值。在效率最大時，其介面功函數差距為 0.4 eV，介面復合能障為 0.1 eV。當氧化鋁厚度愈厚時因為穿隧效應則效率大幅下降，此太陽電池之效率增加時，因超薄氧化鋁之適宜能階而使得

電子傳輸過程中並沒有穿隧效應之發生，因此，我們提出了介面功函數差距、介面復合能障及介面能障等參數與此材料之效率提升之新看法。此外，也確認介面 Ti-O-Al(OH)_2 及極性層對氧化鋁/二氧化鈦電極之影響。

此外，我們建立了一覆蓋率之計算模型以測量染料敏化太陽電池之殼/核電極之覆蓋率，我們利用光電子能譜儀分析此殼/核電極之奈米二氧化鈦顆粒，確認此模型可應用在染料敏化太陽電池之氧化鋁/二氧化鈦電極之覆蓋率計算。結果顯示氧化鋁之覆蓋率隨其厚度及反應循環次數增加而增加，且以原子沉積法鍍上之氧化鋁膜層呈現島狀成長模式。而此太電最高之轉換效率出現在氧化鋁覆蓋率值為 0.25 時，顯示此太電電極若鍍上單原子層之氧化鋁且其覆蓋率值為 1 時，可能有機會增加其原太電轉換效率之 52%。

最後，我們發現此研究中之氧化鋁膜層之成長模式在 ALD 反應次數為 5 次以上時，特別是在銳鈦礦之二氧化鈦電極上會開始從島狀成長轉換成層狀成長。我們推論這是因為受到奈米二氧化鈦顆粒之壓應力減少之影響，而我們也證實了壓應力隨著 ALD 反應次數增加而減少，也導致了島狀成長轉換成層狀成長之狀況發生。

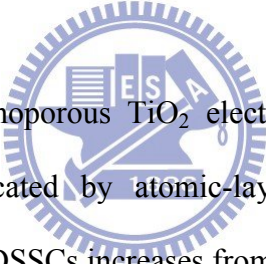
Atomic layer deposition of an Al₂O₃ overlayer on the TiO₂ electrode to improve the photovoltaic performance of dye sensitized solar cells

Student : Ta-Chang Tien

Advisors : Dr. Fu-Ming Pan

Department of Materials Science and Engineering
National Chiao Tung University

Abstract



Ultra-thin Al₂O₃ films on nanoporous TiO₂ electrodes of dye-sensitized solar cells (DSSCs) were successfully fabricated by atomic-layer-deposition (ALD). The power conversion efficiency (PCE) of the DSSCs increases from 5.75% to 6.5%, an improvement of 13%, when the Al₂O₃ overlayer reaches an average thickness of ~0.2 nm. The thesis focused three interfacial issues regarding the Al₂O₃/ TiO₂ electrode; they are (a) the determination of energy levels of the Al₂O₃ overlayer, (b) analysis of the surface coverage of the as a function of the ALD conditions, and (c) study of the growth mode of the core/shell electrode.

The formation of Ti-O-Al(OH)₂ and interfacial dipole layers exhibits a strong influence on the work function of the Al₂O₃ overlayers. As the Al₂O₃ overlayer becomes thicker and thicker, the valence band maximum and the band gap gradually approach the values characteristic of pure Al₂O₃. The one-monolayer thick Al₂O₃ overlayer has a maximum PCE, and a work function difference of 0.4 eV and a recombination barrier height of 0.1 eV were found. However, as the Al₂O₃ overlayer is thicker than one monolayer, the PCE decrease

significantly and the interfacial energy barrier height between the N719 dyes and TiO₂ electrode increases. We found that the electron transfer from the dye to the TiO₂ required no energy barrier as a result of the modification of interfacial energy levels due to the ultra-thin Al₂O₃ overlayer and, therefore, improved the PCE of the cell. The interfacial energy levels depends on the work function difference, the recombination barrier height and the interfacial barrier height, which are a function of the thickness of the Al₂O₃ overlayer and interfacial properties, such as the formation of the Ti-O-Al(OH)₂ moiety and the dipole layer. Proper modifications of the interfacial energy levels may result in an optimal performance of the dye-sensitized TiO₂ solar cell.

We proposed a core/shell (C/S) model to determine the surface coverage of an Al₂O₃ overlayer deposited on TiO₂ nanoparticles by XPS. We used the model to estimate the coverage of the Al₂O₃ shell layer on the nanoporous TiO₂ electrode of the DSSCs as a function of the number of ALD reaction cycles. By analyzing the XPS signals of the TiO₂ electrode with the Al₂O₃ coverage increasing from 0.25 to 1.0, we found that the ALD-Al₂O₃ deposition on the nanoporous TiO₂ electrode was via the island growth mode. On the basis of the coverage analysis, we predict that improvement in the PCE of ~52% is obtainable when a uniform monolayer of ALD-Al₂O₃ (i.e. at the coverage of 1.0) is deposited on the nanoporous TiO₂ electrode.

To understand why the ALD-Al₂O₃ deposition on TiO₂ nanoparticles is via the island growth mode, we used XPS and x-ray diffractometry (XRD) to study the chemical and microstructure properties of the interface between the ALD-Al₂O₃ overlayer and the TiO₂ nanoparticle as a function of the thickness of the ALD-Al₂O₃ overlayer, which was used to derive the growth per cycle of the ALD reaction. The growth mode of the ALD-Al₂O₃ overlayers changes from the island growth to the layer-by-layer growth after the first 5 ALD reaction cycles, and the growth mode transition is much more pronounced for the anatase

electrode layer. We suggest that the growth transition of the ALD- Al_2O_3 overlayer is correlated with the reduction in the lattice strain of the TiO_2 nanoparticle. The contractive lattice strain in the hydroxylated TiO_2 nanoparticle progressively decreases during the ALD Al_2O_3 deposition, resulting in the growth mode transition.



Acknowledgements

在此論文完成之際，有著當初恩師 潘扶民收本人為學生時一樣之愉悅，原因是恩師不僅為本人在工作上之前輩，如今也成為學生完成學業之指導教授，讓學生倍感榮耀。謹在此特別感謝吾師 潘扶民 教授七年來悉心教導，使學生得以完成博士論文及學業。

此外，感謝工研院王麗萍博士對本研究之啟發，使本人得以完成本論文。

感謝台灣大學材料系蔡豐羽教授、林偉同學提供鍍膜儀器與技術。

感謝工研院同仁李佳樺、陳淑貞、陳湘芸提供太電製作與分析技術。

感謝工研院同仁黃啟貞、蔡玲娜在此七年內分擔本人之院內工作。

感謝工研院長官洪健龍、蘇宗榮、蔡松雨、林麗娟提供行政上之資源。

感謝父親、母親、妻子多年來之照顧。

感謝口試委員之指教，讓本論文臻於至善。

最後感謝交通大學及工研院之培養，使本人得以渡過此七年之博士研究。

謹將此論文獻給我親愛之家人、師長與朋友。

Contents

Abstract (in Chinese)	i
Abstract (in English)	iii
Acknowledgements	vi
Contents	vii
Table Caption	x
Figure Caption	xi
List of Symbols	xvii
Chapter 1 Introduction	1
1.1 The Challenge for Photovoltaic Devices	1
1.2 The Importance of Dye-Sensitized Solar Cells	3
1.3 Enhancing the DSSC Efficiency with Core/Shell Electrodes	6
1.4 Objectives and Arrangements of the Study	8
Chapter 2 Literature Review	10
2.1 Solar Energy and Power Conversion Efficiency	10
2.1.1 Air Mass	10
2.1.2 Power Conversion Efficiency	12
2.1.3 Standard Measurement of PCE	13
2.2 Developments in Dye-Sensitized Solar Cells	14
2.2.1 Evolution of Dye-Sensitized Solar Cells	14
2.2.2 Operational Principles of Dye-Sensitized Solar Cells	15
2.2.3 Surface Area of the Nano-Crystalline Electrodes	18
2.3 Core/Shell Electrodes in DSSCs	19

2.3.1 Operational Principles of Core/Shell Electrodes-----	21
2.3.2 The Materials of Electrodes with Shell Structure-----	26
2.3.2.1 TiO ₂ Electrodes with Shell Structures-----	27
2.3.2.2 SnO ₂ Electrodes with Shell Structure -----	30
2.3.2.3 ZnO Electrodes with Shell Structure-----	32
2.3.2.4 Atomic Layer Deposited Al ₂ O ₃ Shells -----	34
2.4 Interfacial Studies of Nanoporous TiO ₂ Electrodes-----	37
2.4.1 Energy Levels of Dye/Electrode Interface -----	37
2.4.2 Coverage of Adsorbed Materials on Electrodes -----	41
2.4.3 Growth Studies of Atomic Deposited Layers -----	42
Chapter 3 Experimental -----	44
3.1 Preparation of Porous TiO ₂ Electrodes-----	44
3.2 Fabrication of Al ₂ O ₃ Shell Layers-----	44
3.3 Cell Characterization -----	47
3.4 Characterization of the Core/Shell Electrodes-----	49
3.4.1 Ultraviolet Photoelectron Spectroscopy -----	50
3.4.2 X-Ray Photoelectron Spectroscopy-----	52
3.4.3 Reflective Electron Energy Loss Spectroscopy -----	53
3.4.4 Transmission Electron Microscopy-----	54
3.4.5 X-ray Diffraction-----	55
Chapter 4 Interfacial Energy Levels of Al₂O₃ Films on TiO₂ Electrodes of Dye-Sensitized Solar Cells-----	57
4.1 Microstructure and Chemical Analysis -----	57
4.2 Interfacial Energy Levels Analysis -----	60
4.3 Energy Level Alignment at the Interfaces of Al ₂ O ₃ / TiO ₂ Electrodes-----	65

4.4 Summary-----	70
Chapter 5 Coverage Analysis for the Core/Shell Electrode of Dye-Sensitized Solar Cells	
-----	72
5.1 Theoretical Model from the Signals of X-ray Photoelectrons -----	72
5.1.1 The Model for A Isolated Core/Shell Particle -----	74
5.1.2 The Model for Core/Shell Particles in Multi-Layers-----	78
5.2 Samples Description-----	85
5.3 Application of the Core/Shell Model on Nanoporous Electrode-----	88
5.4 Summary-----	93
Chapter 6 Growth of Al₂O₃ Deposited on TiO₂ Electrodes of Dye-Sensitized Solar Cells	
-----	95
6.1 Deposition of the Al ₂ O ₃ Overlayers-----	95
6.2 Growth-Per-Cycle of the Al ₂ O ₃ Overlayers-----	99
6.3 Lattice Volumes of TiO ₂ Electrodes-----	101
6.4 Summary-----	105
Chapter 7 Conclusions and Future Works -----	107
7.1 Conclusions-----	107
7.2 Future Works-----	109
References -----	110
Vita -----	116

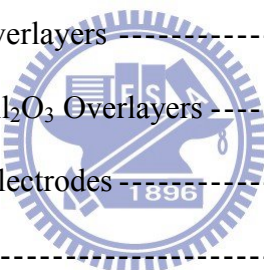


Table Caption

Table 1-1 The relative electric power cost generated by various resources [1]. -----	2
Table 2-1 Summary of the performances of DSSCs with TiO ₂ -core/shell electrodes for PCE values greater than or equal to 5.0 % from previous studies [12-23]. -----	28
Table 2-2 Summary of the performances of DSSCs with SnO ₂ -core/shell electrodes [24-31].	31
Table 2-3 Summary of the performances of DSSCs with SnO ₂ -core/shell electrodes from reference [25]. -----	32
Table 2-4. Summary of the performances of DSSCs with ZnO-core/shell electrodes [32-37].	33
Table 4-1 XPS results of the ALD Al ₂ O ₃ overlayers on TiO ₂ electrodes. -----	60
Table 4-2 Thickness, energy levels of the ALD Al ₂ O ₃ overlayers of the DSSCs.-----	61
Table 4-3 Cell performance of the DSSCs containing the ALD Al ₂ O ₃ overlayers with different thickness. -----	68
Table 5-1 Thickness and deposition rate of the ALD Al ₂ O ₃ shell layers on TiO ₂ electrodes.-	87
Table 6-1 Average thicknesses and deposition rates of ALD Al ₂ O ₃ overlayers on TiO ₂ electrodes.-----	98
Table 6-2 Lattice constants and lattice volumes of TiO ₂ electrodes for various numbers of ALD Al ₂ O ₃ deposition cycles. -----	102

Figure Caption

Figure 1.1 The remaining exploitable global resources in term of years [1]. -----	1
Figure 1.2 The developing trend for the low cost of solar cells shows the DSSC as the main solar cell in 2020 to 2030 [7]. -----	4
Figure 1.3 Number of (a) publications published per year, and (b) patents submitted, obtained from a simple and limited literature search using the keywords “dye-sensitized” and “solar” [6]. -----	5
Figure 1.4 Dye-Sensitized Solar Cell(DSSC)'s annual production and growth rate forecasting [9]. -----	6
Figure 1.5 (a) the efficiency of DSSCs and (b) the percent increase in PCE of DSSCs with TiO ₂ [12-23], SnO ₂ [24-31], ZnO [32-37]–core/shell electrodes from 2001 to 2011. Asterisks denote the shell layers in top-ten values. -----	7
Figure 2.1 Illustration of the path length of solar radiation and the zenith angle ϕ . -----	11
Figure 2.2 Photon flux of the AM 1.5 G spectrum at 1000 W/m ² and calculated accumulated photocurrent (ASTM G173-03). -----	11
Figure 2.3 Typical shape of the current-voltage curve of a solar cell. -----	12
Figure 2.4 Spectral irradiance for AM 1.5 G reference spectrum (IEC 60904-3) and the typical source irradiance of an Oriel 150 W solar simulator. Intensities of the spectra have been normalized to 100 mW/cm ² [41].-----	14
Figure 2.5 Energy band diagram of a typical DSSC employing an iodide/triiodide-based redox eletrolyte and N719 as a sensitizer dye [49]. -----	16
Figure 2.6 Illustrations comparing the operational principles of a (a) conventional DSSC and (b) Type II DSSC [52].-----	18

Figure 2.7 Comparison of the incident wavelength to charge carrier efficiency (ICPE) of dye-sensitized solar cell with (a) flat electrode and (b) nano-crystalline electrode [5].	19
Figure 2.8 Core/shell structures used in DSSCs. (a) The shell layer is formed prior to the film deposition, (b) the shell layer is coated after the film deposition [54].	20
Figure 2.9 A schematic view of the new nanoporous electrode which consists of a nanoporous TiO ₂ matrix covered with a thin layer of Nb ₂ O ₅ [11].	21
Figure 2.10 Illustration of the interfacial charge-transfer processes occurring at the nanostructure TiO ₂ /dye/electrolyte interface of DSSC [56].	22
Figure 2.11 Energy diagram representing the movement of (a) the TiO ₂ conduction band by the SrTiO ₃ coating and (b) the effect of the band shift at applied potential indicated the coated system is more resistive than the bare electrode [57].	24
Figure 2.12 Schematic drawing of a CSSC with a SrTiO ₃ barrier layer (left). The band diagram shows the different electron-transfer processes (right) [52].	25
Figure 2.13 The band diagrams show the band gap (E _g) before passivation (right) and after passivation (left). A larger band gap could further suppress more electron recombination [57].	26
Figure 2.14 The band positions of photo-semiconductors in contact with electrolyte at PH 1 [5].	27
Figure 2.15 A relation between V _{oc} change and the isoelectric point (IEP) of shell materials on TiO ₂ [55].	30
Figure 2.16. Illustrations showing (a) ZnO aggregates with dye molecules, (b) ZnO nanocrystallites withg micropores, (c) thin ALD-TiO ₂ layer on ZnO nanocrystallites, (d) enlarged schematic of (c), and (e) SEM of the aggregates of ZnO nanocrystallites, (f) SEM of the aggregates of ZnO nanocrystallites coated with	

thin TiO ₂ layer [36].-----	34
Figure 2.17 SEM images of the bilayer TiO ₂ electrodes before and after application of a 1 nm ALD Al ₂ O ₃ overlayer: (a) the scattering layer before ALD; (b) the scattering layer after ALD; (c) the nanoporous layer before ALD; (d) the nanoporous layer after ALD [14].-----	36
Figure 2.18 Energy diagram of ZnPcGly-dye/TiO ₂ interface determined from XPS and UPS measurements [73].-----	38
Figure 2.19 The A and B configurations of the N719 dye adsorbed on the TiO ₂ nanoparticle [75].-----	38
Figure 2.20 The possible type of dipole layers (a1) and (a2): Charge transfer across the interface, (b) Concentration of electrons in the adsorbate, (c) Rearrangement of electron cloud at the metal surface, (d) Chemical interaction, (e) Interface state introduced as a buffer of charge carriers, (f) Polar molecules or functional groups [76].-----	39
Figure 2.21 The changes of (a) work function (WF) measured by UPS, (b) CPD measured by Kelvin probe, (c) O 1s XPS peak and (d) Al 2p XPS peak in the Song et al. study [77].-----	40
Figure 2.22 Absorbance of the desorbed dye in a 1 mM KOH water solution versus film weight for four electrodes of thicknesses 2.6, 7.7, 24, and 38 μm [78].-----	41
Figure 2.23 Growth-per-cycle for the ALD processes: (a) Layer-by-layer growth mode, (b) Substrate-enhanced growth, (c) Substrate-inhibited growth, and (d) Island growth [82].-----	43
Figure 3.1 The appearance and layout of Savannah S100 Atomic Layer Deposition (ALD) system made by Cambridge NanoTech Corporation.-----	45
Figure 3.2 Illustration of the layer structure of the DSSCs employed in this study.-----	47

Figure 3.3 The appearance and schematic layout of Peccell solar simulator (PEC-L12). ----	48
Figure 3.4 The appearance and schematic layout of a combined electron spectroscopy (VG ESCALab 250). -----	50
Figure 3.5 Schematic diagram shows the UPS process of photoemission. -----	52
Figure 3.6 Schematic diagram shows the XPS process of photoemission. -----	53
Figure 3.7 Schematic diagram shows the REELS process. -----	54
Figure 3.8 Schematic diagram shows the XRD process. -----	56
Figure 4.1 (a) TEM image of the nanocrystalline TiO ₂ without ALD Al ₂ O ₃ overlayer. (b) TEM image of the nanocrystalline TiO ₂ with 10-cycles ALD Al ₂ O ₃ overlayer. (c) Result of the growth-per-cycle of Al ₂ O ₃ layers via the Al ₂ O ₃ thickness increment per cycle. -----	58
Figure 4.2 XPS results showing (a) Ti2p _{3/2} and (b) Al2p core level photoelectron peaks from ALD Al ₂ O ₃ coated TiO ₂ electrodes. -----	60
Figure 4.3 (a) UPS valence band region and (b) UPS secondary electron region of the as-received and ALD Al ₂ O ₃ deposited TiO ₂ electrode. (c) REELS spectra of the as-received and ALD deposited TiO ₂ electrode. -----	63
Figure 4.4 Changes of the work function, Ti2p _{3/2} XPS peak and Al2p XPS peak with various thicknesses of Al ₂ O ₃ layers. -----	64
Figure 4.5 Schematic band diagram with three interfacial energy parameters: the difference of WF between Al ₂ O ₃ and TiO ₂ over-layer ($\Delta\Phi_{T-A}$), the charge recombination barrier height (ϵ_{RB}) and the interfacial energy barrier height between N719 dye and Al ₂ O ₃ (ϵ_{IB}). -----	66
Figure 4.6 Interfacial energy levels difference ($\Delta\Phi_{T-A}$, ϵ_{RB} , ϵ_{IB}) and PCE via the thickness of Al ₂ O ₃ layers. -----	68
Figure 4.7 Schematic band diagrams illustrate that the paths of electron transfer from dye into	

TiO₂ (a) without any energy barrier and therefore improve the cells PCE due to the ultra-thin Al₂O₃ energy levels, and (b) by tunneling effect when the Al₂O₃ layer is thicker. ----- 69

Figure 5.1 C/S model for calculating the fractional coverage (θ) of shell layers from an isolated C/S particle. The left circular plane is the cross-sectional plane which produces a projection line at a certain azimuth angle. ----- 78

Figure 5.2 The multi-layers-C/S model for calculating the coverage of shell layers from each layer. ----- 78

Figure 5.3 The illustration reveals the signals of layer-2 penetrating the upper core/shell particles. ----- 81

Figure 5.4 TEM images of nanocrystalline TiO₂ core particles prepared (a) without an Al₂O₃ shell layer, (b) with a two-cycle-ALD Al₂O₃ shell layer, (c) with a five-cycle-ALD Al₂O₃ shell layer, and (d) with a 10-cycle-ALD Al₂O₃ shell layer. ----- 86

Figure 5.5 The enlarged TEM images show the TiO₂ core particles (a) without an Al₂O₃ shell layer, (b) with a one-cycle-ALD Al₂O₃ shell layer, (c) with a five-cycle-ALD Al₂O₃ shell layer. ----- 87

Figure 5.6 XPS spectra of the Ti 2p_{3/2} peaks from the nanoporous TiO₂ electrodes. ----- 88

Figure 5.7 Coverages (θ) of Al₂O₃ shell layers on TiO₂ electrodes, obtained from XPS analyses. The experimental data (crosses) match the corresponding theoretical curves from our C/S model. ----- 90

Figure 5.8 Changes in the PCE and coverage, plotted with respect to the number of ALD reaction cycles for Al₂O₃ shell layers on TiO₂ electrodes. ----- 92

Figure 6.1 XPS data for the (a) Ti 2p_{3/2} and (b) Al 2p core level photoelectron peaks from ALD Al₂O₃-coated TiO₂ electrodes. ----- 97

Figure 6.2 (a) TEM images of the anatase TiO₂ nanoparticles featuring a 10-cycle ALD Al₂O₃

overlayer. Inset in (a) shows the high-magnification image of a selected area of the marked area. (b) TEM images of the marked area of a rutile TiO_2 particles (shown in the inset) featuring a 10-cycle ALD Al_2O_3 overlayer. ----- 98

Figure 6.3 Growth-per-cycle of the Al_2O_3 overlayers as a function of the number of ALD reaction cycles. ----- 100

Figure 6.4 XRD spectra of the anatase electrode layer (a) and the rutile electrode layer (b) with respect to the number of ALD deposition cycles of the Al_2O_3 overlayer. ----- 102

Figure 6.5 Lattice volumes of TiO_2 crystals in (a) the anatase and (b) in the rutile electrode layers, plotted with respect to the number of ALD reaction cycles of the Al_2O_3 overlayer. ----- 104

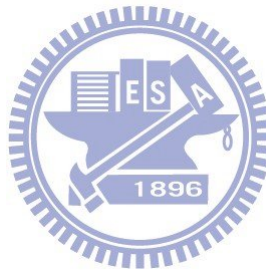


List of Symbols

I^{nth}	: the signal intensities of the nth layer after the shell coating
I_0^{nth}	: the signal intensities of the nth layer before the shell coating
S^*	: negative ion of dye
$*\varepsilon_{\text{IB}}$: the interfacial energy barrier height between N719 dye and Al_2O_3
a	: the thickness of each monolayer
a	: a fractional constant and is closely related to the size of the region
$A_{\text{A, core}}$: projection area of the core particles in a layer
$A_{\text{A, shell}}$: projection area of the a shell-only-regions in a layer
ALD	: atomic-layer-deposition
α_x	: the strip angle
b	: the fractional constant for the shell-only region
C/S	: core/shell
CBM	: conduction band minimum
d	: the sample density (g/cm^3)
D	: diameter of the bare core particles
ΔC_{M}	: the number of atoms M (here is Al) adsorbed per unit surface area per cycle
$\Delta\Phi_{\text{A-T}}$: the difference of work function between Al_2O_3 and TiO_2 over-layer
Δh	: the thickness increment per cycle
ΔI	: intensities of photoelectrons emitted from a single strip with the shell layer
ΔI_{α}	: intensities of photoelectrons emitted from a single strip without the shell layer
ΔI_{bulk}	: intensity of the photoelectrons from a strip of infinite length
DSSC	: dye-sensitized solar cell
E	: the e-beam energy (KeV)
ε_{RB}	: charge recombination barrier height
eV_{bi}	: built-in potential
Φ	: work function
ϕ	: azimuth angles

FF	: fill factor
HOMO	: highest occupied molecular orbital
I	: total intensity (I) of photoelectrons emitted from the entire half part of the circular plane with the shell layer
I^-/I_3^-	: negative ion of iodide/triiodide
I_0	: intensities of photoelectrons emitted from the substrate without the thin film material
I_o	: the intensity of photoelectrons from circular plane without the shell layers
I_0^{total}	: total XPS signal intensity of the C/S structured thin film without the shell layer
I_s	: intensities of photoelectrons emitted from the substrate with the thin film material
I^{total}	: total XPS signal intensity of the C/S structured thin film with the shell layer
J_{sc}	: short-circuit current
λ	: the inelastic mean free path (IMFP) of electrons traveling in the overlayer
λ_{core}	: the IMFP of electrons traveling in the core particle
λ_{shell}	: the inelastic mean free path (IMFP) of electrons traveling in the shell layer
LUMO	: lowest unoccupied molecular orbital
M	: the molar mass of layer
M	: multi-layers Factor
M_w	: molecular weight of the core or shell material
n	: the number of monolayers in an island
n_A	: the number of the atoms in a molecule
N_a	: Avogadro's number
O	: the origin of the circle
P	: porosity
PCE	: the power conversion efficiency
θ	: fractional coverage
θ_{island}	: island coverage
ρ	: the density of layer

S^+	: positive ion of dye
SF	: sub-layer Factor
σ_i	: interfacial energy
S^o	: dye molecular
σ_o	: surface energy of the overlayer
σ_s	: surface energy of the substrate
σ_{st}	: accumulated strain energy
t_x	: thickness of the shell
VBM	: valence band maximum
V_{oc}	: open-circuit voltage
$V_{V,core}$: volume fraction of the core particles in a layer
$W_{\alpha,a}$: the width of a strip
WF	: work function
X	: the depth of electron penetration



Chapter 1

Introduction

1.1 The Challenge for Photovoltaic Devices

Global energy consumption in 2030 is expected to rise 1.4 times than its present level [1]. It is anticipated the demand for fossil fuels will increase with economic growth of developing countries; however, the amount of main energy resources available for supply in the world will less than 130 years from present [2], as shown in Fig. 1.1. Based on the present rate of consumption, the remaining exploitable global resources, in term of years, show the expected period are 122, 42, and 60 years for coal, oil, and natural gas, respectively. Although new oil fields and mines will be discovered in the future, we cannot deny they are limited resources and need to be replaced by other more suitable energy resources. To the point, the supply of energy from the sun to the earth is estimated to be 3×10^{24} J/year, which is 10000 times more than the current global human consumption. That is, covering photovoltaic devices on only 0.1% of the earth's surface with a conversion efficiency of 10% is sufficient for global needs at the present day [3].

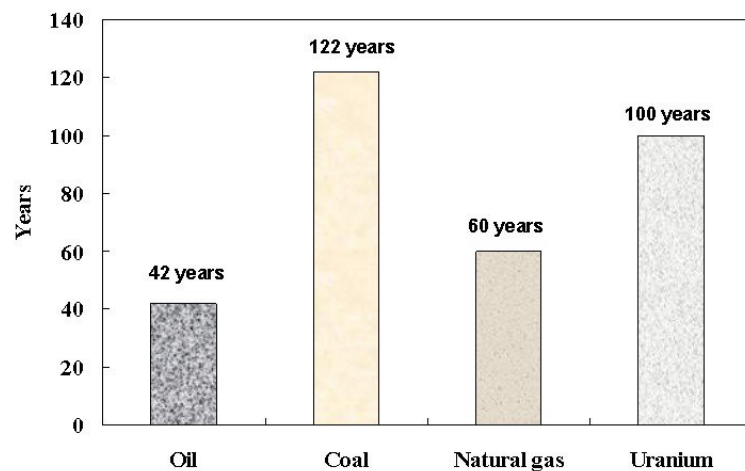


Figure 1.1 The remaining exploitable global resources in term of years [1].

The cost to generate the electric power is a key to alternative resources in the future. Table 1-1 shows the relative electric power cost generated by various resources [1]. The hydroelectric and wind power are clean and low-cost energy sources, but are restricted by the proper geography, weather and location. On the other hand, concerning global warming and pollution issues, solar cells are considered as the next generation energy resource, because it will be more cost-effective in the next two decades to generate the electric power than other energies, to support the continued growth of the global economy [4]. The Japanese research institute NEDO (New Energy Development Organization) and ANRE (Agency for Natural Resources and Energy, Government) expects that the power generation cost of new solar cells will reach 14 yen/KWh, lower than that of home-used electricity in 2020, and a power conversion efficiency of 20% [2]. Therefore, efforts are being focused on technologically developing new types of solar cells to reach higher efficiencies and lower production costs.

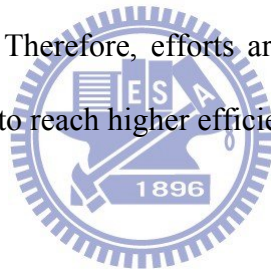


Table 1-1 The relative electric power cost generated by various resources [1].

<i>Power source</i>	<i>Units price of electric power generation</i>
Hydroelectric	8.2 – 13.3 yen
Oil	10 – 17.3 yen
Natural gas	5.8 – 7.1 yen
Coal	5 – 6.5yen
Nuclear	4.8 – 6.2 yen
Photovoltaic	49 yen
Wind	9 – 14 yen

1.2 The Importance of Dye-Sensitized Solar Cells

Recent concerns about the laborious, energy-consuming, and costly production of photovoltaic devices have accentuated the need for more efficient, dye-sensitized solar cells (DSSCs) [5]. As an emerging energy source, DSSC has the potential to become a third generation solar cell offering the following advantages [6]:

1. Low production cost and lower investment cost
2. Transparency and multi-color options
3. Flexibility
4. Lightweight
5. Feedstock availability to reach terawatt scale
6. Short energy payback time
7. Enhanced performance under diffuse light and higher temperatures
8. Capture light from all angles
9. Outperforms competitors for indoor applications

In addition to these advantages, the electric generation cost of DSSCs was regarded to be the lowest of photovoltaic devices in the 2020 to 2030 market evaluated by NEDO (New Energy Development Organization) and ANRE (Agency for Natural Resources and Energy, Japanese Government) [7], as shown in Fig. 1.2. The number of DSSCs research groups around the world is growing, indicating great opportunities of DSSCs to be a future alternative energy resource, as shown in Fig. 1.3 [6], a literature search illustrates the increase in the number of research papers and patents over the last several years.

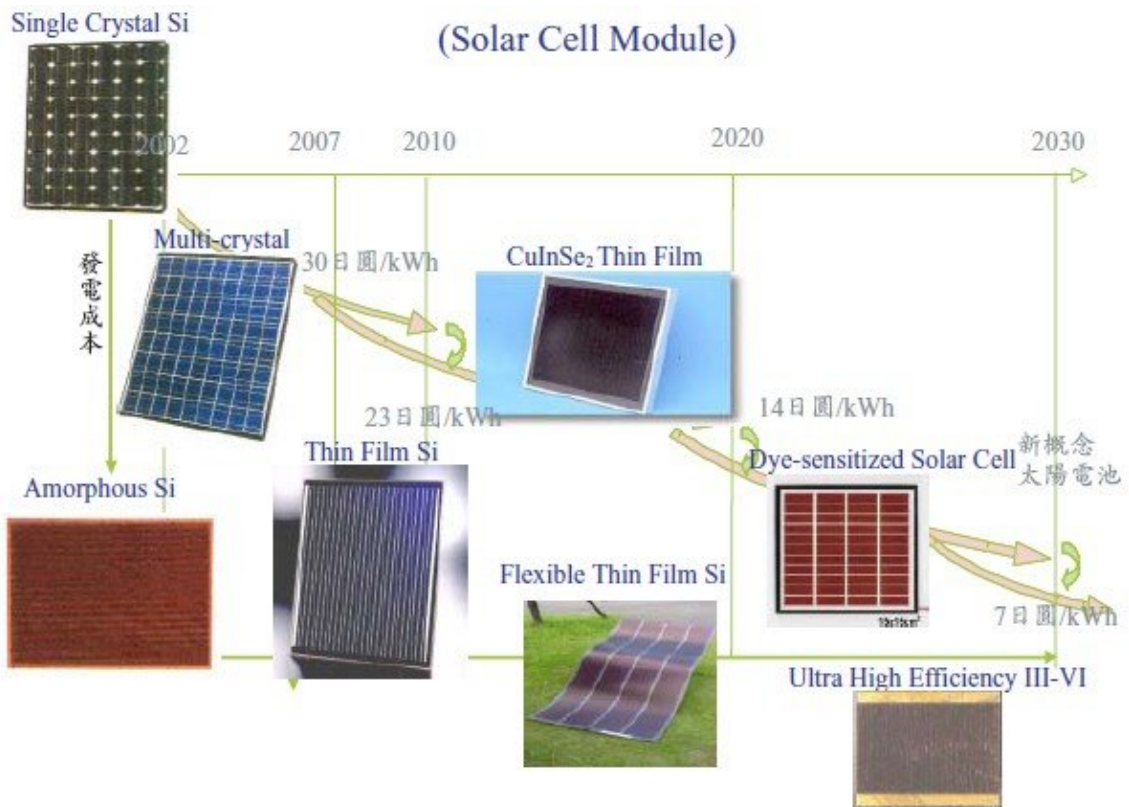
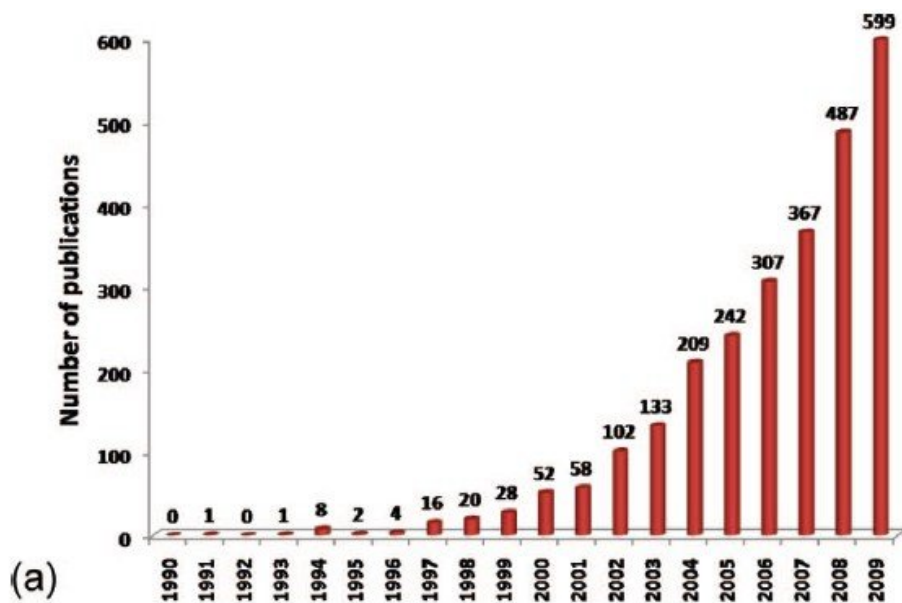
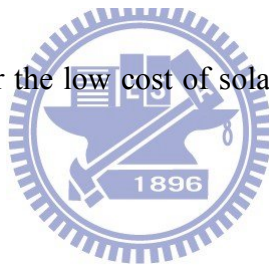


Figure 1.2 The developing trend for the low cost of solar cells shows the DSSC as the main solar cell in 2020 to 2030 [7].



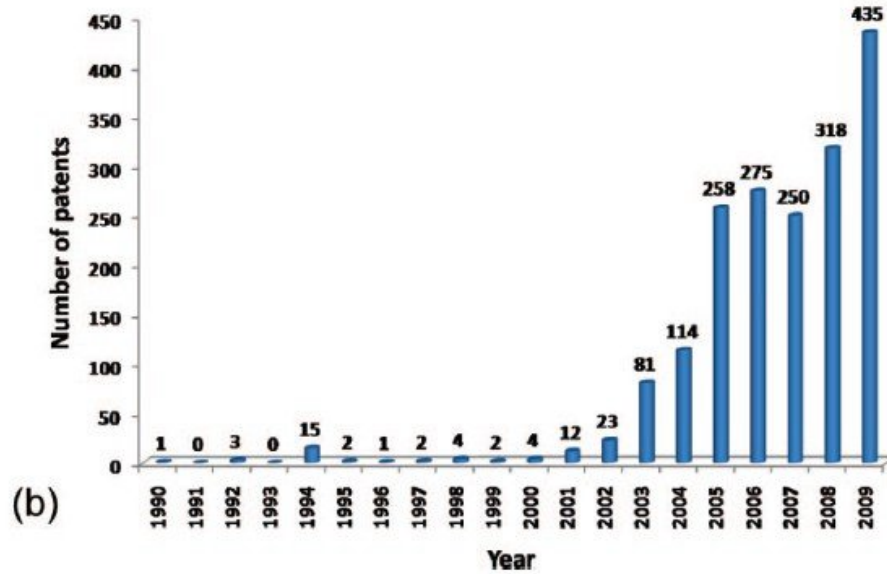


Figure 1.3 Number of (a) publications published per year, and (b) patents submitted, obtained from a simple and limited literature search using the keywords “dye-sensitized” and “solar” [6].



The commercial progress of DSSC in the near future is mainly hindered by two major problems: the rare ruthenium-based dye and the corrosive electrolyte [8]. However, some proponents of DSSCs expect these problems will be solved, especially for small-sized DSSCs, as international companies such as Samsung SDI, Corus, Sharp, DNP and 3G Solar are expected to produce products in the next two years [9]. As a result, the commercialization of DSSC will ideally occur in 2013. Presently, the application of DSSC, namely a Building Integrated Photovoltaic System (BIPV), will account for more than 50% of the DSSC market and portable electric chargers are expected to grow to 20% of the market. The annual production and growth rate of DSSC are expected to follow the trend shown in Fig. 1.4 [9]. The annual production may reach 2.6 GW in 2015 and the anticipated growth rate ranges between 100 and 520 % both the numbers showing the prosperous future of DSSC.

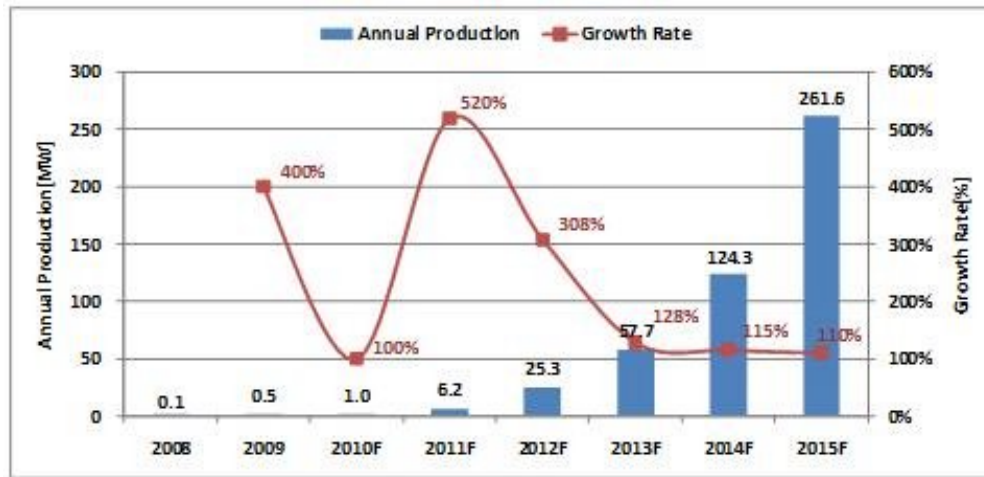


Figure 1.4 Dye-Sensitized Solar Cell(DSSC)'s annual production and growth rate forecasting [9].

1.3 Enhancing the DSSC Efficiency with Core/Shell

Electrodes



A high efficient DSSC was developed in 1991 by using a nanoporous electrode to increase the dye/electrode interface, thus increasing the number of electrons transferred into the electrode [10]. Therefore, modifying the dye/electrode interface is a direct method to achieve higher efficiency in DSSC. One of the most efficient processes to enhance DSSC performance is to coat the porous electrodes with an ultra-thin oxide layer [11].

In literature, only three types of nanoporous electrodes (TiO_2 , SnO_2 and ZnO) were found to enhance the efficiency of DSSCs with core/shell structures. Figure 1.5 shows the performances of DSSCs with TiO_2 [12-23], SnO_2 [24-31], ZnO [32-37]–core/shell electrodes from 2001 to 2011. The most efficient electrode with shell layers, shown in Fig. 1.5(a) was a TiO_2 electrode; in addition, SnO_2 and ZnO core/shell electrodes produced more improvement

in efficiency of DSSCs. Al_2O_3 shells were the most commonly used layers in high efficient TiO_2 -core/shell electrodes. Recently, the shell layers coated on TiO_2 electrode by Atomic Layer Deposition (ALD) increased the DSSC's power conversion efficiency (PCE) by 14 to 80% indicating that ALD may be the ideal shell fabrication process for DSSCs, and hence further study is necessary [19, 21, 22].

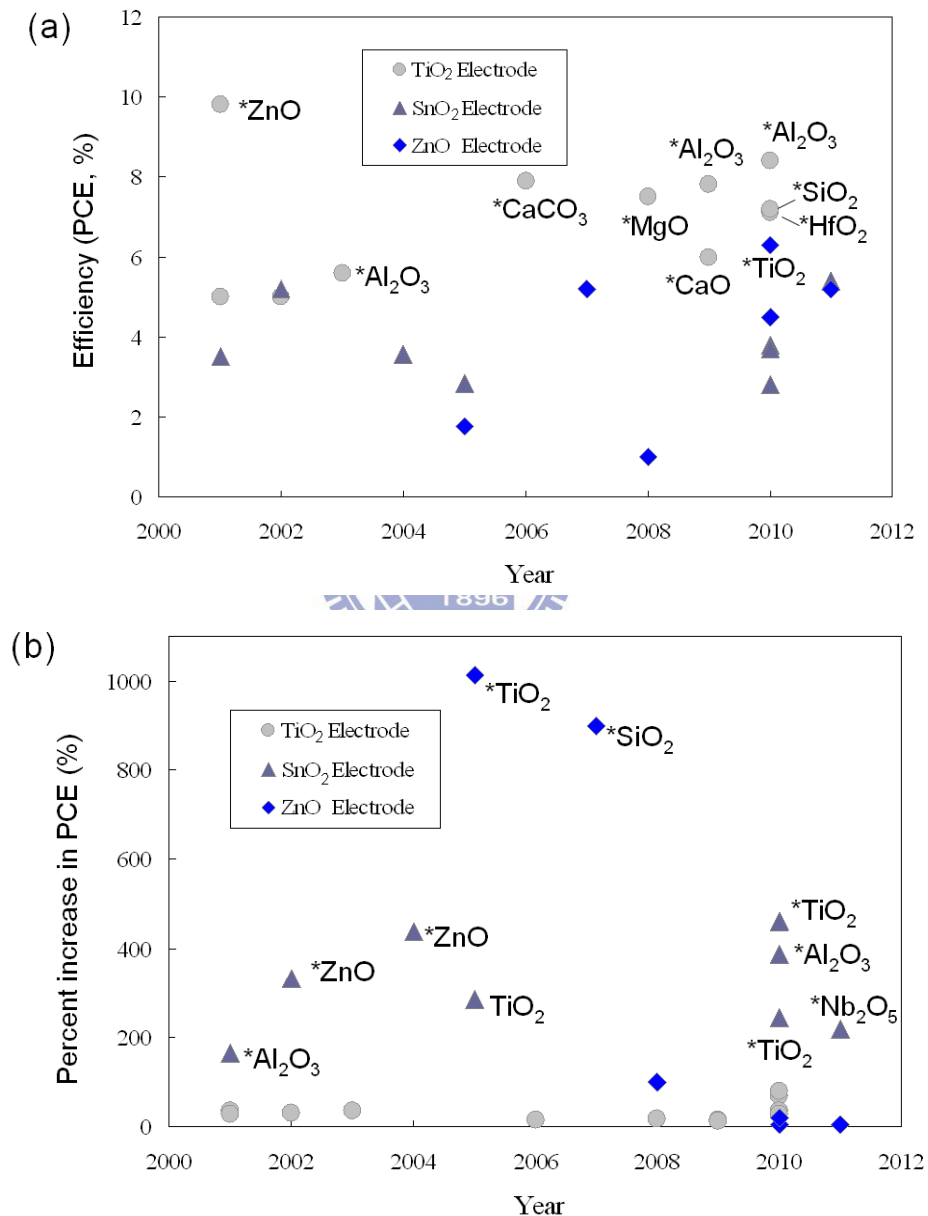
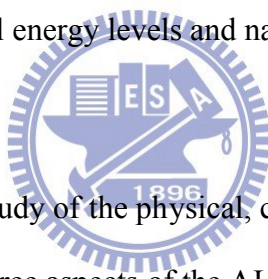


Figure 1.5 (a) the efficiency of DSSCs and (b) the percent increase in PCE of DSSCs with TiO_2 [12-23], SnO_2 [24-31], ZnO [32-37]-core/shell electrodes from 2001 to 2011. Asterisks denote the shell layers in top-ten values.

1.4 Objectives and Arrangements of the Study

Based on the aforementioned points, we chose atomic layer deposited Al_2O_3 over-layers as the shell layers, on the nanoporous TiO_2 electrodes of dye-sensitized solar cells (DSSCs). Previous explanations for the improvement of DSSCs with the Al_2O_3 over-layers were based solely on the assumptions made on the energy levels at core/shell interface and quality of the coating on the TiO_2 electrodes which, consequently, were rarely accurate, because the interfacial energy levels may change significantly due to chemical reaction and the coverage of shell layers may be decreased by the island growth. The future improvement of DSSCs will be determined, in part, by the extent of the understanding developed on the $\text{Al}_2\text{O}_3/\text{TiO}_2$ interface through the analysis of real energy levels and nano-structures.



To achieve a comprehensive study of the physical, chemical, and electrical properties of the Al_2O_3 over-layers, we studied three aspects of the ALD $\text{Al}_2\text{O}_3/\text{TiO}_2$ electrodes: interfacial energy levels, surface coverage, and growth mode. We examine a low-temperature ALD process for forming the Al_2O_3 barriers to achieve compatibility with low-temperature DSSCs fabrication processes. The relation of interfacial energy level, surface coverage, and growth mode to power conversion efficiency (PCE) was investigated by using TEM, ultraviolet photoelectron spectroscopy (UPS), x-ray photoelectron spectroscopy (XPS), and reflective electron energy loss spectroscopy (REELS). The nano-structure and influence of ALD Al_2O_3 layers on nanoporous TiO_2 electrodes in DSSCs were also studied using these characterization techniques.

The organization of this dissertation is as follows:

Chapter 1 introduces the motivation and objective of this study.

Chapter 2 reviews the literature concerning basic concept of solar energy, recent progress of DSSCs, characterization and previous studies of core/shell electrodes.

Chapter 3 describes the experimental method and analytic techniques.

Chapter 4 discusses the interfacial energy levels of Al_2O_3 films on TiO_2 electrodes of DSSCs. The related properties are also discussed.

Chapter 5 shows a calculated model that measures the coverage of the core/shell electrode of DSSCs from XPS signals. The model calculated the coverage from isolated spheres to multi-layers core/shell materials, which can evaluate the ideal PCE of DSSCs with the core/shell electrodes.

Chapter 6 discusses the growth modes of Al_2O_3 deposited on TiO_2 electrodes of DSSCs. Obtaining a comprehensive understandings of the influencing factors of the ALD Al_2O_3 deposited on TiO_2 electrodes of DSSCs was investigated.

Chapter 7 concludes the experimental results and suggests future work worthy for pursuing.

Chapter 2

Literature Review

This chapter reviews the properties of solar energy and power, development of dye-sensitized solar cells, and the characterization of core/ shell electrodes.

2.1 Solar Energy and Power Conversion Efficiency

The solar irradiance, also named as solar constant, is defined as the power density of sunlight outside the atmosphere of earth and is regarded as a constant, 1367 W/m^2 , by the World Radiometric Center (WRC) [38]. However, when sunlight reaches the earth's surface, the solar radiation changed due to atmosphere effects (i.e., absorption and scattering), weather, latitude, time etc. The measurement of power conversion efficiency of solar cells is affected by many factors, hence, it is necessary to introduce the standard conditions to evaluate the power conversion efficiency of solar cells.

2.1.1 Air Mass

The maximum radiation strikes the earth's surface when the sun is directly overhead, having the shortest path length through the atmosphere at clear skies. The path length is called the air mass (AM) and can be calculated by the equation $AM = 1/\cos \varphi$, where φ is the zenith angle as shown in Fig. 2.1. The standard solar spectrum outside the earth's atmosphere is called AM 0. The path length of standard solar spectrum used for efficiency measurements of solar cells is AM 1.5 G (global), given that $\varphi = 48.19^\circ$ [39]. Fig 2.2 presents the photon flux of the AM 1.5 G spectrum at 1000 W/m^2 and the calculated accumulated photocurrent.

The spectrum is normalized such that the integrated irradiance (i.e., the amount of radiant energy received from the sun per unit area) is 1000 W/m^2 . In the diagram, the maximum photocurrent is the current at short-circuit conditions for a solar cell device converting all incident photons below the absorption onset wavelength into electric current. For example, the maximum short-circuit current for a solar cell with an absorption onset of 700 nm is 20 mA/cm^2 .

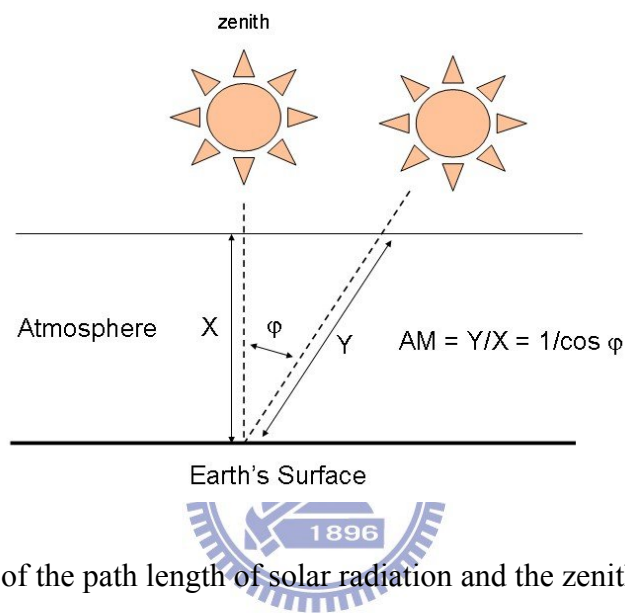


Figure 2.1 Illustration of the path length of solar radiation and the zenith angle ϕ .

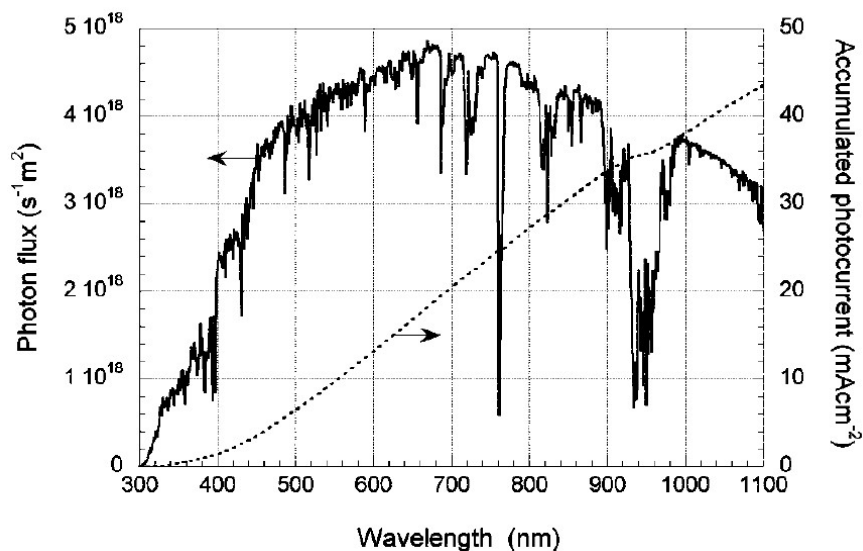


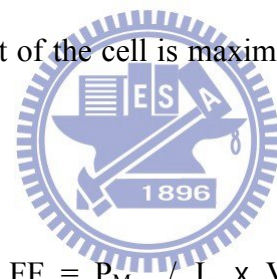
Figure 2.2 Photon flux of the AM 1.5 G spectrum at 1000 W/m^2 , and calculated accumulated photocurrent. (ASTM G173-03)

2.1.2 Power Conversion Efficiency

The power conversion efficiency (PCE, η) of the dye-sensitized cell is determined by the following equation [40]:

$$\eta = J_{sc} \times V_{oc} \times FF / I_s \quad (2-1)$$

where the J_{sc} is the photocurrent density measured at short circuit, the V_{oc} is open-circuit photo-voltage, FF is the fill factor of the cell and equal to $J_{Max} \times V_{Max} / J_{sc} \times V_{oc}$, and I_s the intensity of the incident light, as shown in Fig. 2.3. The maximum power (P_{Max}) is equal to $J_{Max} \times V_{Max}$ where the power output of the cell is maximal. Then the fill factor of the cell can be calculated as follows:



$$FF = P_{Max} / J_{sc} \times V_{oc} \quad (2-2)$$

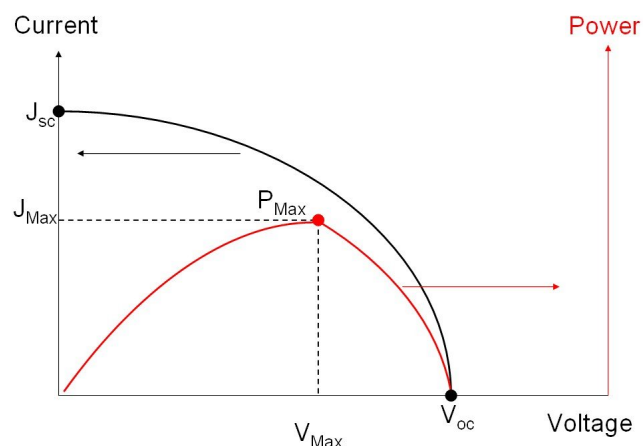
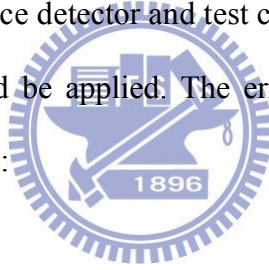


Figure 2.3 Typical shape of the current-voltage curve of a solar cell.

2.1.3 Standard Measurement of PCE

Accurate efficiency measurement of a solar cell depends on the international standard reporting conditions (SRC) such as 100 mW/cm² total irradiance, AM 1.5G reference spectrum, and 25 °C cell temperature [41]. The current AM 1.5G reference spectrum used by the international terrestrial photovoltaics community is from International Electrotechnical Commission (IEC) Standard 60904-3, as shown in Fig. 2.4, and American Society for Testing and Materials (ASTM) Standard G173-03. Typically, the irradiance incident on the solar cell is measured with a reference cell. The spectral error in the measured short-circuit current (J_{SC}) of the solar cell is induced by the mismatch between the spectral irradiance of the light source and the reference spectrum. In addition, the difference between the spectral responses of the reference detector and test cell needs to be corrected. Therefore, a correction for these errors should be applied. The errors can be expressed as a spectral mismatch correction factor (M) [41]:



$$M = \frac{\int_{\lambda_1}^{\lambda_2} E_{\text{Ref}}(\lambda) S_R(\lambda) d\lambda \times \int_{\lambda_1}^{\lambda_2} E_S(\lambda) S_T(\lambda) d\lambda}{\int_{\lambda_1}^{\lambda_2} E_{\text{Ref}}(\lambda) S_T(\lambda) d\lambda \times \int_{\lambda_1}^{\lambda_2} E_S(\lambda) S_R(\lambda) d\lambda} \quad (2-3)$$

where $E_{\text{Ref}}(\lambda)$ is the reference spectral irradiance, $E_S(\lambda)$ is the source spectral irradiance, $S_R(\lambda)$ is the spectral responsivity of the reference cell, and $S_T(\lambda)$ is the spectral responsivity of the test cell, all of which are a function of wavelength (λ). The range of λ_1 and λ_2 in the above equation should cover the full spectra and spectral responses to avoid error.

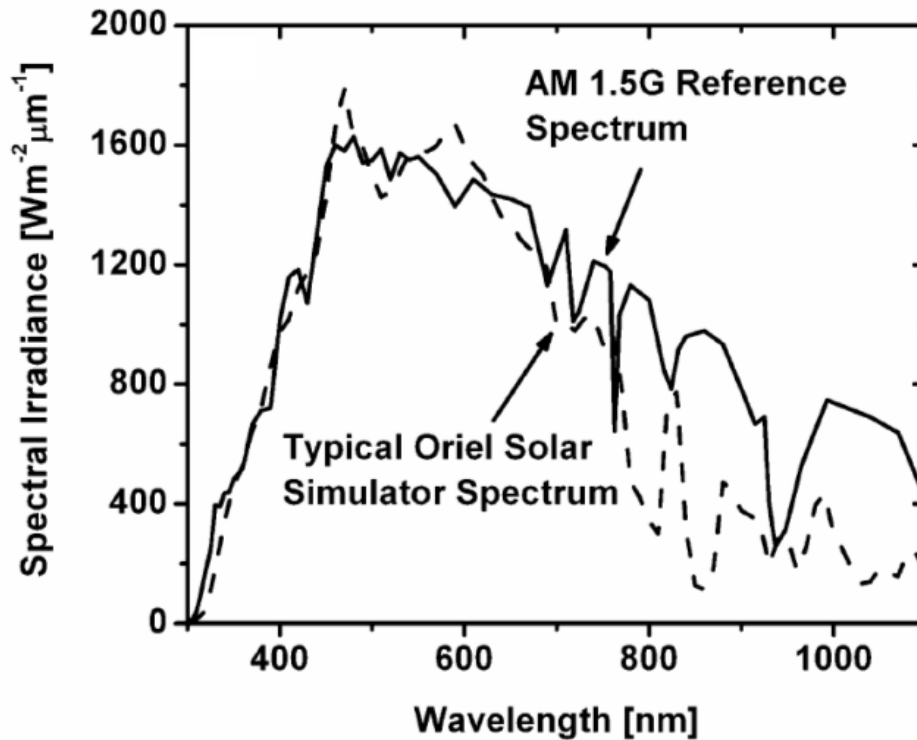


Figure 2.4 Spectral irradiance for AM 1.5 G reference spectrum (IEC 60904-3) and the typical source irradiance of an Oriel 150 W solar simulator. Intensities of the spectra have been normalized to 100 mW/cm^2 [41].

2.2 Developments in Dye-Sensitized Solar Cells

2.2.1 Evolution of Dye-Sensitized Solar Cells

In 1873, H. Vogel discovered the “dye sensitization” by adding some organic dyes into silver halide to enhance the green and red light absorption [42]. The silver halides used in photography are insensitive to visible light and have band gaps in the range of 2.7-3.2 eV, just as the TiO_2 used in DSSCs. The dye-sensitized phenomenon was later explained as the electron transfer from the organic dyes to the silver halide. What followed was the first sensitization of photo-electrode using a similar chemistry was performed in 1887 [43].

Research in the sensitization in solar cells then commenced [44-47] and showed cell conversion efficiencies below 1% in the following century.

The milestone of high-efficiency DSSCs was established by B. O'Regan and M. Grätzel in 1991 [10]. The cell construction with 7% solar power conversion efficiency composed of nano-crystalline TiO₂ electrode and ruthenium complex dye is still used now in modern DSSCs. The surface-area of the TiO₂ film introduced was believed to induce the enormous power conversion efficiency by loading larger amounts of dye and increasing light absorption. The great improvement achieved in their research was not only the introduction of the nano-crystalline TiO₂ electrode, to achieve the enormous power conversion efficiency, but also determining the main structure for the best-performing modern DSSCs. In recognition of this contribution, these types of DSSCs are generally referred as "Grätzel's Cell". In the decade after the original publication, the record efficiency for the Grätzel's cell increased from 7.1% to 10%, however, in the subsequent decades the efficiency has only increased to 11.5% [48].

2.2.2 Operational Principles of Dye-Sensitized Solar Cells

The main operating principle of the DSSCs is presented in Fig. 2.5 [49]. From left to right, the cell consists of a transparent conductive oxide (TCO) substrate, normally doped SnO₂ with fluorine on glass. A porous transparent semiconductor layer is coated onto the substrate, normally 10-15 μm of ~20 nm TiO₂ particles, which gives an internal surface area of ~1000 cm² per cm² substrate. Dye molecules are absorbed onto the internal surface of this semiconductor to form approximately one monolayer. The typical dye is N719. The substrate is joined to a counter electrode, usually a few nanometers of platinum on another

TCO glass. A seal is formed around the cell, followed by injection of electrolyte through a hole which is subsequently sealed. So far all DSSCs have been based on an iodine/iodide electrolyte in organic solvent. A typical electrolyte consists of methoxypropionitrile (MPN) with 0.6 M propylmethylimidazolium iodide, 0.1 M LiI, 0.1 M tert-butylpyridine, and 0.1 M iodine.

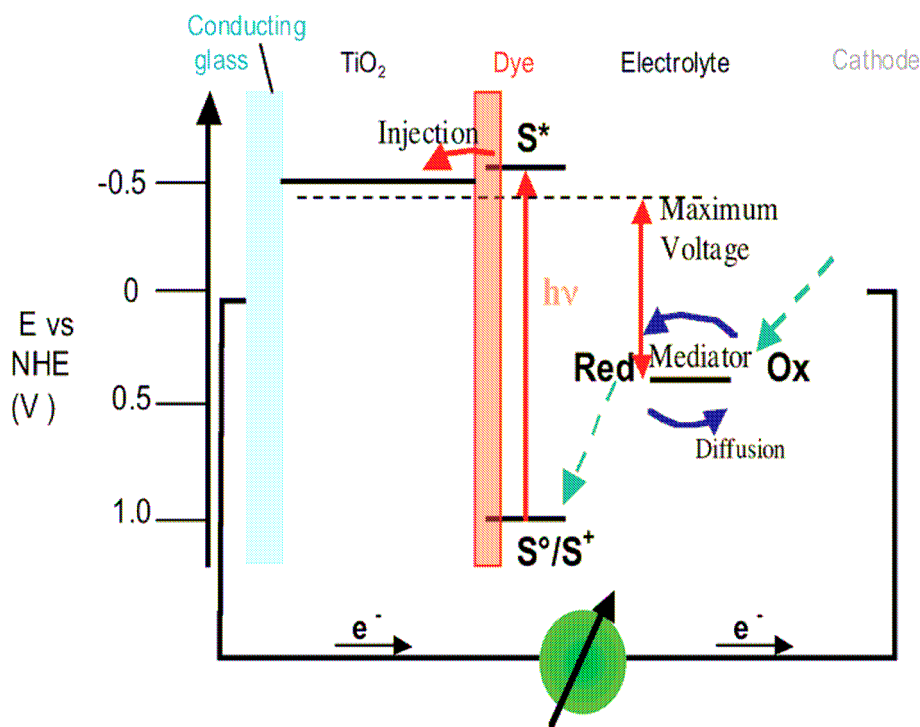
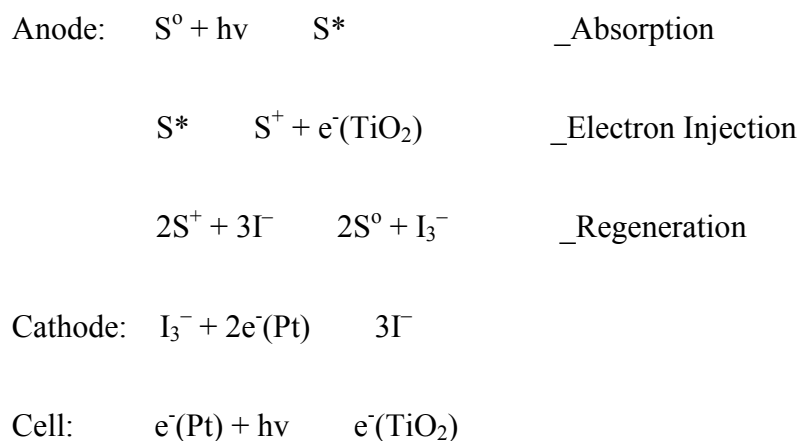


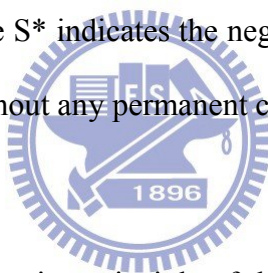
Figure 2.5 Energy band diagram of a typical DSSC employing an iodide/triiodide-based redox electrolyte and N719 as a sensitizer dye [49].

As shown in Fig. 2.5, the sensitizer attached to the surface of a porous film absorbs the energy from sunlight ($h\nu$). The injection of electrons into the conduction band of the oxide is induced by the process of photo-excitation of the dye. Subsequently, the electron from electrolyte regenerates to the dye on the surface of porous films. The electrolyte contains the negative ion of iodide/triiodide (I^-/I_3^-) couple as a redox couple. Reduction of positive ion of dye (S^+) by iodide (I^-) regenerates the original form of the dye (S^0) while producing triiodide

ions (I_3^-). This prevents any significant increase of S^+ , which could recapture the conduction band electron at the surface. The iodide is regenerated by the reduction of the triiodide ions at the counter-electrode, where the electrons are acquired from the external circuit through the Pt. The whole reaction can be represented by following processes.



Where the S^0 represents the dye, the S^* indicates the negative ion of dye. Thus, the device is generating electricity from light without any permanent chemical transformations.



Recently, a second type of operating principle of the DSSCs was proposed [50-52]. As shown in Fig. 2.6, the type II DSSCs are based on direct electron injection from the ground state (HOMO) of the sensitizer (dye) into the conduction band of TiO_2 . Unlike the conventional DSSCs, photoexcitation of the type II dye results in the direct electron injection from the ground state of the sensitizer into the conduction band of the TiO_2 , omitting the charge transfer that electron jumping from the ground state to the excited state (LUMO) of dye and then injecting into the conduction band (E_{CB}) of the TiO_2 . Noted that no photoexcited dye states are involved in the type II DSSCs, in contrast to conventional DSSCs. Typical type II sensitizers are organic molecules composed of endiol ligands that form a chelating bond with an under coordinated tetrahedral $Ti(IV)$ surface state [52].

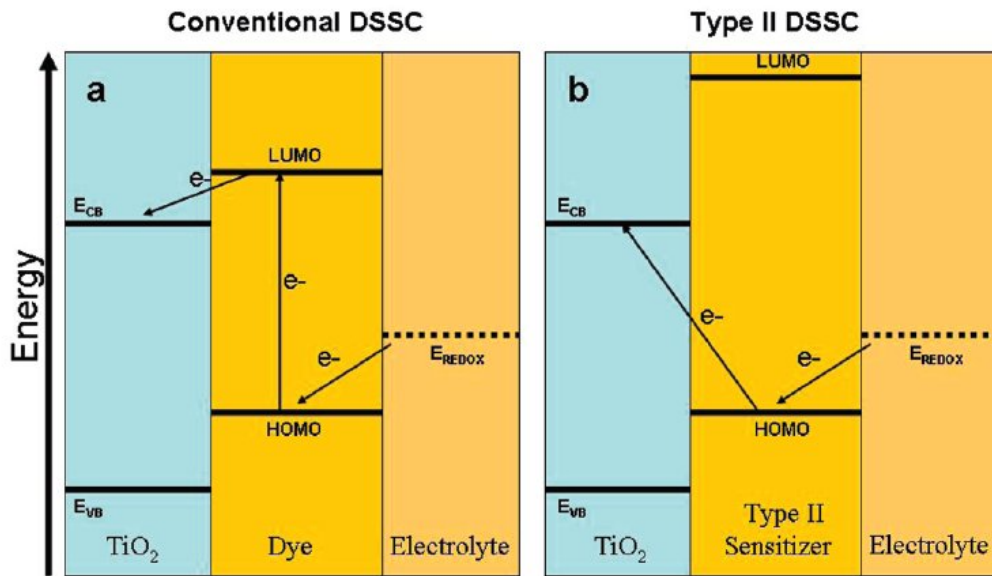


Figure 2.6 Illustrations comparing the operational principles of a (a) conventional DSSC and (b) Type II DSSC [52].

2.2.3 Surface Area of the Nano-Crystalline Electrodes

The specific surface area of the nano-crystalline TiO₂ structure is about 2000 times larger than that of the bulk TiO₂ structure [10] and directly increases both the light harvesting area and dye-electrode interface enormously. Figure 2.7 compares the incident photon to charge carrier efficiency (ICPE) of dye-sensitized solar cell with flat electrode and nano-crystalline electrode, the improvement is about 600 times increase for the nano-crystalline electrode [5]. The incident-photon-to-current conversion efficiency is plotted as a function of wavelength with both flat electrode and nano-crystalline electrode. The IPCE value obtained with the single-crystal electrode is only 0.13% at 530 nm, where the value with the nanocrystalline electrode reaches 88% — more than 600 times greater.

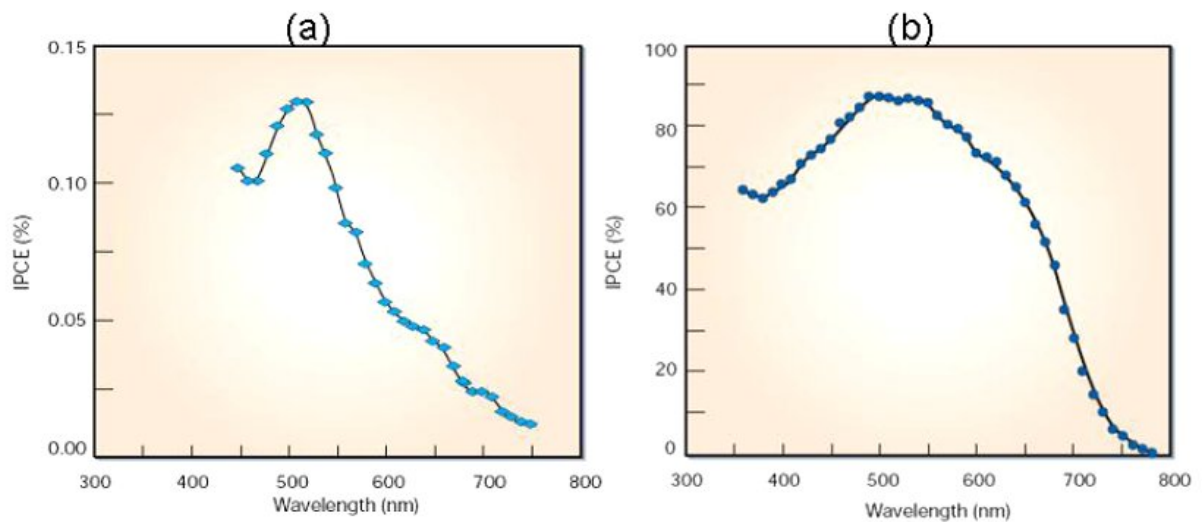


Figure 2.7 Comparison of the incident wavelength to charge carrier efficiency (ICPE) of dye-sensitized solar cell with (a) flat electrode and (b) nano-crystalline electrode [5].

As mentioned above, there are many ways to improve the surface of porous electrodes to optimize the efficiency. One of the most successful methods is to coat the nano-crystalline electrode with a thin shell layer has been research over last decade. However, although many variants of the fabrication, including surface layers on nano-crystalline particles, have been studied, the lack of characterization limited the development in DSSCs with a core/shell electrode. For example, although a 0.2 nm thick shell layer can be deposited on a nano-crystalline or core/shell electrode, it is difficult to measure the surface coverage of this shell layer [53]. The following sections will discuss the problems in detail.

2.3 Core/Shell Electrodes in DSSCs

As shown in Fig 2.8, two core/shell structures have been developed to create the electrodes of DSSCs [54]. One includes the fabrication of nanoparticles and then forming a shell layer on the surface of nanoparticles. This leads to the formation of core/shell structured

nanoparticles to form the photoelectrode film (Fig 2.8a). However, such a structure creates an energy barrier not only at the nanoparticle/electrolyte interface but also between the individual core nanoparticles. In another structure, the photoelectrode film is composed of nanoparticles prepared prior to the deposition of shell layer, as show in Fig. 2.8(b). The latter structure is obviously beneficial to electron transport, it is a challenge to fabricate a shell layer in term of ideal uniformity of the shell material.

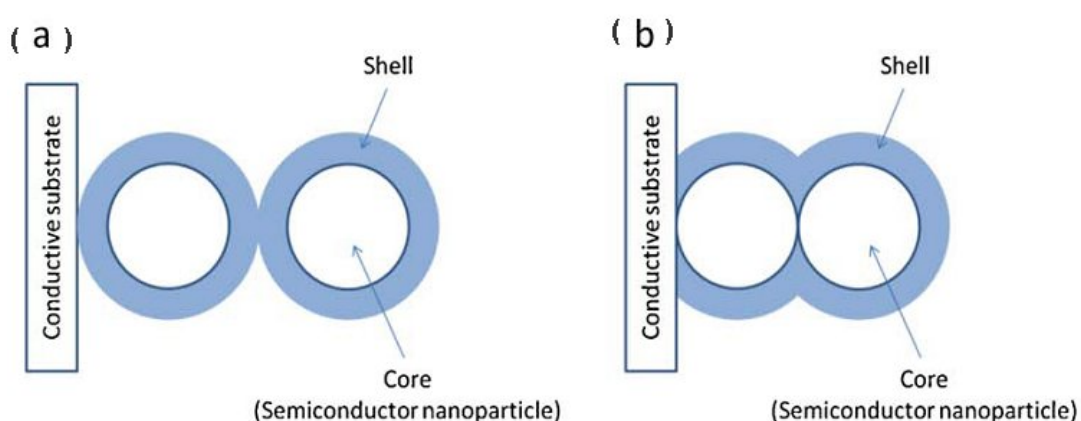


Figure 2.8 Core/shell structures used in DSSCs. (a) The shell layer is formed prior to the film deposition, (b) the shell layer is coated after the film deposition [54].

In this study, we defined the core/shell electrode like previous study [55] as the nanoporous inorganic semiconductor electrode that is covered with a shell of other metal oxide and coated after the film deposition. These electrodes can slow the recombination processes by the formation of an energy barrier at the TiO_2 surface. The conduction band of the shell should be higher than that of the core semiconductor to generate an energy barrier for the reaction of the electrons present in the core with the oxidized dye or the redox mediator in solution. Nevertheless, there exist the varying conclusions on the path of electron transfer through the shell layer.

2.3.1 Operational Principles of Core/Shell Electrodes

The first core/shell electrode was developed by A. Zaban et al. in 2000 [11]. They reported the fabrication of a $\text{TiO}_2/\text{Nb}_2\text{O}_5$ nanoporous electrode, which improved the performance of dye sensitized solar cells by more than 35%. In the mechanism described as the illumination of a DSSC, an electron is injected from the dye into the TiO_2 film followed by a hole transfer to the electrolyte. The injected electrons must cross the TiO_2 film and reach the conducting substrate, while the oxidized ions diffuse towards the back electrode, where they are re-reduced. The porous geometry that permits the presence of the electrolyte through the entire electrode provides a high surface area for recombination between the injected electrons and the holes in solution. In the absence of an energy barrier at the electrode–electrolyte interface, the rate of this recombination process may be very high depending on the properties of the hole carrier. As illustrated in Fig. 2.9, the energy level differences form an energy barrier at the electrode–electrolyte interface, which can reduce the rate of recombination processes of the photoinjected electrons. A comparison of two similar DSSCs that differ only in their nanoporous electrode, shows that the core/shell electrode is superior to the standard one with respect to all cell parameters. This demonstrated superiority, measured from many cells results in a 35% increase of the overall conversion efficiency.

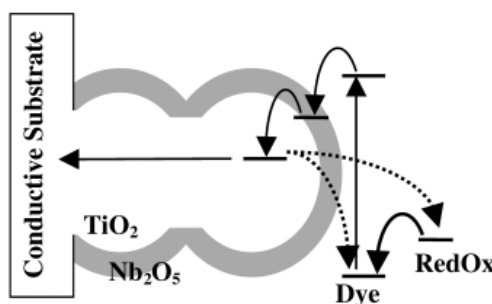


Figure 2.9 A schematic view of the new nanoporous electrode which consists of a nanoporous TiO_2 matrix covered with a thin layer of Nb_2O_5 [11].

The second mechanism suggested by E. Palomares [14,15], where the conformal growth of an overlayer of Al_2O_3 on a nanocrystalline TiO_2 film, is shown to result in a 4-fold retardation of interfacial charge recombination, and a 30% improvement in photovoltaic device efficiency. The main charge-transfer events that take place at the TiO_2 /dye/electrolyte interface are depicted in Fig. 2.10. Visible light is absorbed (1) by the sensitizer dye. Electron injection (2) from the excited state of the dye into the conduction band of the TiO_2 by tunneling effect is followed by the subsequent regeneration of the dye by I^-/I_3^- red/ox couple (4). Efficient operation of the DSSC device relies upon the reduction of the possible recombination pathways occurring at the TiO_2 /dye/electrolyte interface, allowing efficient charge transport through the TiO_2 film and electrolyte and subsequent charge collection at the device contacts. There are two possible recombination losses to consider. The injected electrons may recombine either with oxidized dye molecules (3) or with the oxidized redox couple (5).

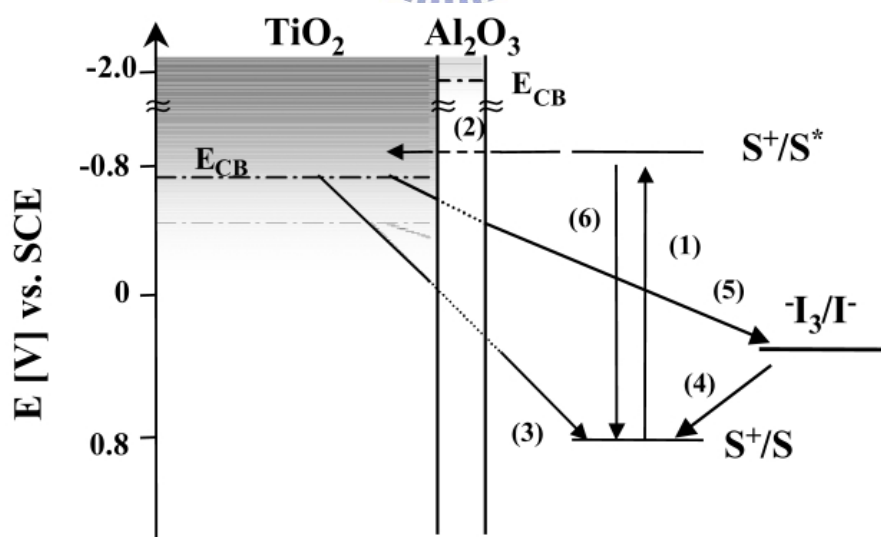


Figure 2.10 Illustration of the interfacial charge-transfer processes occurring at the nanostructure TiO_2 /dye/electrolyte interface of DSSC [14,15].

The difference between these two mechanisms can be seen at the path (2) of electron transfer. The first mechanism claimed electron injection (2) from the dye into TiO_2 without any energy barriers, but the second mechanism assumed electron injection (2) from dye into TiO_2 by tunneling effect. This understanding is based on the assumption of that ultra-thin over-layers maintain the same energy levels after coating on the TiO_2 electrodes as in the bulk structure; consequently, the energy diagrams of DSSCs with $\text{Al}_2\text{O}_3/\text{TiO}_2$ interface structures have been determined mostly by inserting the energy data from bulk material and assuming the vacuum levels of all of the layers are equal.

In 2002, Diamand et al. used SrTiO_3 as a shell layer to coat on the TiO_2 electrode [55]. They found that SrTiO_3 layer shifted the conduction band of the TiO_2 (E_{CB}^0) in the negative direction, rather than formed an energy barrier at the TiO_2 surface, as shown in Fig. 2.11. This type of photoanode modification cannot suppress the back recombination rate as a function of the electron density, but can suppress the back recombination as a function of the applied potential. As a result, the forming “surface dipole” reduced J_{sc} slightly and significantly increased the V_{oc} and the devices conversion efficiency was improved by 15.3%. As shown in Fig. 2.11(b), the formation of a potential step subjected to the surface dipole shifted the conduction band of TiO_2 in the negative direction.

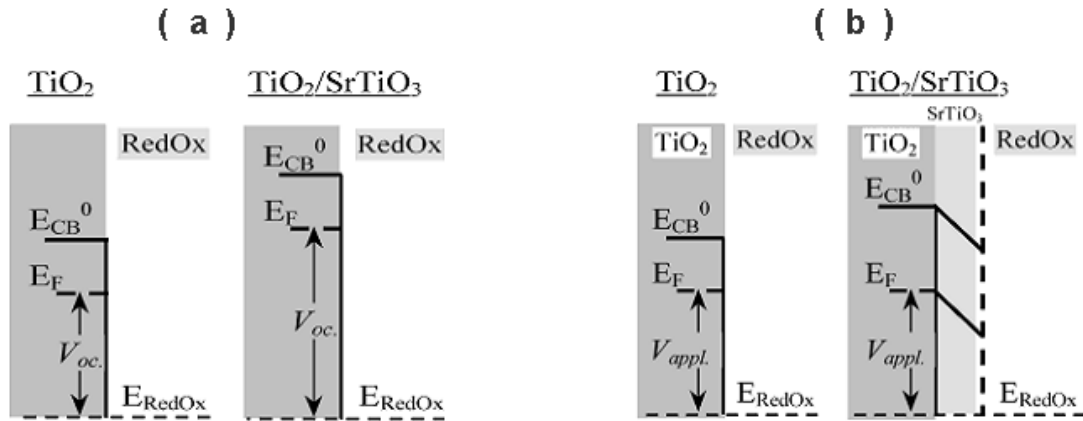


Figure 2.11 Energy diagram representing the movement of (a) the TiO_2 conduction band by the SrTiO_3 coating and (b) the effect of the band shift at applied potential indicated the coated system is more resistive than the bare electrode [55].

The core/shell electrode has also been used in the type II DSSC [52]. Figure 2.12 shows the operation of the SrTiO_3 barrier layer as a barrier of recombination in the type II DSSC using catechol as a dye; therefore, the cell is named a catechol-sensitized type II DSSCs (CSSCs). The SrTiO_3 's conduction band is higher than the conduction band of TiO_2 by 0.2 eV, forming an energy barrier between the TiO_2 and the catechol. Due to excitation, an electron is injected from the HOMO level of the catechol molecule into the conduction band of the SrTiO_3 . The energy difference between the SrTiO_3 and TiO_2 conduction band edges creates a tendency for the electron transfers from the SrTiO_3 layer to the TiO_2 core, resulting in the reduction of the back electron transfers to the oxidized catechol compared to the uncoated TiO_2 particles.

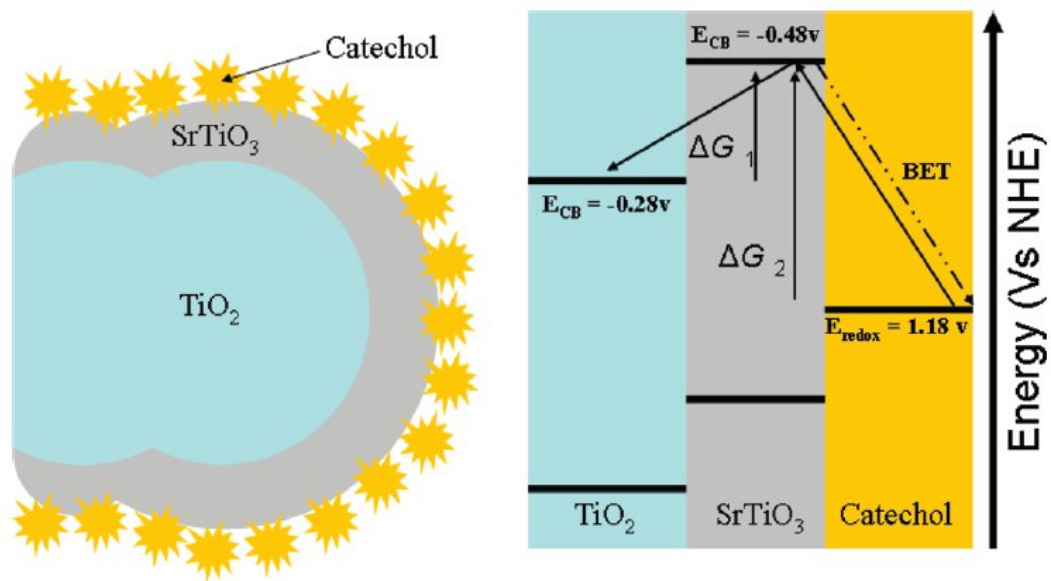


Figure 2.12 Schematic drawing of a CSSC with a SrTiO₃ barrier layer (left). The band diagram shows the different electron-transfer processes (right) [52].

Another method to improve electron injection and suppress electron recombination in core/shell electrodes is by reducing the surface state sites of electrode via passivation [56,57]. Figure 2.13 shows the band diagrams before passivation (right) and after passivation (left). Passivation induces a larger band gap that could further suppress electron recombination. According to previous studies [58, 59], 3–10 nm PbS particles which filled the surface states of TiO₂ electrode effectively and improved power conversion efficiency by 20%. The similar mechanism was demonstrated with TiO₂ electrodes modified by alizarin (C₁₄H₈O₄) [60].

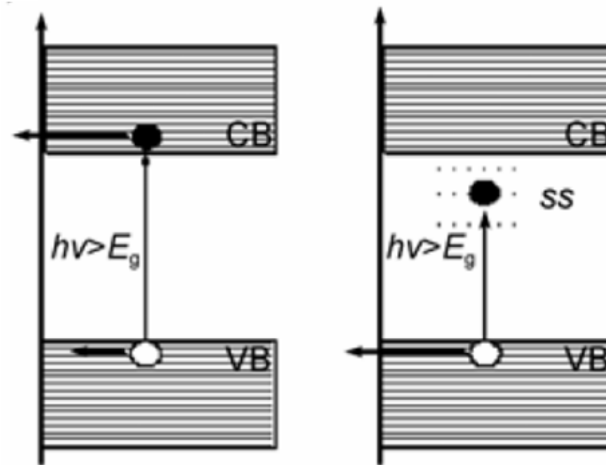


Figure 2.13 The band diagrams show the band gap (E_g) before passivation (right) and after passivation (left). A larger band gap could further suppress more electron recombination [56,57].

2.3.2 The Materials of Electrodes with Shell Structure

Generally, materials for high-efficient electrodes should satisfy the two important conditions: a) ease in fabricating the larger surface areas, b) a band structure compatible with that of the dye, and c) high stability to the corrosive electrolyte. The compatible band structure can be expressed as shown in Fig. 2.14, with the band positions of some photo-semiconductors in contact with electrolyte at PH 1 [5]. The conduction band minimum (CBM) of electrodes should be similar to TiO_2 or near the zero energy of the normal hydrogen electrode (NHE), since the CBM of dye is just about 0.4 eV higher than the zero energy [53]. Therefore, combined with condition (a) and (c), three types of electrodes (TiO_2 , SnO_2 and ZnO) were found, in the literature, to enhance the efficiency of DSSCs by the shell, as described in the following sections.

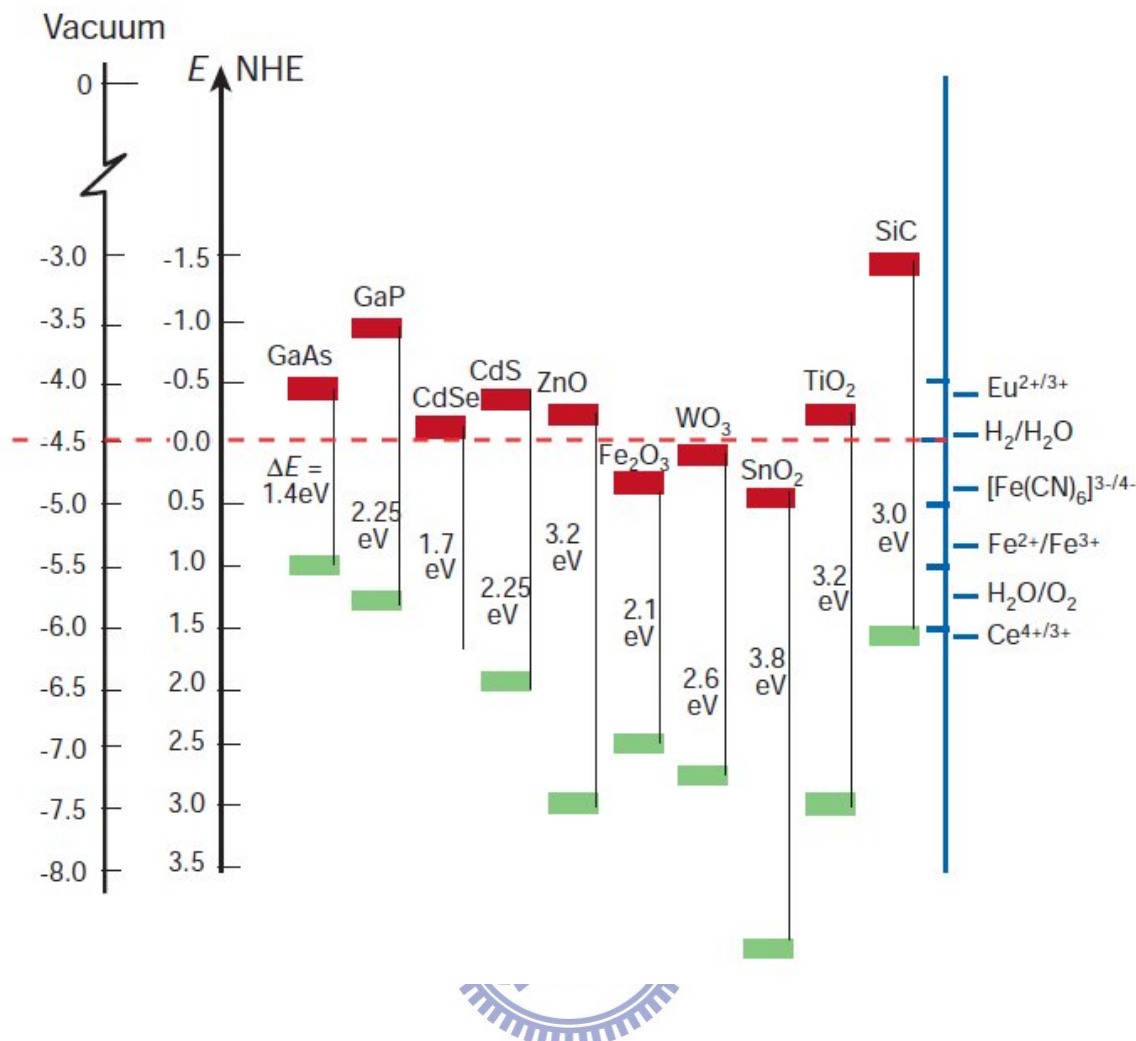


Figure 2.14 The band positions of photo-semiconductors in contact with electrolyte at PH 1 [5].

2.3.2.1 TiO₂ Electrodes with Shell Structures

Table 2-1 summarizes the performances of DSSCs with TiO₂-core/shell electrodes with PCE greater than or equal to 5.0 %, from 2001 to 2011 [12-23]. Al₂O₃ is the most popular shell material with many researchers improving the PCE of DSSCs by 14 to 35 %. A ZnO shell layer increased the PCE to 9.8% which is the highest performance in the table; however, there is a controversy on this study due to the later studies reported only 2.29 to 4.51% PCE for DSSCs with ZnO shell layers [61, 62]. The shell layers fabricated by Atomic Layer

Deposition (ALD) which increase the DSSC's PCE by 14 to 80% indicated the ALD may be the ideal shell fabrication process for DSSCs and the further study is necessary.

Table 2-1 Summary of the performances of DSSCs with TiO₂-core/shell electrodes for PCE values greater than or equal to 5.0 % from previous studies [12-23].

<i>Reference</i>	<i>Year</i>	<i>Electrode</i>	<i>Shell layer</i>	<i>Shell fabricated process</i>	<i>PCE (%)</i>	<i>Percent increase in PCE (%)</i>
[12]	2001	Nano-Porous TiO ₂	Nb ₂ O ₅	Sol-gel	5.0	35
[13]	2001	Nano-Porous TiO ₂	ZnO	Hydrothermo method	9.8	27.3
[14]	2002	Nano-Porous TiO ₂	Al ₂ O ₃	Sol-gel	5.0	30
[15]	2003	Nano-Porous TiO ₂	Al ₂ O ₃	Sol-gel	5.6	35
[16]	2006	Nano-Porous TiO ₂	CaCO ₃	Dip-coating	7.9	14.5
[17]	2008	Nano-Porous TiO ₂	MgO	Sputtering	7.5	17.4
[18]	2009	Nano-Porous TiO ₂	CaO	Evaporation	6.0	15.1
[19]	2009	Nano-Porous TiO ₂	Al ₂ O ₃	Atomic Layer Deposition	7.8	14
[20]	2010	Nano-Porous TiO ₂	HfO ₂	Atomic Layer Deposition	7.1	69

[21]	2010	Nano-Porous TiO ₂	Al ₂ O ₃	Atomic Layer Deposition	8.4	35
[22]	2010	Nano-Porous TiO ₂	SiO ₂	Atomic Layer Deposition	7.2	80
[23]	2010	Nano-Porous TiO ₂	Ba(NO ₃) ₂	Dipping/sintering	6.7	28

In 2004, A. Zaban found a relation between V_{oc} change and the isoelectric point (IEP) of shell materials on TiO₂, that is, the V_{oc} is roughly proportional to the isoelectric point, as shown in Fig. 2.15 [55]. He proposed that oxides such as ZnO, SrTiO₃, ZrO₂ and Al₂O₃ with isoelectric points higher than that of the TiO₂, created a positive charge on surface, leading to an increase in the open circuit voltage; however, the Al₂O₃ shows some different trend in the figure that might be attributed to the formation of surface dipole layer on the Al₂O₃ shell. A surface dipole layer was created toward the TiO₂, leading to an increase in the open circuit voltage of the cells; however, a decrease in the photocurrent was observed. This indicates the formation of a dipole layer might accelerate the electron recombination. It should be noted that the observed photocurrent is the difference between the forward photocurrent and the photocurrent caused by the back recombination. Therefore, for the TiO₂-core/ Al₂O₃-shell nanostructures, it is necessary to investigate the dipole layer as well as the band structure.

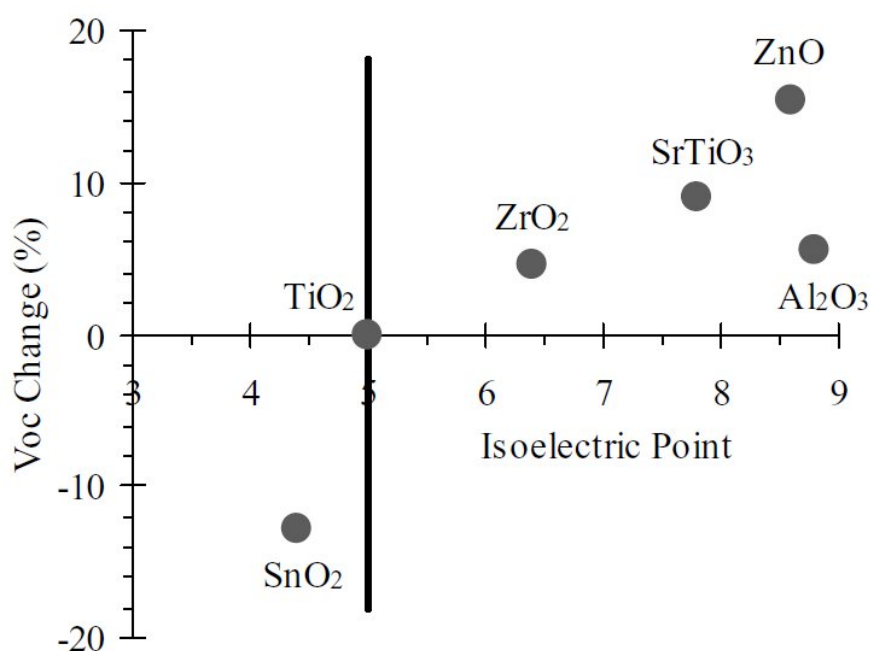


Figure 2.15 A relation between V_{oc} change and the isoelectric point (IEP) of shell materials on TiO_2 [55].



2.3.2.2 SnO₂ Electrodes with Shell Structure

Table 2-2 lists the performances of DSSCs with SnO₂-core/shell electrodes for PCE fabricated from 2001 to 2011 [24~ 31]. The SnO₂ core/shell electrodes produced much lower PCE than the TiO₂ core/shell electrodes. The Al₂O₃, ZnO, TiO₂ are the most popular shell materials used for SnO₂ electrodes which improved the PCE of DSSCs by 166 to 460 %. The Nb₂O₅ shell layer increased the PCE to 5.48 % which is the highest performance of all shell layers. Recently, the shell layers fabricated by Atomic Layer Deposition (ALD) increased the DSSC's PCE by 386 %, indicating the ALD may be the ideal shell fabricated process for SnO₂ electrodes and the further study maybe necessary.

Table 2-2 Summary of the performances of DSSCs with SnO₂-core/shell electrodes [24-31].

<i>Reference</i>	<i>Year</i>	<i>Electrode</i>	<i>Shell layer</i>	<i>Shell fabricated process</i>	<i>PCE (%)</i>	<i>Percent increase in PCE (%)</i>
[24]	2001	Micro-Porous SnO ₂	Nano-Particle Al ₂ O ₃	Dip-coating	3.2	166
[25]	2002	Nano-Porous SnO ₂	ZnO	Mixing	5.2	333
[26]	2004	Nano-Porous SnO ₂	ZnO	Mixing	3.5	439
[27]	2005	Nano-Porous SnO ₂	Nano-Particle TiO ₂ /Al ₂ O ₃	Dip-coating	2.85	285
[28]	2010	Nano-Porous SnO ₂	Nano-Particle TiO ₂	Dip-coating	3.8	245
[29]	2010	Nano-Porous SnO ₂	TiO ₂ /MgO	Dip-coating	2.8	460
[30]	2010	Nano-Porous SnO ₂	Al ₂ O ₃	Atomic Layer Deposition	3.7	386
[31]	2011	Nano-Porous SnO ₂	Nb ₂ O ₅	Dip-coating	5.48	220

In 2002, M. Grätzel [25] coated different oxides on SnO₂ electrode and summarized the performances of DSSCs as shown in Table 2-3, listing the data that also roughly obey the relationship between the isoelectric point and V_{oc}. In addition, the surface of the oxide coating was more basic than SnO₂, which increased dye attachment and resulted in the photovoltage and fill factor being strongly enhanced. The optimum thickness of shell layer

was about a few angstroms, suggesting that electron transfer occurs from dye to SnO₂ by the tunneling effect. Different coating methods for SnO₂ nano-crystals with a thin layer of an insulating oxide may result in different efficiencies. On the other hand, the shell coverage and thicknesses in the table indicated these two factors are important issues in affecting the efficiency of the DSSCs, but a comprehensive study is still lacking.

Table 2-3 Summary of the performances of DSSCs with SnO₂-core/shell electrodes, from reference [25].

colloid	modified with	resulting oxide coating	oxide coverage ($\mu\text{mol}/\text{m}^2$)	equivalent coating thickness (nm)	short-circuit photocurrent I_{sc} (mA/cm^2)	open-circuit photovoltage V_{oc} (mV)	fill factor ff (%)	energy conversion efficiency η (%)
SnO ₂	–	–	0	0	6.4	480	40	1.2
SnO ₂	ZnO powder	ZnO	?	?	11.2	690	67	5.2
SnO ₂	Zn(CH ₃ -COO) ₂	ZnO	40	0.59	11.2	670	69	5.1
SnO ₂	TiCl ₄	TiO ₂	18	0.35	10.9	660	54	3.9
SnO ₂	ZrOCl ₂	ZrO ₂	25	0.50	12.9	550	47	3.4
SnO ₂	Mg(NO ₃) ₂	MgO	12	0.13	12.6	600	51	3.8
SnO ₂	Al(NO ₃) ₃	Al ₂ O ₃	6	0.16	9.7	610	61	3.6
SnO ₂	Y(NO ₃) ₃	Y ₂ O ₃	3	0.13	13.6	530	49	3.7
SnO ₂	Y(NO ₃) ₃	Y ₂ O ₃	6	0.27	13.8	610	59	4.9
SnO ₂	Y(NO ₃) ₃	Y ₂ O ₃	12	0.54	10.7	680	60	4.4
SnO ₂	Sc(CF ₃ -SO ₃) ₃	Sc ₂ O ₃	10	0.35	11.0	610	61	4.2
SnO ₂	La(NO ₃) ₃	La ₂ O ₃	8	0.40	14.0	510	46	3.3
SnO ₂	Sm(NO ₃) ₃	Sm ₂ O ₃	8	0.40	14.0	530	49	3.6
SnO ₂	Nd(NO ₃) ₃	Nd ₂ O ₃	8	0.40	13.1	520	48	3.2
SnO ₂	Ga(NO ₃) ₃	Ga ₂ O ₃	9	0.28	11.3	580	49	3.3
SnO ₂	In(NO ₃) ₃	In ₂ O ₃	5	0.20	8.2	500		1.8

2.3.2.3 ZnO Electrodes with Shell Structure

Table 2-4 lists the performances of DSSCs with ZnO-core/shell electrodes for PCE from 2001 to 2011 [32-37]. The ZnO-core/shell electrodes received better PCE than the SnO₂-core/shell electrodes but lower than TiO₂. The TiO₂, SiO₂ are most popular shell materials used for ZnO electrodes to improve the PCE of DSSCs by 4 to 1012 %. The atomic-layer-deposited TiO₂ shell layer increased the PCE to 6.3 % which is the highest performance in the table. Compared to Dip-coating, the shell layers fabricated by Atomic Layer Deposition (ALD) increase the DSSC's PCE 3 to 6 times indicated the ALD may be

the ideal shell fabricated process for ZnO electrode and the further study maybe necessary.

Table 2-4. Summary of the performances of DSSCs with ZnO-core/shell electrodes [32-37].

<i>Reference</i>	<i>Year</i>	<i>Electrode</i>	<i>Shell layer</i>	<i>Shell fabricated process</i>	<i>PCE (%)</i>	<i>Percent increase in PCE (%)</i>
[32]	2005	Nano-Porous ZnO	TiO ₂	Dip-coating	1.78	1012
[33]	2007	Nano-Porous ZnO	SiO ₂	Sol-gel	5.2	900
[34]	2008	Nano-Porous ZnO	TiO ₂	Dip-coating	1.02	100
[35]	2010	Nano-Porous ZnO	SiO ₂	Sol-gel	4.51	4
[36]	2010	Nano-Porous ZnO	TiO ₂	Atomic Layer Deposition	6.3	21.1
[37]	2011	Nano-Porous ZnO	Nb ₂ O ₅	Dip-coating	5.2	4.4

The ZnO electrode may not be an appropriate material to be coated with high efficient shell layers because its isoelectric point is quite high (see Fig. 2.15); however, the band structure of ZnO is similar to TiO₂, explaining the DSSC's performance enhancement by the surface passivation of SiO₂ or the efficient electron transportation of TiO₂ shell layer. It should be noted that ZnO and SiO₂ are also two of the best shell layers applied on TiO₂ electrode, as can be seen in Table 2-1. On the other hand, recently, the advanced structure of porous ZnO electrode was referred as the submicrometer-sized ZnO nanocrystallite

aggregates, which can enhance light scattering and efficiency of DSSCs without decreasing the surface area of electrodes for dye adsorption or TiO₂ shell [36], as shown in Fig. 2.16. This shows the ZnO electrodes with nanocrystallite aggregates might have the potential to improve the efficiency with shell layers.

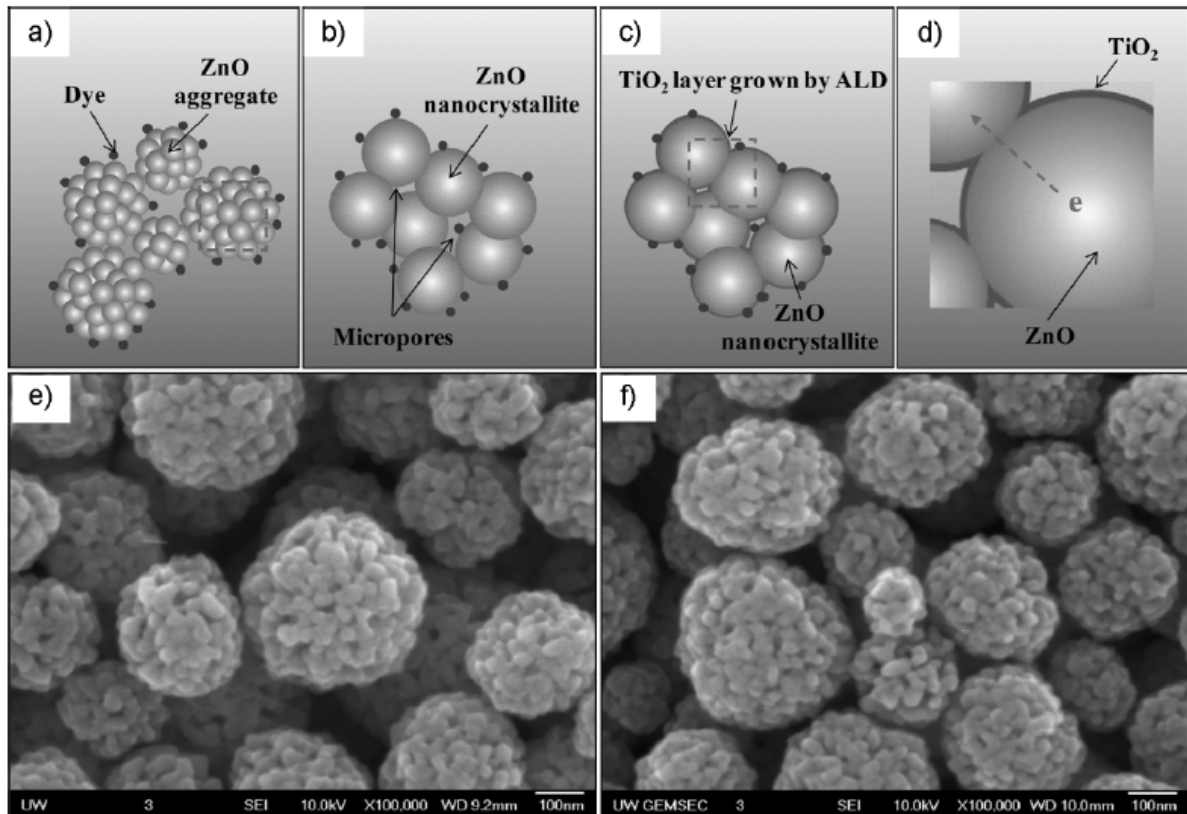


Figure 2.16. Illustrations showing (a) ZnO aggregates with dye molecules, (b) ZnO nanocrystallites with micropores, (c) thin ALD-TiO₂ layer on ZnO nanocrystallites, (d) enlarged schematic of (c), and (e) SEM of the aggregates of ZnO nanocrystallites, (f) SEM of the aggregates of ZnO nanocrystallites coated with thin TiO₂ layer [36].

2.3.2.4 Atomic Layer Deposited Al₂O₃ Shells

As there is a lot of interest and work in efficiency enhancement, the power conversion efficiency (PCE) of DSSCs based on nanoporous TiO₂ electrodes has been consistently

increased by 14-35% using Al_2O_3 over-layers [14-15, 19, 21]. Optimization of the $\text{Al}_2\text{O}_3/\text{TiO}_2$ interface in DSSCs was carried out by different coating procedures, which have relied so far on sol-gel or solution processes that provide the capability of infiltrating porous structures thereby ensuring good coverage of the surface of the nanoporous electrode. The sol-gel or solution processes require a sintering step at 450-500 °C to achieve good quality and, hence, has limited compatibility with low-temperature fabrication processes, such as those for making plastic-based flexible DSSCs [64]. Low-temperature (100 °C) sol-gel Al_2O_3 layers have been demonstrated on flexible DSSCs by Haque et al [65], however, the improvement provided was not as significant as that achieved by the high-temperature sol-gel process. Besides the temperature constraints of the typical sol-gel process, the thickness of the sol-gel films can only be altered with a resolution of ~1 nm [14, 66], which is too coarse for adjusting the optimal thickness of the Al_2O_3 layers. Atomic layer deposition (ALD) was regarded as an ideal method for forming a well structured $\text{Al}_2\text{O}_3/\text{TiO}_2$ interface, because it offers high conformability ensuring uniform deposition onto the entire surfaces of nanoporous structures [67], low deposition temperatures (down to 33 °C for Al_2O_3) [68], and high resolution (~0.1 nm for Al_2O_3) for enhanced control of the film thickness [69, 70]. Hence, ALD provides a significant opportunity to enhance the PCE by providing advanced Al_2O_3 over-layers on TiO_2 electrodes of DSSCs. The chemical reactions of ALD Al_2O_3 overlayers on a titania substrate can be seen in reference [71] or in chapter 3.2.

One advanced report on enhancing the PCE of DSSCs by ~14% with atomic layer deposited Al_2O_3 over-layers on TiO_2 electrodes was provided in 2009 [19]. The optimal thickness for the ALD barriers was produced by 1 cycle of ALD (0.1 nm in nominal thickness), which resulted in an average increase in PCE of 14% among the 11 devices tested, with the highest achieved PCE being 7.82%. The TiO_2 electrode was 6 μm in diameter and

composed of two screen printed layers with different levels of porosity: a 12 μm thick nanoporous layer at the bottom (adjacent to the ITO electrode) formed with 20 nm TiO_2 nanoparticles, and a 4 μm thick scattering layer at the top formed with 200–400 nm TiO_2 particles. SEM images of these bilayers TiO_2 electrodes are shown in Fig. 2.17. The PCE enhancement for the DSSCs featuring the ALD- Al_2O_3 shell layers was not as significant as that for DSSCs with Al_2O_3 shell layers prepared by other methods, such as sol-gel coating. The unsatisfactory PEC enhancement can be ascribed to a low surface coverage of the ALD- Al_2O_3 shell layers on the nanoporous TiO_2 electrodes as a result of that the island growth mode prevails during the ALD deposition [53]. To further optimize the PCEs of DSSCs featuring Al_2O_3 / TiO_2 electrodes, it will be necessary to properly understand the dependence of the coverage of the Al_2O_3 over-layers on the number of the ALD deposition cycles.

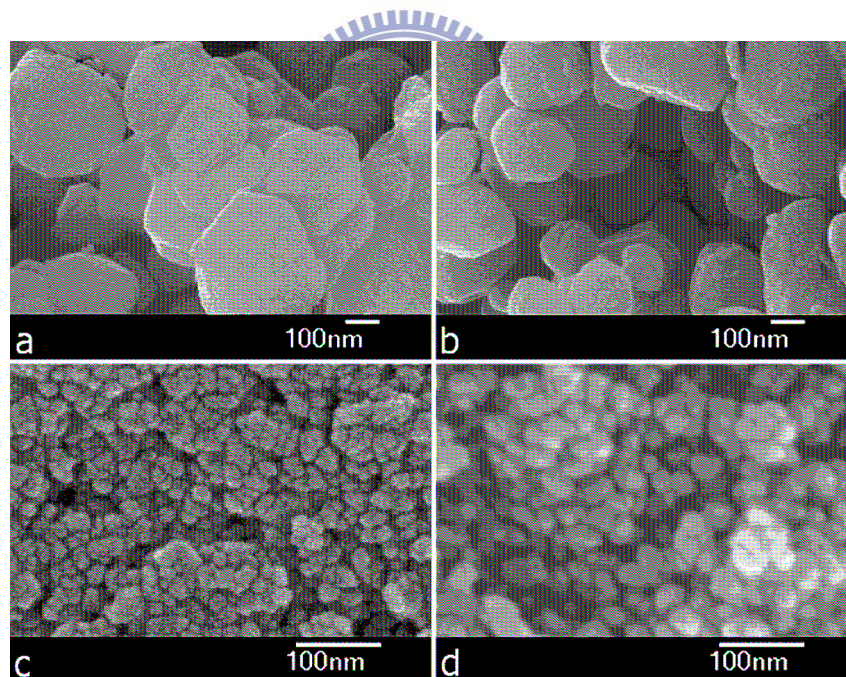


Figure 2.17 SEM images of the bilayer TiO_2 electrodes before and after application of a 1 nm ALD Al_2O_3 overlayer: (a) the scattering layer before ALD; (b) the scattering layer after ALD; (c) the nanoporous layer before ALD; (d) the nanoporous layer after ALD [19].

2.4 Interfacial Studies of Nanoporous TiO₂ Electrodes

The DSSCs have high conversion efficiency because they use the nano-structure as an electrode, which provided several thousands times more surface/interface area for dye/electrode. Enhancement of DSSC's efficiency by core/shell electrodes also relies on optimal interfacial properties between the core and the shell, such as energy levels, coverage and growth behavior. However, very few studies have addressed these properties. It is therefore of high interest to study the interfacial energy levels, coverage and growth behavior of core/shell electrodes.

2.4.1 Energy Levels of Dye/Electrode Interface

The high conversion efficiency may mainly rely on the interfacial energy matching between the dye and the electrode where initiates the charge separation, recombination and electron transfer. For example, the difference ($E_{\text{lumo}}-E_{\text{cb}}$) between the lowest unoccupied molecular orbital (LUMO) of dye and the conduction band (CB) edge of semiconductor presents a driving force at the interface for charge separation and electron injection [72]. Nevertheless, most researchers reported the relative energy levels at dye/electrode interface by estimation, studies seldom reveal the energy level or heterojunction of dye/electrode by accurate measurement from ultraviolet photoelectrode spectroscopy. As we know, the first study was in 2002, when Liu et al. aligned the energy levels of ZnPcGly-dye/TiO₂ interface of DSSCs and established the band diagram from ultraviolet photoelectron spectroscopy (UPS) as shown in Fig. 2.18 [73]. Accordingly, they concluded that the electron injection into TiO₂ electrode of the DSSC was very fast and efficient since the value of $E_{\text{lumo}}-E_{\text{cb}}$ was 0.1 eV. In 2005, J. E. Whitten used UPS to study four dyes/TiO₂ interfaces and compared their energy levels [74], he suggested the bandgap of the dye has a more significant effect on

device efficiency than the value of $E_{\text{lumo}}-E_{\text{cb}}$. In addition, Angelis et al. used density functional theory (DFT) to find that the energy levels of N719 dye changed by the adsorbing configurations as illustrated in Fig 2.19 [75] when N719 was coated on TiO_2 . Configuration B was considered more efficient interface than A because the value of $E_{\text{lumo}}-E_{\text{cb}}$ of configuration B was larger than that of A and the band gap of N719 was smaller.

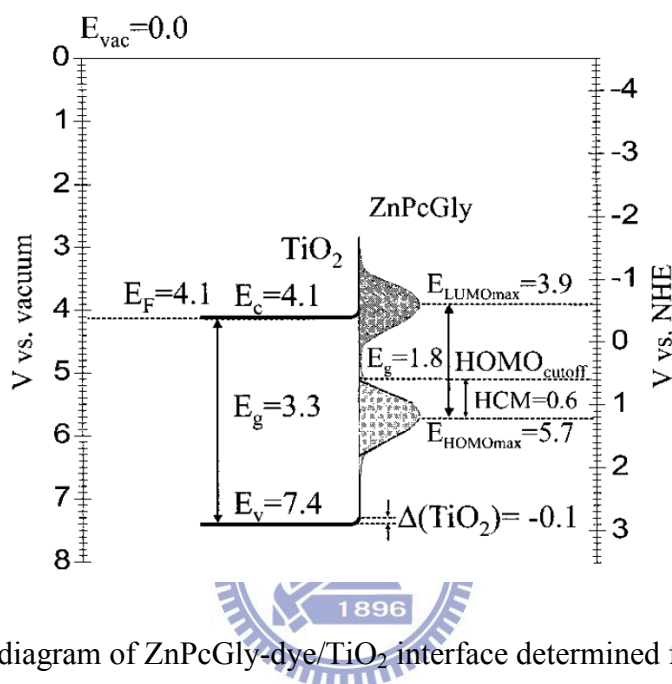


Figure 2.18 Energy diagram of ZnPcGly-dye/ TiO_2 interface determined from XPS and UPS measurements [73].

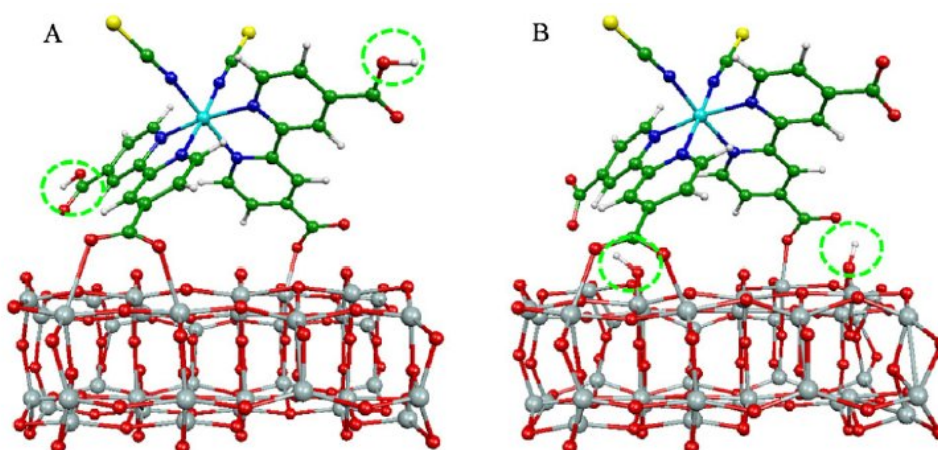


Figure 2.19 The A and B configurations of the N719 dye adsorbed on the TiO_2 nanoparticle [75].

The value of $E_{\text{lumo}}-E_{\text{cb}}$ is also an important factor to determine the efficiency of DSSCs with core/shell electrodes. C. Lin et al. compared the Fermi-levels of various thicknesses of Al_2O_3 shell layers on TiO_2 electrodes in DSSCs and found the conversion efficiency decreased to almost zero when the value of $E_{\text{lumo}}-E_{\text{cb}}$ was negative [19]. The variable value of $E_{\text{lumo}}-E_{\text{cb}}$ maybe induced from the dipole layer forming at the interface of $\text{Al}_2\text{O}_3/\text{TiO}_2$ [53]. Nonetheless, the relation between dipole layer and interfacial energy needs further study to be comprehensive. For example, the possible type of dipole layers in Figure 2.20 should be investigated at the interface of $\text{Al}_2\text{O}_3/\text{TiO}_2$ [76].

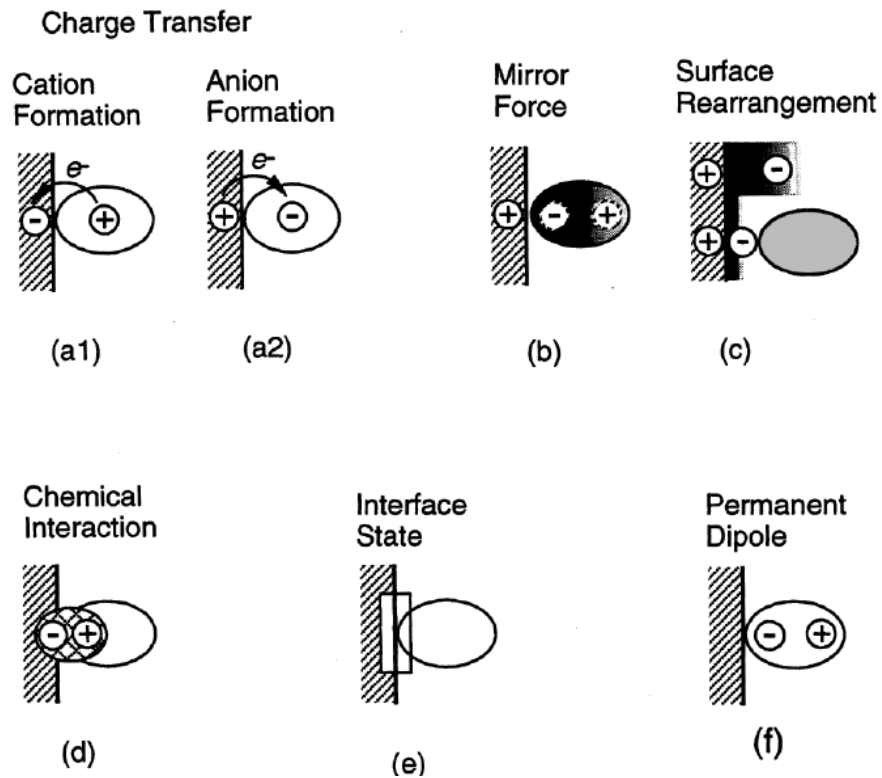


Figure 2.20 The possible type of dipole layers (a1) and (a2): Charge transfer across the interface, (b) Concentration of electrons in the adsorbate, (c) Rearrangement of electron cloud at the metal surface, (d) Chemical interaction, (e) Interface state introduced as a buffer of charge carriers, (f) Polar molecules or functional groups [76].

One of the appropriate methods to determine the dipole layer of ultra-thin alumina has been suggested by Song et al. as follows [77]. Figure 2.21 shows the work function (WF) or contact potential difference (CPD) of ultra-thin alumina as a function of oxygen exposure ($1\text{L } 10^{-6}\text{ torr}\cdot\text{s}$). Ideally, the binding energies of O 1s and Al 2p XPS peaks should be constant when oxide layer growth without the interfacial dipole layer in the $\text{Al}_2\text{O}_3/\text{substrate}$ interface. The binding energy shifts of O 1s and Al 2p XPS peaks shown similar trends as that of the WF and the CPD, which indicates the formation of the interfacial dipole layer at the interface. The strong decrease of WF and CPD was associated with the formation of interfacial dipole layer. The dipole layer was completed and the measured WF or CPD became stable with increasing the oxide layer thickness as well as the oxygen exposure.

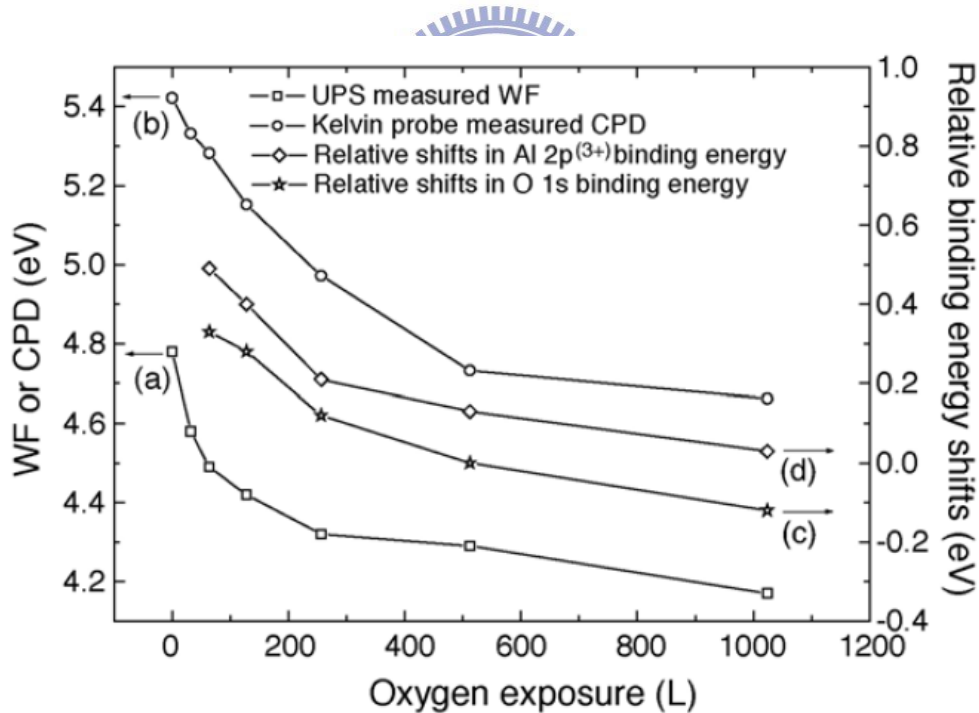


Figure 2.21 The changes of (a) work function (WF) measured by UPS, (b) CPD measured by Kelvin probe, (c) O 1s XPS peak and (d) Al 2p XPS peak in the Song et al. study [77].

2.4.2 Coverage of Adsorbed Materials on Electrodes

In previous studies, the coverage of dye/electrode interfaces was usually estimated by chemical desorption [78, 79]. The amount of adsorbed dye was determined by measuring the absorption spectra when desorbing the dye from the films with different thicknesses into KOH water solution. Fig. 2.22 shows that the absorbance (540 nm) of the dye solution is proportional with film weight, suggesting that the dyed in the films at all thicknesses are homogeneous. The standard absorbance was corrected for the film area (cm^2) and the volume (mL) of the decoloration solution. It is possible to estimate the average molecular number of dye molecules per colloid (using the particle with same diameter) from the standard spectrum. Ignoring the area loss from connection between particles and assuming that the adsorbed dye molecule covers 1 nm^2 per molecule, this number corresponds to a total surface coverage may be estimated.

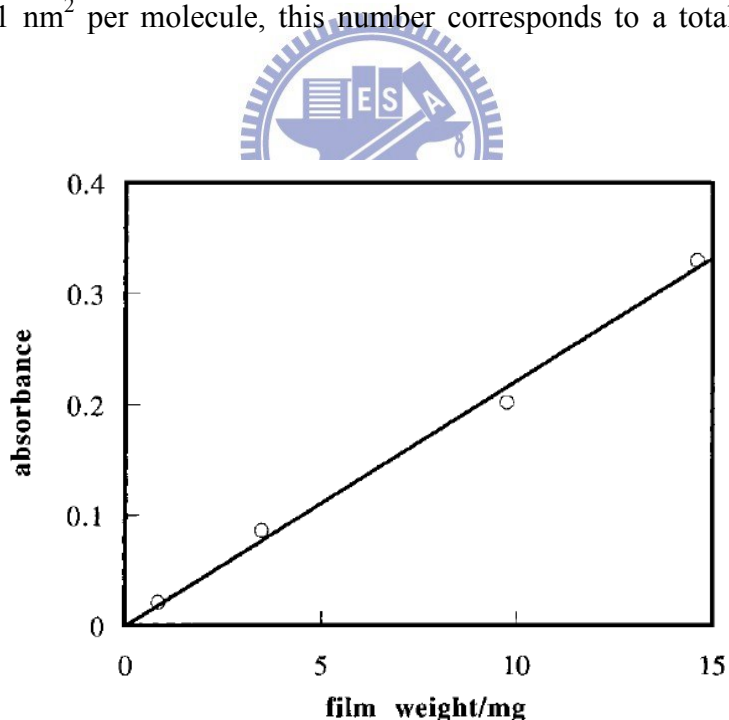


Figure 2.22 Absorbance of the desorbed dye in a 1 mM KOH water solution versus film weight for four electrodes of thicknesses 2.6, 7.7, 24, and 38 μm [78].

On the other hand, the coverage of shell/electrode interfaces can be estimated by the weighing method when the film is fabricated from solution [25]. For example, when the TiO_2 is coated on SnO_2 particles, by adding TiCl_4 solution into the SnO_2 colloid, we may calculate the coverage of TiO_2 on SnO_2 by using the unit $\mu\text{mol}/\text{m}^2$, where the μmol is quantity of TiCl_4 we added, and the m^2 is the total area of SnO_2 particles. Accordingly, the coverage data then revealed is shown in Table 2-3.

2.4.3 Growth Studies of Atomic Deposited Layers

In an attempt to enhance the PCE of the sol-gel process, Lin et al. employed ALD of Al_2O_3 to overcoat anatase based DSSCs [14]. Nevertheless, the final 14% PCE increase was lower than the 30-35% reported for the sol-gel technique [14, 15]. Tien et al. attributed the unsatisfactory results to a low Al_2O_3 coverage of the nano-porous TiO_2 film because of the island growth during ALD [80]. A complete understanding of the growth behavior of the Al_2O_3 overlayers is thus a basic step towards further PCE increases in DSSCs.

A method to determine the growth mode was suggested by Puurunen et al. [81, 82]. Figure 2.23 shows the four types of growth-per-cycle (GPC), via various number of ALD reaction cycles. The growth-per-cycle is defined as the amount of material deposited in an ALD reaction cycle, and referred to as GPC and will be discussed in chapter 6. Figure 2.23(a)-(d) represents the layer-by-layer growth mode, substrate-enhanced growth, substrate-inhibited growth and island growth, respectively. The growth mode by the changes of growth-per-cycle can be clearly identified from these plots. The effect of the substrate on the GPC is obvious in the beginning of the growth, when the substrate is not fully covered by the ALD-grown film. The effect of the substrate on the GPC is lost after the substrate surface

is completely covered by the ALD materials, and the GPC is expected to become constant.

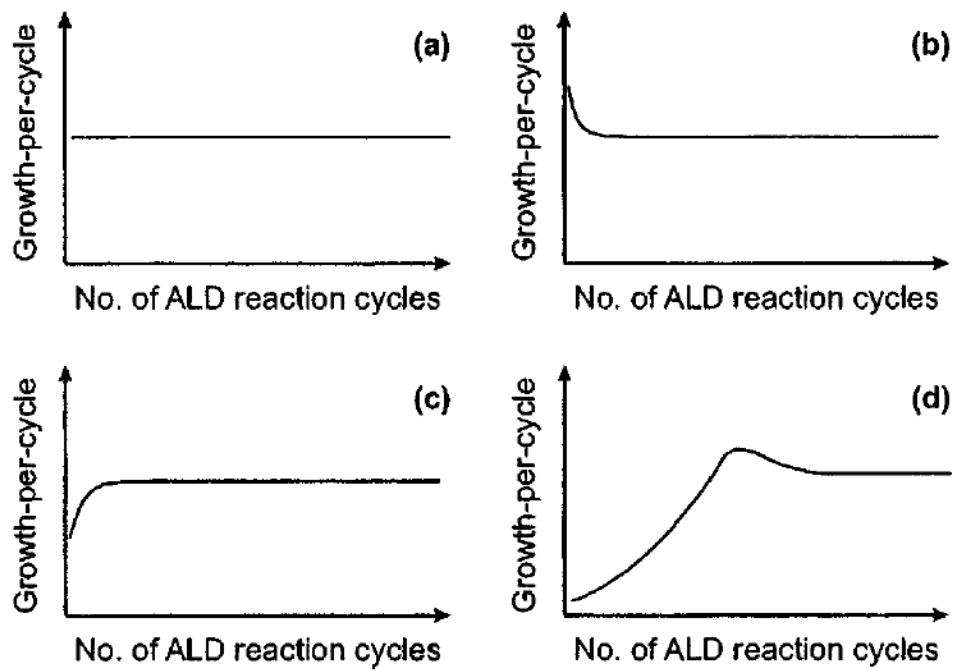
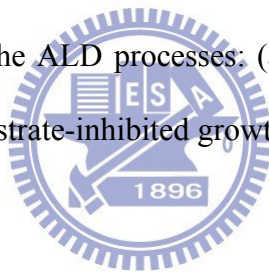


Figure 2.23 Growth-per-cycle for the ALD processes: (a) Layer-by-layer growth mode, (b) Substrate-enhanced growth, (c) Substrate-inhibited growth, and (d) Island growth [82].



Chapter 3

Experimental

3.1 Preparation of Porous TiO₂ Electrodes

The structure of the layers of the DSSCs employed in this study were fabricated as a transparent, conductive, glass/TiO₂ electrode with an optional ALD Al₂O₃ coating bis(tetrabutylammonium) salt of cis-di(thiocyanato)-N,N-bis(2,2'-bipyridyl-4,4'-dicarboxylic acid)-ruthenium(II), also known as N719 dye, then combined with electrolyte/Pt/transparent conductive glass. The transparent conductive glass (Nippon Sheet Glass Co., Ltd.) contains a fluorine-doped oxide (FTO) film with a sheet resistance of 10-12 Ω/cm^2 . The TiO₂ electrode was 6 mm in diameter and composed of two screen-printed layers, i.e., a 12- μm -thick nanoporous layer at the bottom (active layer) formed with ~ 20 nm TiO₂ nanoparticles and a 4- μm -thick scattering layer at the top formed with TiO₂ particles in the size range of 200-400 nm. The ~ 20 -nm TiO₂ nanoparticles were identified as anatase phase and prepared from following procedure: A volume of 37 mL of titanium(IV) isopropoxide (Aldrich, 99.9%) in 10 mL of 2-propanol was slowly dripped over 30 min into a stirred mixture of 80 mL of glacial acetic acid and 250 mL of deionized water at 0 °C. The resulting solution was heated to 80 °C for 8 h. It was then heated to 230 °C for 12 h in a titanium autoclave. When the solution was removed from the autoclave, it was sonicated for 5 min with a cell disrupter with an approximate power of 250 W. The solution was then concentrated to 150 g/L. A 4 g sample of CarbowaxTM (Dow Chemical Company) was added and it was stirred overnight.

3.2 Fabrication of Al₂O₃ Shell Layers

The Savannah S100 Atomic Layer Deposition (ALD) system made by Cambridge NanoTech Corporation and shown in figure 3.1, is used for the deposition of Al₂O₃ on TiO₂ electrodes. In the ALD system, substrate size may reach to 100 mm and substrate temperature can heat to 450 °C. The other specifications of Savannah S100 are listed as follows: deposition uniformity of Al₂O₃ is <1%, precursor delivery system may compose of 6 lines and each line can heat to 200 °C independently, high speed ALD valves with 10 msec response time, 50 ml stainless steel precursor cylinders may heat to 315 °C individually, the mass flow of carrier/venting gas (N₂ or Ar) may up to 100 sccm.

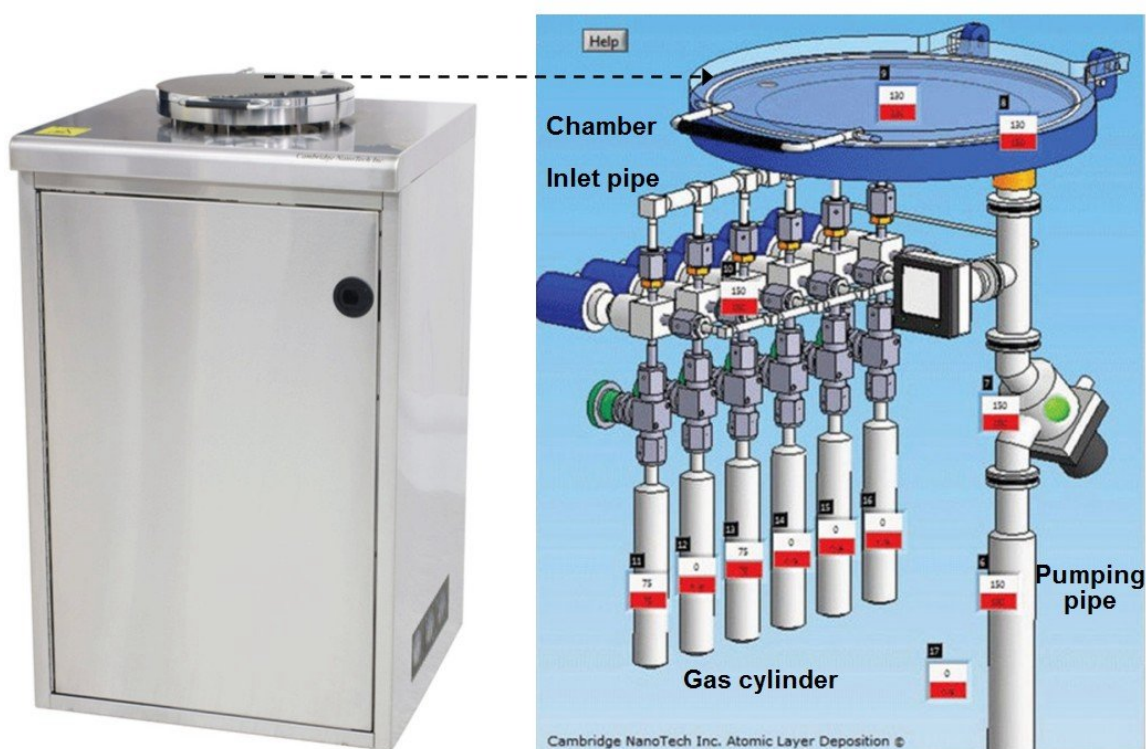
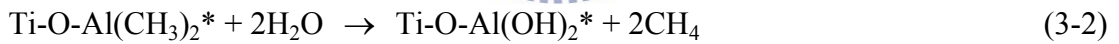
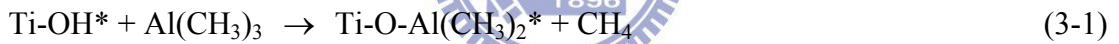
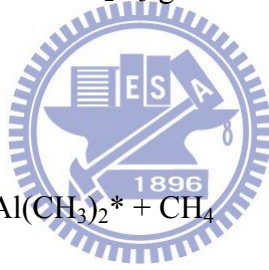


Figure 3.1 The appearance and schematic layout of Savannah S100 Atomic Layer Deposition (ALD) system made by Cambridge NanoTech Corporation.

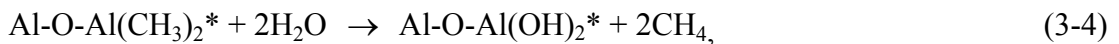
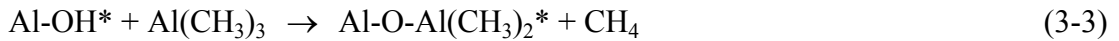
In this study, the atomic layer of Al₂O₃ was deposited on the TiO₂ electrodes used

$\text{Al}(\text{CH}_3)_3$ (trimethylaluminum, TMA) and H_2O as precursors and a deposition temperature of $150\text{ }^\circ\text{C}$. The ALD process consisted of a given number of identical cycles, each containing the following 6 steps: dosing with H_2O for 0.05 s, soak in the H_2O dose for 2 min, evacuation for 5 min, dosing with TMA by opening the TMA valve for 0.05 s, soak in the TMA dose for 2 min, and evacuation for 5 min. After the precursors were carried with nitrogen at a constant flow rate of 20 sccm with gas pressure 1.0 Torr and precursor/nitrogen ratio 1:10, the chamber was closed for the subsequent soaking process.

Deposition of Al_2O_3 overlayers on a titania substrate, using $\text{Al}(\text{CH}_3)_3$ and H_2O as the precursors, can be separated into two consecutive stages: (1) aluminum hydroxide formation on the titania surface and (2) continuous Al_2O_3 growth. The first stage can be represented by the following reactions [71]:



where the asterisks denote the surface species. Similarly, the continuing growth of the Al_2O_3 overlayer can be summarized by the two consecutive reaction steps:



where again the asterisks indicate surface species. According to the above reaction equations, at the end of each ALD reaction cycle, the sample is covered by hydroxyl surface groups.

The TiO₂ electrodes with or without the ALD Al₂O₃ overlayer were sensitized with the N719 dye to saturation in an N₂ glove box. The content of the electrolyte solution was as follows: 0.1 M LiI, 0.03 M I₂, 0.5 M tert-butylpyridine, and 0.5 M 1,2-dimethyl-3-propylimidazoliumiodide (PrMeImI) in anhydrous acetonitrile. An illustration of the layer structure of the DSSCs employed in this study is shown in Fig. 3.2.

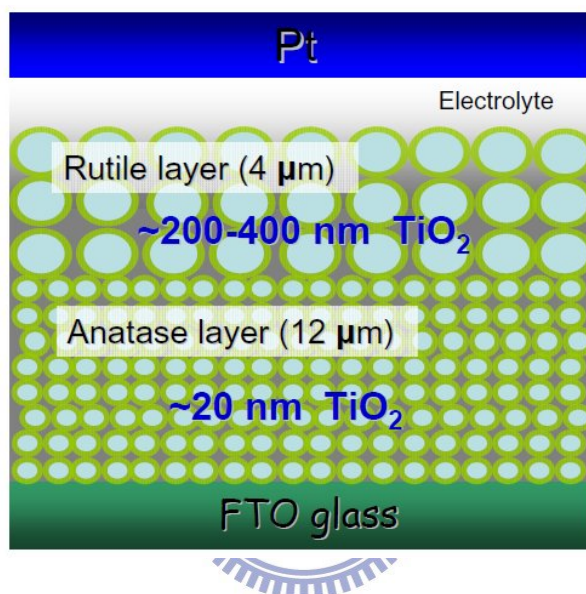


Figure 3.2 Illustration of the layer structure of the DSSCs employed in this study.

3.3 Cell Characterization

The photocurrent-voltage characteristics of the DSSCs were measured under AM 1.5G illumination simulated with a Yamashita Denso solar simulator (YSS-100A) as shown in figure 3.3. I-V characteristics were measured by a source meter (Keithley 2400) controlled by an original software under irradiation of the solar simulator.



Figure 3.3 The appearance of Yamashita Denso solar simulator (YSS-100A).

The power conversion efficiency (PCE,) of the dye-sensitized cell is determined by the following equation:

$$= J_{sc} \times V_{oc} \times FF / I_s \quad (3-5)$$

where the J_{sc} is the photocurrent density measured at short circuit, the V_{oc} is open-circuit photo-voltage, FF is the fill factor of the cell and equal to $J_{Max} \times V_{Max} / J_{sc} \times V_{oc}$ (see Figure 2.3) and I_s is the intensity of the incident light. The maximum power (P_{Max}) is equal to $J_{Max} \times$

V_{Max} at where the power output of the cell is maximal. Then the fill factor of the cell can be calculated with the following equation:

$$FF = P_{Max} / J_{sc} \times V_{oc} \quad (3-6)$$

Efficiency of the solar cells were measured under the international standard reporting conditions (SRC) such as 100 mW/cm² total irradiance, AM 1.5G reference spectrum and 25 cell temperature. The current AM 1.5G reference spectrum used by the international terrestrial photovoltaics community is from International Electrotechnical Commission (IEC) Standard 60904-3.

3.4 Characterization of the Core/Shell Electrodes

The TEM analysis of the TiO₂ electrodes was done using a field-emission transmission electron microscope (JEOL, JEM-2100f) with a 0.1-nm lattice resolution. Ultraviolet photoelectron spectroscopy (UPS), x-ray photoelectron spectroscopy (XPS), and reflective electron energy loss spectroscopy (REELS) analyses of the TiO₂ electrode were performed using a combined electron spectroscopy (VG ESCA lab 250) as shown in figure 3.4 with a base pressure of 1x10⁻¹⁰ torr, and with the sources of Al K α (h ν =1486.6 eV) for XPS, He I radiation (h ν =21.22 eV) for UPS, and electron beam (kinetic energy=17 eV) for REELS. The lattice structure of the samples was studied by X-ray diffraction (XRD) using an X-ray diffractometer (Philips-PW3710) operated at a scanning step of 0.02^o/s. The basic processes of UPS, XPS, REELS, TEM and XRD are described next.

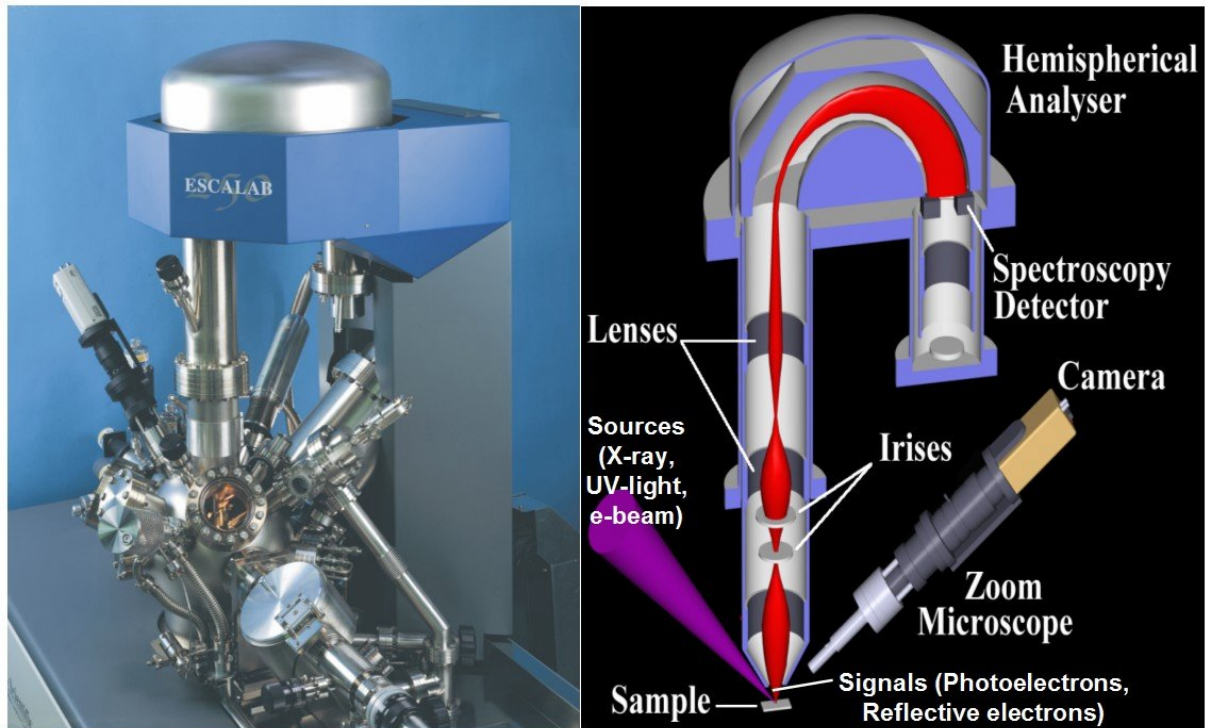
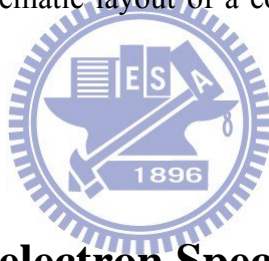


Figure 3.4 The appearance and schematic layout of a combined electron spectroscopy (VG ESCALab 250).



3.4.1 Ultraviolet Photoelectron Spectroscopy (UPS)

A simple UPS process of photoemission is shown in Fig. 3.5, where the incident ultraviolet (UV) light resulted in the escape of photoelectron from valence band. Typical UV sources are He gas discharges and synchrotron radiation. The kinetic energy of the photoelectron (E_k) can be detected by spectrometer and expressed by the following equation [76]:

$$E_k = h\nu - E_b \quad (3-7)$$

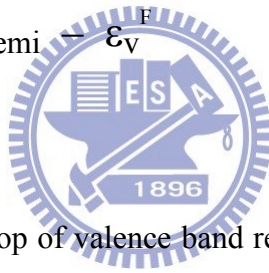
where $h\nu$ represents the energy of incident UV light, E_b is the binding energy of the electron before excitation relative to the vacuum level. When a metal is under the excitation of UPS,

the work function of the metal (Φ_m) can be determined by

$$\Phi_m = h\nu - E_{\text{metal}} \quad (3-8)$$

where the E_{metal} is the energy difference between the minimum kinetic energy of the electron and the energy at Fermi edge (Fermi level). On the other hand, when a semiconductor or insulator is under the excitation of UPS, the work function of the semiconductor or insulator (Φ_i) is ideally determined by the following equation,

$$\Phi_i = h\nu - E_{\text{semi}} - \varepsilon_V^F \quad (3-9)$$



where the ε_V^F is the energy at the top of valence band relative to Fermi level, E_{semi} is the energy difference between the minimum kinetic energy of the electron and the energy at the top of valence band. It should be noted that when the $h\nu$ is known and the E_{semi} , ε_V^F are measured from UPS spectrum, then the work function of materials can be acquired from above equations.

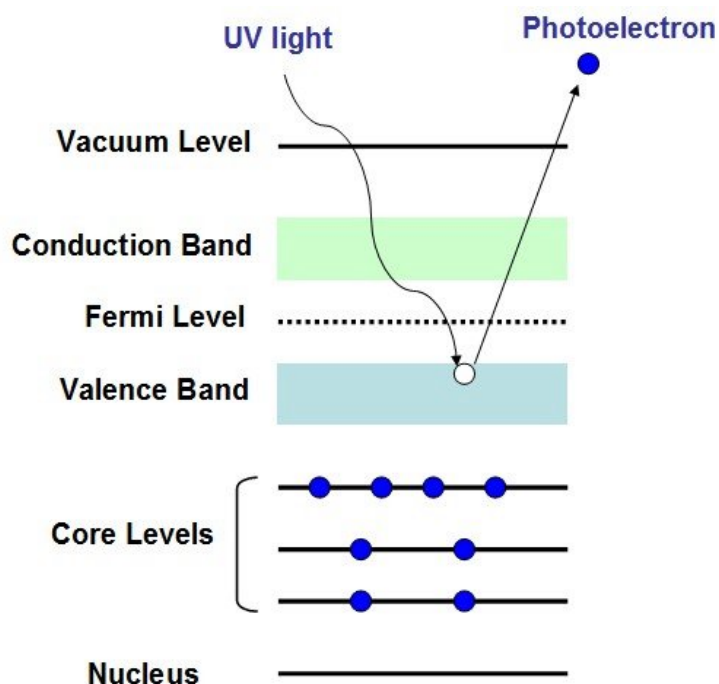


Figure 3.5 Schematic diagram shows the UPS process of photoemission.



3.4.2 X-Ray Photoelectron Spectroscopy (XPS)

The simple XPS process of photoemission is shown in Fig. 3.6, where the incident X-ray resulted in the escape of photoelectrons from the core level and the valence band. Typical X-ray sources are Mg $K_{\alpha 1,2}$, Al $K_{\alpha 1,2}$ and synchrotron radiation. The measuring principle and basic equation of XPS are the same with UPS such as equation 3-7 except for the energy level where the photoelectrons originate. UPS is more sensitive at the valence band, because the incident light used lower energy; in addition, UPS can not acquire the core level information due to the low energy of incident UV light not inducing photoelectron from core level.

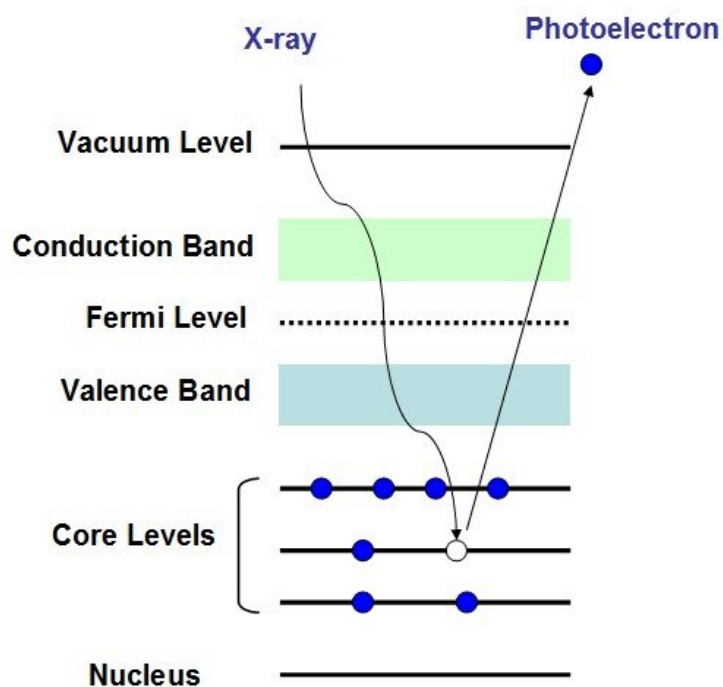


Figure 3.6 Schematic diagram shows the XPS process of photoemission.

3.4.3 Reflective Electron Energy Loss Spectroscopy

(REELS)

In REELS we are concerned with the specific electron with a lowest energy loss in the spectrum, that is, the reflective electron induces the excitation from valence band maximum (VBM) to conduction band minimum (CBM). The specific REELS process is shown in Fig. 3.7, where the incident electron beam results in an electron jump from VBM to CBM. The kinetic energy of the reflective electron with lowest energy loss ($E_{\text{lowest loss}}$) can be detected by spectrometer and expressed by following equation.

$$E_{\text{lowest loss}} = E_{\text{beam}} - E_{\text{band gap}} \quad (3-10)$$

where the E_{beam} is the energy of electron beam, $E_{\text{band gap}}$ is the energy of band gap. Then, we can calculate the $E_{\text{band gap}}$ from equation 3-10.

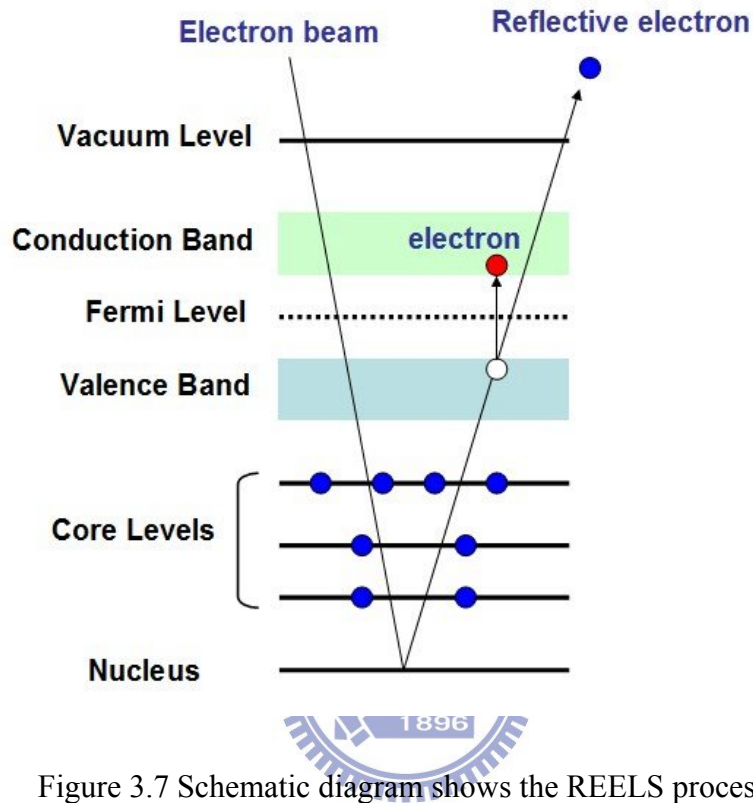


Figure 3.7 Schematic diagram shows the REELS process

3.4.4 Transmission Electron Microscopy (TEM)

Based on the same basic principle with optical microscopy, TEM uses the electron beam transmitted through an ultra thin specimen and forming an image. The basic principle was started in 1873, the optician Ernst Abbe developed the Abbe's theoretical relationship calculated the minimum resolvable separation d_0 of an image formed by a microscopy as follows:

$$d_0 = 0.61\lambda / n \sin \alpha \quad (3-11)$$

where λ is wavelength of the illuminant, α is the half the angle of the cone of illuminant from specimen plane accepted by the objective (half aperture angle in radians), n is refractive index in the space between object and objective lens. Theoretically, the relationship could calculate the limit of resolution of any microscopies included TEM. The wavelength of the illuminant used in TEM was expressed by de Broglie equation:

$$\lambda = 1.23/V^{1/2} \text{ nm} \quad (3-12)$$

where V is the voltage applied on the electron source. Eq. 3-11 and Eq. 3-12 provide the foundation of high image resolution in TEM. For example, if $n \sin \alpha$ is 1.4, then the image resolution of a 50 kV TEM could reach to 0.0024-nm, or 0.024-Å; however, in the real case, 200 kV TEM (JEOL, JEM-2100f) may has a 0.1-nm lattice image resolution which is lower than theoretical capability.

3.4.5 X-ray Diffraction (XRD)

A x-ray diffraction process is shown in Fig.3-8, where the incident X-ray in a crystal results in the reflective x-ray that following the bragg law:

$$n\lambda = 2d \sin \theta \quad (3-13)$$

where n is the order of diffraction corresponding to $n = 1, 2, 3, \dots$, λ is wavelength of x-ray,

d is distance between crystal planes, θ is the angle between incident x-ray and crystal plane.

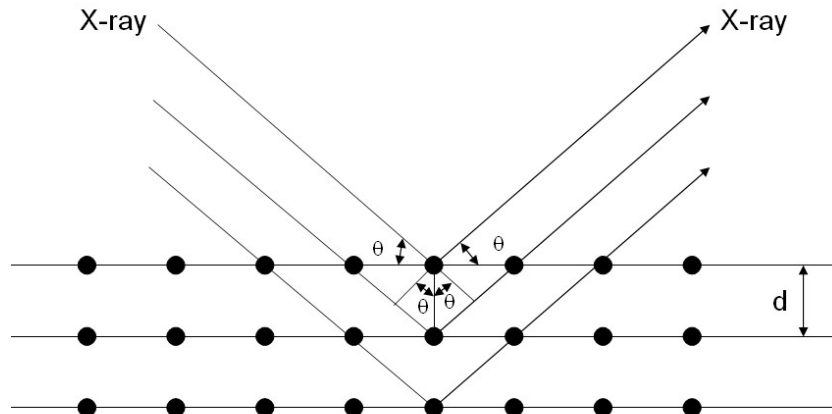


Figure 3.8 Schematic diagram shows the XRD process

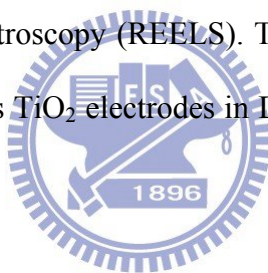
XRD generally used to identify the crystalline materials or to determine the crystal phase of materials. In this study, we used XRD to provide the lattice constant of crystalline core-materials. By comparing the experimental XRD data and the standard data from International Center Diffraction Data (ICDD) or formerly known as Joint Committee on Powder Diffraction Standards (JCPDS), we can evaluate the lattice strain for the electrode. The standard database is available from the diffraction equipment manufacturers or from ICDD.

Chapter 4

Interfacial Energy Levels of Al₂O₃ Films on TiO₂

Electrodes of Dye-Sensitized Solar Cells

To achieve a comprehensive study of the physical, chemical, and electrical properties of the Al₂O₃ overlayers, we studied the ALD Al₂O₃/TiO₂ electrodes on the interfacial energy level. We examine low-temperature ALD process for forming the Al₂O₃ barriers to achieve compatibility with low-temperature DSSCs fabrication processes. The interfacial energy level related to power conversion efficiency (PCE) were investigated by using TEM, ultraviolet photoelectron spectroscopy (UPS), x-ray photoelectron spectroscopy (XPS), and reflective electron energy loss spectroscopy (REELS). The nano-structure and the influence of ALD Al₂O₃ layers on nanoporous TiO₂ electrodes in DSSCs were also studied using these characterization techniques.



4.1 Microstructure and Chemical Analysis

The TEM images in Fig. 4.1(a) show the nanocrystalline TiO₂ without the ALD Al₂O₃ overlayer; Fig. 4.1(b) shows the nanocrystalline TiO₂ with the 10-cycles ALD Al₂O₃ overlayers. Both of the samples presented spherical-like, uniform, interconnected TiO₂ nanoparticles that were about 20 nm in size. The uniform, over-coated Al₂O₃ layers can be seen in part of the TEM image have been identified as amorphous structure by XRD. The thicknesses of 1-cycle, 2-cycle, 5-cycle, 10-cycle, and 20-cycle ALD Al₂O₃ overlayers determined by TEM, which are about 0.2 nm, 0.5 nm, 1.0 nm, 1.9 nm and 2.8nm, respectively, indicated a significant discrepancy of deposition rate (nm/cycle) for different cycles. The

discrepancy may be ascribed to the growth-per-cycle (ΔC_M) of the ALD Al_2O_3 layers, as shown in the equation (4-1) [81]:

$$\Delta C_M = \Delta h \times (\rho N_A / M) \quad (4-1)$$

where the ΔC_M defined as the number of atoms M (here is Al) adsorbed per unit surface area per cycle, Δh is the thickness increment per cycle, ρ is the density of layer and N_A is the number of atoms per mole ($6.02214 \times 10^{23} \text{ mol}^{-1}$), M is the molar mass of layer. By substituting the $M=50.98 \text{ g/mol}$ and $\rho= 2.9 \times 10^{-21} \text{ g/nm}^3$ [68] into the equation, Fig. 4.1(c) shows the growth-per-cycle of Al_2O_3 layers via the Al_2O_3 thickness increment per cycle. The growth-per-cycle increased to a maximum and then decreased to the steady value, referred to as substrate-inhibited growth of the ALD Al_2O_3 layers. This result is consistent to Puurunen's study suggested island growth as the origin of this type of substrate-inhibited growth in ALD Al_2O_3 layers [82].

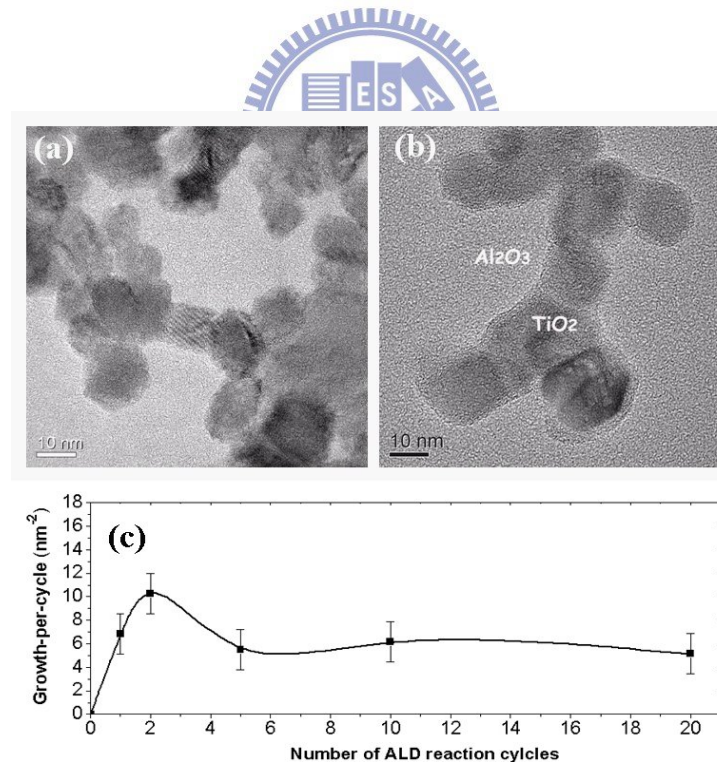


Figure 4.1 (a) TEM image of the nanocrystalline TiO_2 without ALD Al_2O_3 overlayer. (b) TEM image of the nanocrystalline TiO_2 with 10-cycles ALD Al_2O_3 over-layer. (c) Result of the growth-per-cycle of Al_2O_3 layers via the Al_2O_3 thickness increment per cycle.

After the peak fitting was performed by using the Shirley background subtraction and Gaussian/Lorentzian functions, the normalized XPS spectrum of the as-received TiO₂ electrode shown in Fig. 4.2(a) indicates that the Ti 2p_{3/2} core level of the nanoporous TiO₂ electrode located at 458.9 eV lies within the range of 458.8-459.4 eV reported in the literature for TiO₂ [83, 84]. Therefore, charging effects and subsequent shifts in the photoelectron peak positions were considered to be negligible. Following the ALD process, first, the binding energy of the Ti 2p_{3/2} core level was shifted by -0.4 eV to 458.4 eV and then shifted by +0.3 eV to 458.7 eV after the deposition of 10-cycle Al₂O₃ over-layers. These shifts of the Ti 2p_{3/2} core levels partially indicated an air-surface reaction existing within the 0.2-nm thickness of the Al₂O₃ over-layer. The interfacial reaction can be seen more clearly in the Al 2p spectra shown in Fig. 4.2(b). There are two groups of the Al 2p peaks, named S1 and S2, in the Figure. The S1 peaks located at 74.1 eV were identified as Al₂O₃ according to previous literature [84], and they shifted by 0.5 eV to 74.6 eV after 10-cycle deposition. Another peak, which was labeled S2 and shifted from 75.8 eV to 76.1 eV, was identified as Ti-O-Al(OH)₂, according to our previous model [19]. In our previous model, the thickness of a 1-cycle Al₂O₃ overlayer equals that of the Ti-O-Al(OH)₂ monolayer, or 0.3 nm, which is close to our measured values. It should be noted that the Ti-O-Al(OH)₂ and Al₂O₃ were formed when the sample's surface reacting to the atmosphere, there is another one like "Ti-O-Al(OH)-O-Ti", with only one hydroxyl on Al atom to maintain a constant growth rate each cycle, should exist in ALD vacuum chamber. The fact that the S2/S1 peak area ratios listed in table 4-1 were inversely proportional to the number of cycles indicates that the Ti-O-Al(OH)₂ monolayer, which is located close to the Al₂O₃/TiO₂ interface, could be a possible cause of the negative binding energy shifts of the Ti 2p_{3/2} core levels.

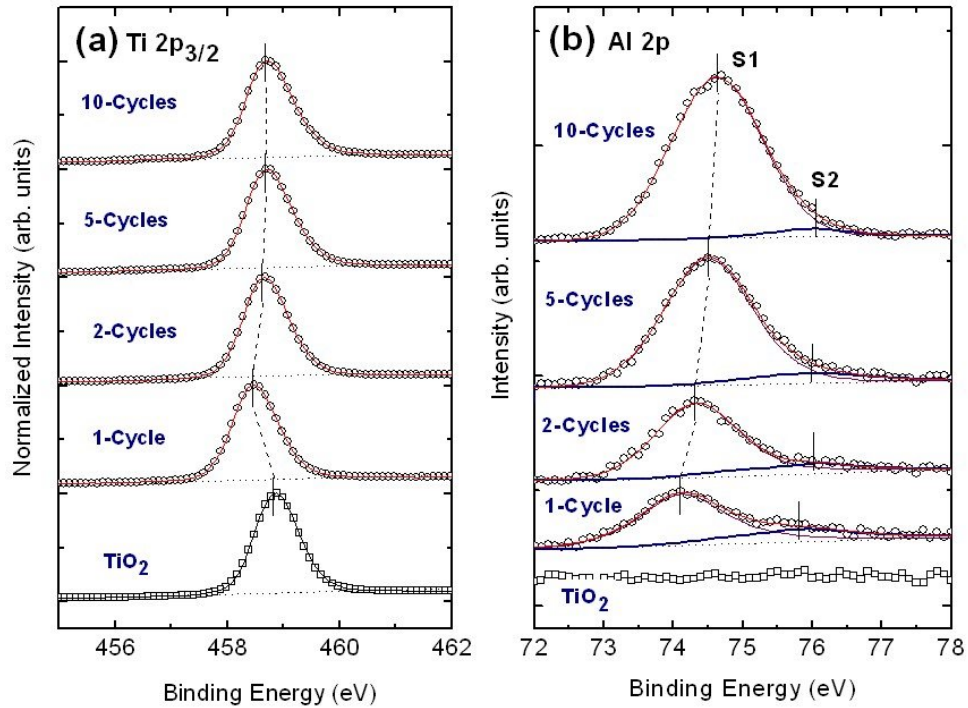


Figure 4.2 XPS results showing (a) $Ti2p_{3/2}$ and (b) $Al2p$ core level photoelectron peaks from ALD Al_2O_3 coated TiO_2 electrodes.

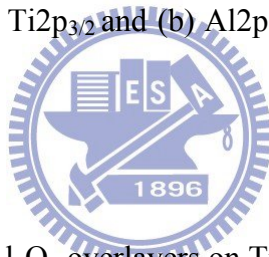


Table 4-1 XPS results of the ALD Al_2O_3 overlayers on TiO_2 electrodes.

Deposition cycles	$Ti2p_{3/2}$ Binding energy/ Relative shift(eV)	S1 Binding energy/ Relative shift(eV)	S2 Binding energy/ Relative shift(eV)	S2/S1 ratio
0 cycle	458.8/ 0	-----	-----	-----
1-cycles	458.3/ -0.4	74.1/ 0	75.8/ 0	0.3
2-cycles	458.3/ -0.2	74.3/ 0.2	76.1/ 0.2	0.08
5-cycles	458.7/ -0.1	74.5/ 0.4	76.0/ 0.1	0.08
10-cycle	458.7/ -0.1	74.6/ 0.5	76.0/ 0.1	0.03

4.2 Interfacial Energy Levels Analysis

UPS is a powerful technique for measuring the valence band maximum (VBM) and work function (WF) of ultra-thin film; in addition, it gives the most directive figure about the energy level alignment at the interface between two layers [76]. Figures 4.3(a) and 4.3(b) show the UPS spectra obtained from the as-received and ALD-deposited TiO_2 electrodes. The

VBM relative to the Fermi-level (E_F) was determined by the values of cutting points in the VB region of UPS assuming that E_F is 0 eV, and the resulting values are listed in table 4-2. Following the ALD process, the VBM was shifted by 0.9 eV from 3.7 eV to 4.9 eV, which is larger than the shifts in core levels, and it is believed that the VBM shifted toward the reported value of 5.6 eV for pure Al_2O_3 thin film [85]. On the other hand, the work function (WF) was measured from the values of cutting points in the secondary electron (SE) region of the UPS, as can be seen in Fig. 4.3(b). It should be noted that the WF of ultra-thin Al_2O_3 overlayers increased from 4.7 eV to 5.1 eV at the surface in the first ALD cycle process, which indicates that the band is bending downward across the surface to the interface, and the difference of WF, which induced a 0.4 eV built-in potential (V_{bi}), accelerated the electron transport from Al_2O_3 over-layers to the TiO_2 electrode. The WF of ultra-thin Al_2O_3 overlayers decreased with subsequent 2-10 cycle ALD deposition and shifted to 4.4 eV after the 10-cycle ALD deposition process. A similar trend was found in the reference [86], where the interfacial dipole layers were regarded as the main factor that determined the work function of ultra-thin Al_2O_3 films on a Cu-9%Al surface. The thickness dependence of the WF for the Al_2O_3 overlayers revealed the interfacial charge stability of the dipole layers, and this is shown in Fig. 4.4.

Table 4-2 Thickness, energy levels of the ALD Al_2O_3 overlayers of the DSSCs.

Deposition cycles	Al_2O_3 Thickness (nm)	VBM (B.E., eV)	Work function (eV)	Band gap (eV)	Electron affinity (eV)
0 cycle	0	3.7	4.7	3.9	4.5
1-cycles	0.2	3.7	5.1	4	4.8
2-cycles	0.5	3.8	4.8	4.3	4.3
5-cycles	1.0	4.3	4.6	5.1	3.8
10-cycle	1.9	4.6	4.4	5.9	3.1

The REELS spectrum of as-received TiO_2 in Fig. 4.3(c) shows that the onset of electron

signals located at 3.9 eV lies within the band gap value reported in the literature for nano-crystalline TiO₂, which indicated the blue-shift or quantum confinement compared to 3.2 eV for a large grain size of TiO₂ [87, 88]. By considering the depth sensitivity in the REELS spectra, we calculated the depth of electron penetration (X) from the following equation [89]:

$$X (\mu\text{m}) = 0.1E^{1.5}/d \quad (4-2)$$

where E is the e-beam energy (KeV), and d is the sample density (g/cm³) in the REELS spectra. Substituting the experimental e-beam energy value (17 eV), ALD Al₂O₃ density value (2.9 g/cm³) [68], and TiO₂ density value (3.893 g/cm³, JCPDS-ICDD No:31-1272) into the equation (4-2), the resulting depths of electron penetration in our REELS analysis were determined to be about 0.07 nm for Al₂O₃ and about 0.05 nm for TiO₂ materials. This result may guarantee that our REELS spectra are depth-sensitive enough to the Al₂O₃ over-layers for measuring their band gap. After the deposition of the Al₂O₃ overlayers, the onset of electron signals shifted from 4.0 eV to 5.9 eV as the thicknesses of the Al₂O₃ over-layers increased as shown in Fig. 4.3(c). The trend are similar to the earlier reports that used REELS to measure the band gap of Al₂O₃ ultra-thin films from 2.5 eV for the surface to 8.7 eV for the bulk state, and the lower band gap value is mainly due to structural surface states, such as defects, Al sp_z dangling bond [90], and the amorphous structure [91]. The present results are consistent with earlier findings in REELS studies that suggested that the band gap of the Al₂O₃ overlayer is positively correlated with its thickness at the sub-nanometer scale due to the fact that the ratio of reflective electrons from structural surface-states is a major portion of the REELS spectra in ultra-thin Al₂O₃ films.

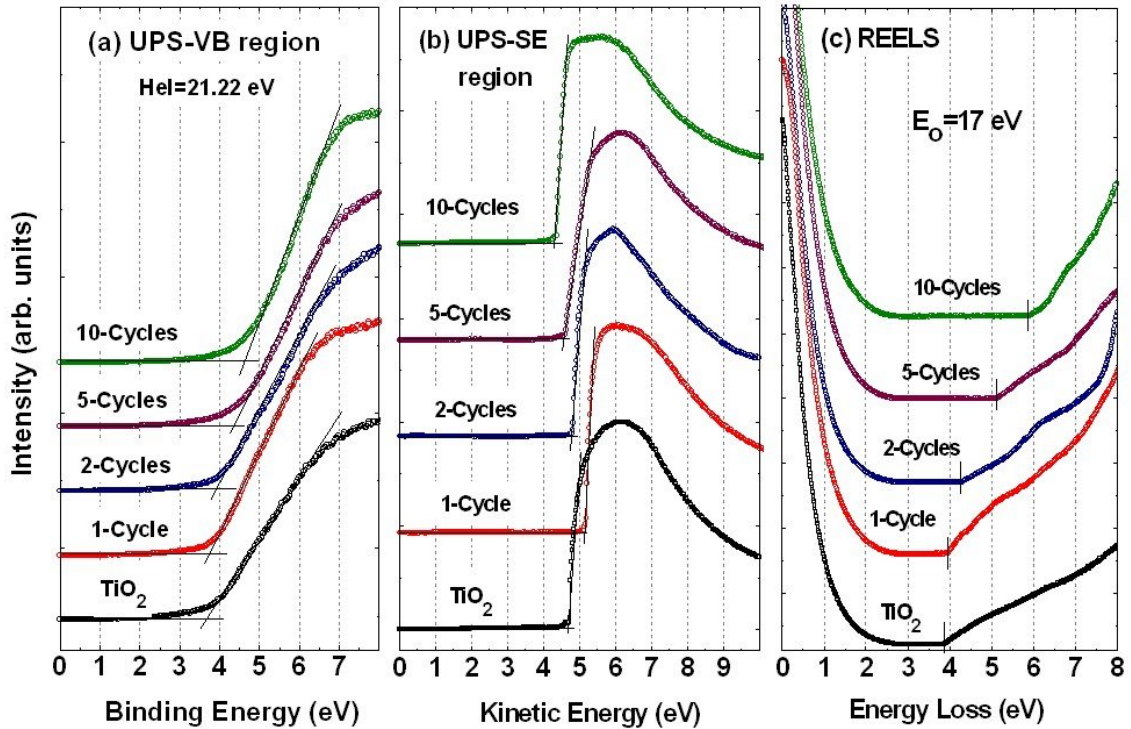


Figure 4.3 (a) UPS valence band region and (b) UPS secondary electron region of the as-received and ALD Al_2O_3 deposited TiO_2 electrode. (c) REELS spectra of the as-received and ALD deposited TiO_2 electrode.

The work function (WF) changes as a function of the thickness of the Al_2O_3 over-layers (Fig. 4.4), indicate that the magnitude and the direction of the core level shifts are in excellent agreement with the decrease in WF. The measured WF of the pure, nanoporous TiO_2 electrode was 4.7 eV, which is close to the WF of 4.8 eV of the pure TiO_2 (110) surface [92]. Following the deposition of the Al_2O_3 over-layers, the shifts of Ti $2p_{3/2}$ and Al $2p$ XPS peaks showed a similar trend to that of the WF. Significant changes of WF and Ti $2p_{3/2}$ core level by 0.4 eV at about a 0.2-nm thickness of Al_2O_3 deposition indicate the occurrence of an interfacial reaction between the Al_2O_3 over-layer and the TiO_2 electrode. This could be due in part to the formation of Ti-O-Al(OH)_2 , as previously mentioned when we discussed Fig. 4.2. The reduction of WF, when the thickness of the Al_2O_3 over-layers exceed 0.2 nm, was associated with the increase of binding energy of Ti $2p_{3/2}$ and Al $2p$ core levels. These results

were consistent with previous studies [77, 86], and they could be attributed to the interfacial Ti-O-Al(OH)₂ and the formation of dipole layers, which stabilized after the formation of two Al₂O₃ layers.

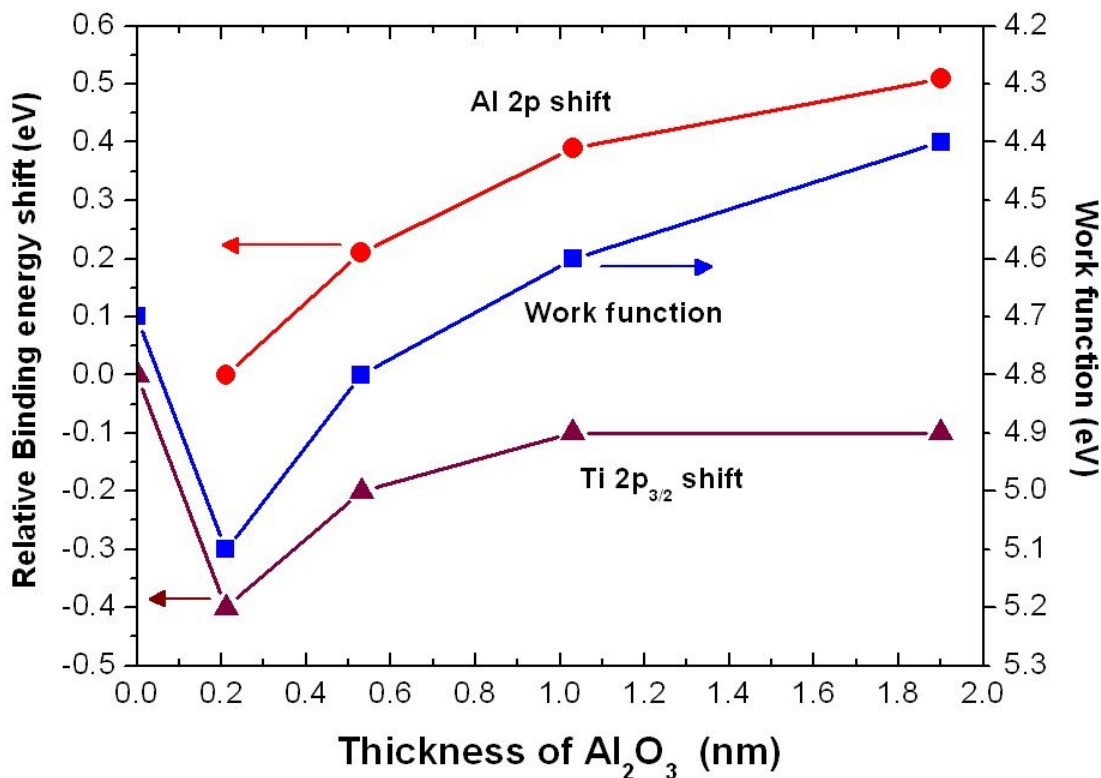


Figure 4.4 Changes of the work function, Ti2p_{3/2} XPS peak and Al2p XPS peak with various thicknesses of Al₂O₃ layers.

We have repeated the UPS/XPS and REELS measurements several times, indicating the data's error less than 0.1 eV. The accuracy or resolution of our data was calibrated before every spectral experiment by following analysis: The “resolution” of our electron spectroscopy determined as the energy between 80% to 20% intensity of pure Ag Fermi-edge was ~98 meV. But the real ability to resolve signals was determined as ≤20 meV using the same spectral condition in this study and tested a pure Ag surface from sample bias in the range of -5.00 eV to -5.04 eV by increments of 0.02 eV. The UPS deviations were smaller than 0.005 eV, and it could be assured that the resolving power was ≤ 0.02 eV. Therefore, the

larger data's error was mainly resulted from the deviations of samples preparation.

4.3 Energy Level Alignment at the Interfaces of Al₂O₃/TiO₂ Electrodes

The measured power conversion efficiency (PCE) of the DSSCs in Table 4-3 shows that the optimal ALD Al₂O₃ layer thickness is one monolayer, or 0.2 nm, which is considerably thinner than the reported 0.9-2.5 nm for sol-gel Al₂O₃ films. As discussed in our previous work, we ascribe this discrepancy to the limited film-thickness resolution of the sol-gel method, in which the minimum achievable Al₂O₃ thickness was ~1 nm, and the poorer infiltrating ability of the liquid precursors of the sol-gel process, which tends to cause overestimation of the Al₂O₃ thickness (i.e., the sol-gel films may accidentally be thinner on the electrode surfaces that are more difficult for the precursors to reach, where the thickness may fall into the desirable Al₂O₃ layer thickness range.)

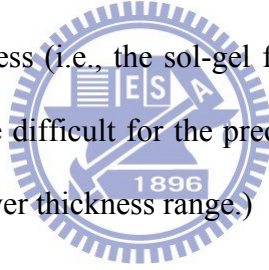


Table 4-3 Cell performance of the DSSCs containing the ALD Al₂O₃ overlayers with different thickness.

Al ₂ O ₃ Thickness (nm)	V_{oc} (mV)	J_{sc} (mA/cm ²)	FF (%)	PCE (%)
0	737±9	11.57±0.43	66.9±0.7	5.75±0.22
0.2 (1-cycle)	765±9	12.46±0.38	68.7±0.8	6.50±0.15
0.5 (2-cycles)	744±38	9.77±0.21	68.6±5.8	5.00±0.16
1.0 (5-cycles)	796±4	0.86±0.11	67.9±8.8	0.46±0.12
1.9 (10-cycles)	764±104	0.18±0.01	37.2±3.4	0.05±0.01

To discuss the effects of Al₂O₃ overlayers on the power conversion efficiency (PCE) of DSSCs, a schematic band diagram is presented in Fig. 4.5 with three interfacial energy parameters i.e., the difference of WF between Al₂O₃ and TiO₂ overlayer ($\Delta\Phi_{A-T}$), charge

recombination barrier height (ϵ_{RB}), and the interfacial energy barrier height between N719 dye and Al_2O_3 ($^*\epsilon_{IB}$). The conduction band minimum (CBM) relative to the Fermi-level was calculated from the aforementioned VBM and band gap data as: $\text{CBM} = \text{Band gap} - \text{VBM}$. It is reasonable to correlate these three parameters with PCE based on the concept of electron transportation, which suggests positive values of $\Delta\Phi_{A-T}$, high ϵ_{RB} values, and low $^*\epsilon_{IB}$ values, resulting in higher PCE for DSSCs. By assuming that the Lowest Unoccupied Molecular Orbital (LUMO) of N719 in the DSSCs was 0.4 eV higher than the conduction band minimum (CBM) of TiO_2 [93], the interfacial energy barriers between N719 dye and the Al_2O_3 layer ($^*\epsilon_{IB}$) can be calculated quantitatively to evaluate its effects on PCE.

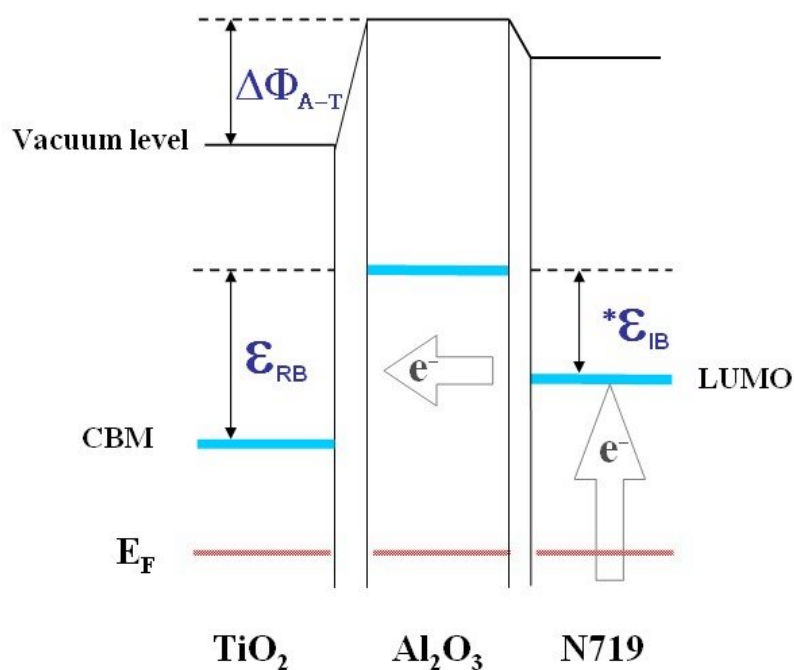


Figure 4.5 Schematic band diagram with three interfacial energy parameters: the difference of WF between Al_2O_3 and TiO_2 overlayer ($\Delta\Phi_{A-T}$), the charge recombination barrier height (ϵ_{RB}) and the interfacial energy barrier height between N719 dye and Al_2O_3 (ϵ_{IB}).

As a result, Fig. 4.6 shows the relationship between the energy levels' differences ($\Delta\Phi_{A-T}$, ϵ_{RB} , $*\epsilon_{IB}$) and PCE with various thicknesses of Al_2O_3 layers. The efficiency was increased initially by 13% at ~ 0.2 -nm thickness of Al_2O_3 layer, and then it dropped dramatically to almost zero percent after the thickness of the Al_2O_3 layers increased. The tunneling effect [94] which will exponentially decrease the current from dye to TiO_2 electrode with the thickness of Al_2O_3 overlayers increased was found from the open-circuit voltage (V_{oc}), short-circuit current (J_{sc}), and fill factor (FF) listed in table 4-3. Accordingly, the drop of the PCE maybe ascribed to tunneling effect when the thickness of Al_2O_3 overlayers increased and the initial increase of PCE and J_{sc} at ~ 0.2 -nm thickness of Al_2O_3 layer maybe attributed in part to the reduction of recombination. On the other hand, the increase of V_{oc} might exist few possible reasons: One possible reason is that the Al_2O_3 overlayer provides a negative conduction band by the lower electron affinity [55]; however, the electron affinity of Al_2O_3 overlayer at ~ 0.2 -nm thickness is higher than TiO_2 electrode in the present study (see table 4-2); therefore, this reason can be excluded. Another ideal reason is more likely that the positive work function difference ($\Delta\Phi_{A-T}$) provided a built-in potential (eV_{bi}) at the semiconductors' heterojunction [95] to increase the V_{oc} of the DSSC. Therefore, the positive $\Delta\Phi_{A-T}$ (~ 0.4 eV) value of Al_2O_3 overlayer may be regarded as a important factor to increase the PCE of the DSSCs.

It can be seen that the $\Delta\Phi_{A-T}$ of 0.4 eV and ϵ_{RB} of 0.1 eV, which were associated with 0 eV $*\epsilon_{IB}$, should be the key factors for the PCE increase after the first monolayer or ~ 0.2 nm of ALD Al_2O_3 layer deposition. The significant reduction of PCE was accompanied by decreasing values of $\Delta\Phi_{A-T}$ and increasing values of $*\epsilon_{IB}$ at the following deposition of 2-cycle ALD Al_2O_3 layers. This is consistent with the concept of semiconductor physics, that there will be no difficulty for electron transfer to the Al_2O_3 layers, especially if $*\epsilon_{IB}$ remains at 0 eV. The evidence suggests that the change in efficiency of the DSSCs that resulted from the

various thicknesses of the Al₂O₃ overlayers can be correlated with the difference of work function ($\Delta\Phi_{A-T}$), recombination barrier height (ϵ_{RB}), and interfacial energy barrier height ($*\epsilon_{IB}$).

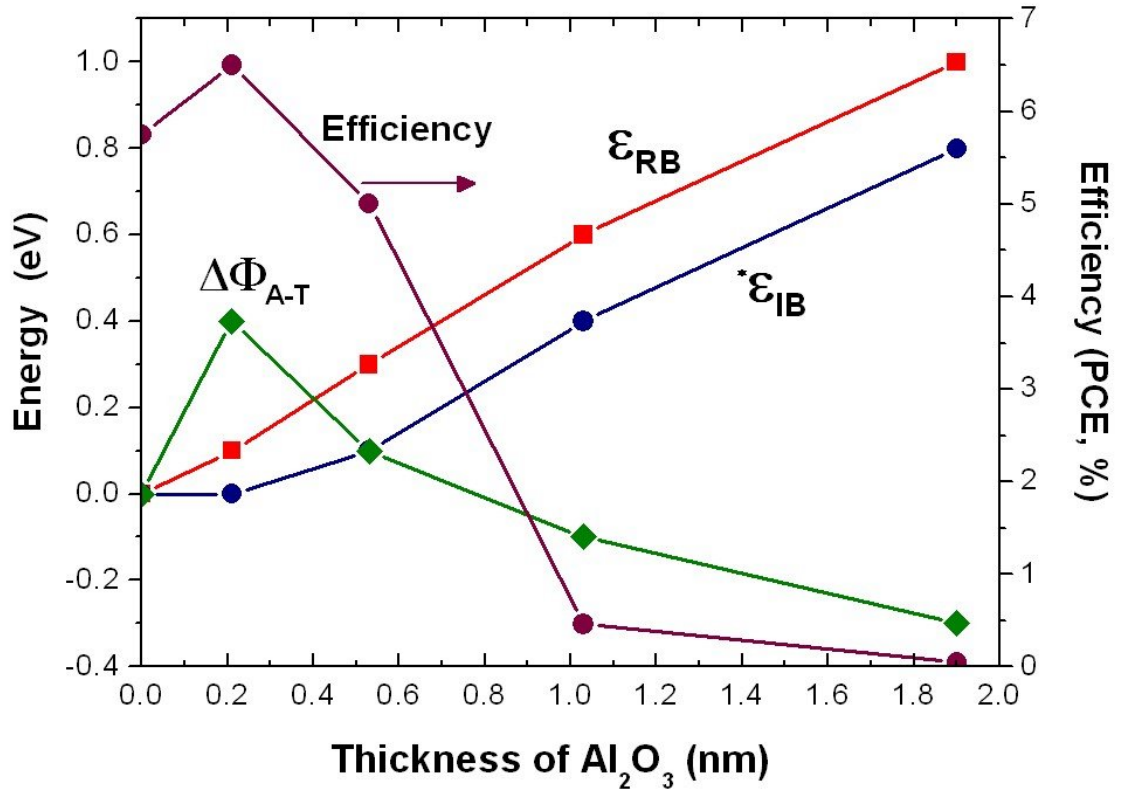


Figure 4.6 Interfacial energy levels difference ($\Delta\Phi_{A-T}$, ϵ_{RB} , $*\epsilon_{IB}$) and PCE via the thickness of Al₂O₃ layers.

It should be noted that the linear and parallel increases of ϵ_{RB} and $*\epsilon_{IB}$ with the layer thickness is not related to a similar increase in $\Delta\Phi_{A-T}$. This can be attributed to the changes of the band gap by ultra-thin Al₂O₃ structure and the changes of the work function by the dipole layers and Ti-O-Al(OH)₂, as the aforementioned description of Fig 4.3, 4.4 and 4.5. The ϵ_{RB} (~0.1 eV) of the thinnest Al₂O₃ layer may increase the electron concentration in the TiO₂ electrode by reducing the electron transported across the Al₂O₃ layer. The surface passivation

effect could be induced by the increase of the electron concentration in the TiO₂ electrode, thus enhancing both the photovoltage and photocurrent of the DSSC [96].

The results suggest two mechanisms correlated with the paths of electron transfer which is illustrated in Fig. 4.7. The first mechanism revealed that electron injects from dye into TiO₂ without any energy barrier and therefore improve the cells PCE due to the proper ultra-thin Al₂O₃ energy levels in Fig. 4.7(a). The second paths of electron transfer suggested that electron injects from dye into TiO₂ by tunneling effect in Fig. 4.7(b) when the Al₂O₃ structure is thicker and therefore decreases the cells PCE.

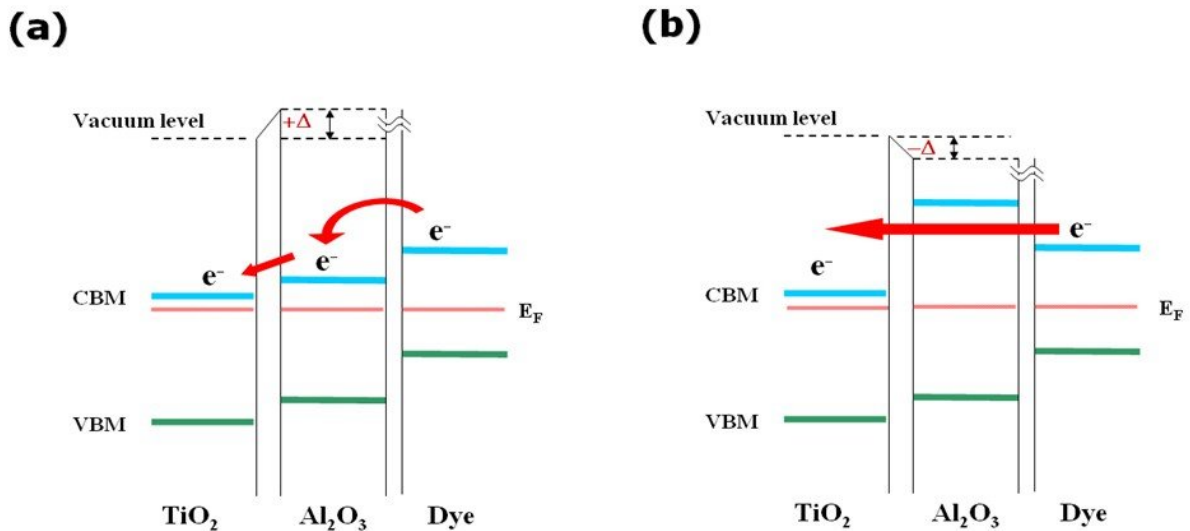


Figure 4.7 Schematic band diagrams illustrate that the paths of electron transfer from dye into TiO₂ (a) without any energy barrier and therefore improve the cells PCE due to the ultra-thin Al₂O₃ energy levels, and (b) by tunneling effect when the Al₂O₃ layer is thicker.

The dependence of the interfacial energy levels on the thickness of the Al₂O₃ overlayers may explain the fluctuation of the PCE in the dye-sensitized TiO₂ solar cells. It also has implications for the design and optimization of the DSSCs, especially those based on nanoporous TiO₂ electrodes. Regarding thickness control, it is necessary to understand the

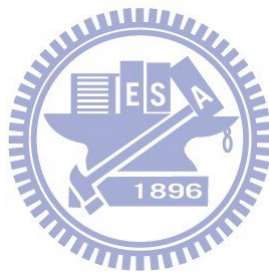
mechanism of growth of the ALD Al₂O₃ overlayers on the TiO₂ electrodes. The mechanism may be related to the island growth modes resulting in a low coverage of ALD Al₂O₃ overlayer on nanoporous TiO₂ electrode [82]; therefore, in this study, the ALD may not have so much advantage than sol-gel techniques due in part to the low coverage of ALD Al₂O₃ overlayers on nanoporous TiO₂ electrodes was not optimized at present stage. However, since the coverage of ALD Al₂O₃ overlayers on nanoporous TiO₂ electrodes is not known, further experiments are in progress to clarify this issue.

4.4 Summary

A low-temperature (150 °C) ALD process was used to obtain ultra-thin Al₂O₃ over-layers on a TiO₂ electrode in dye-sensitized solar cells. The optimal Al₂O₃ thickness was determined to be about 0.2 nm, and this thickness resulted in an enhancement of the power conversion efficiency (PCE) by ~13%, which is a significant increase over the DSSCs without Al₂O₃ overlayer. Thicker Al₂O₃ overlayers moved the valence band maximum and band gap toward those of pure Al₂O₃. The core level XPS peaks showed the formation of Ti-O-Al(OH)₂ and dipole layers at the Al₂O₃/TiO₂ interface and exhibited a strong influence on the work function of the Al₂O₃ overlayers. A work function difference ($\Delta\Phi_{A-T}$) of 0.4 eV and a recombination barrier height (ϵ_{RB}) of 0.1 eV were associated with the highest PCE after the deposition of the first ALD Al₂O₃ monolayer. A significant reduction of PCE occurred as $\Delta\Phi_{A-T}$ decreased and ϵ_{IB} increased.

The results show that the paths of electron transfer from dye into TiO₂ without any energy barrier and therefore improve the cells PCE due to the proper ultra-thin Al₂O₃ energy levels. The evidence suggests that the power conversion efficiency (PCE) of the DSSCs can

be correlated with the difference of work function ($\Delta\Phi_{A-T}$), recombination barrier height (ϵ_{RB}), and the interfacial energy barrier height (ϵ_{IB}) of the Al_2O_3 overlayers. Interfacial reactions, such as the formation of $Ti-O-Al(OH)_2$ and dipole layers, play an important role in determining the interfacial energy levels and the PCE, which must be taken into account in designing an optimal performance of dye-sensitized TiO_2 solar cells.



Chapter 5

Coverage Analysis for the Core/Shell Electrode of Dye-Sensitized Solar Cells

Correct determination of the coverage of an ultra-thin Al_2O_3 layer coated on a porous electrode is difficult because there is presently no reliable analytical tool for the measurement. For instance, information provided by TEM analysis with an atomic scale resolution is limited to a localized area, and sample damage may occur during TEM sample preparations. X-ray photoelectron spectroscopy (XPS) has a very small probe depth (<10 nm) and is often used to determine the coverage of an ultra-thin film on a flat substrate in terms of measuring XPS signals of the substrate as a function of the amount of deposited film materials. However, XPS becomes less straightforward when the coverage on a curved substrate, such as a particle, is studied. Theoretical models based on XPS to evaluate the coverage of an ultra-thin layer on a particle usually require an elaborate mathematical derivation with complex geometric considerations. This is particularly so for ultra-thin films deposited on porous substrate composed of interconnected nanoparticles. The purpose of this study is to develop a multi-layers-core/shell model, using XPS, to measure the coverage of shell layers on the nanoporous electrodes of DSSCs. The model resembles more to a real core/shell material system as in the case of the porous TiO_2 electrode. Using these characterization techniques, we studied the influence of the coverage of the Al_2O_3 shell layers on the PCE of our DSSCs.

5.1 Theoretical Model from the Signals of X-ray

Photoelectrons

We found that the PCE enhancement for our DSSCs featuring the ALD- Al_2O_3 shell layers is not better than that for DSSCs with Al_2O_3 shell layers prepared by other methods, such as sol-gel coating. We ascribed to the unsatisfactory PEC enhancement to a low coverage of the ALD- Al_2O_3 shell layers on the nanoporous TiO_2 electrodes as a result of that the island growth mode prevails during the ALD deposition. To further optimize the PCEs of DSSCs featuring $\text{Al}_2\text{O}_3/\text{TiO}_2$ electrodes, it will be necessary to know well the dependence of the coverage of the Al_2O_3 over-layers on the number of the ALD deposition cycles. However, to correctly determine the coverage of an ultrathin Al_2O_3 layer coated on a porous electrode is difficult because there is presently no reliable analytical tool for the measurement. For instance, information provided by TEM analysis with an atomic scale resolution is limited to a localized area, and sample damage may occur during TEM sample preparations.

X-ray photoelectron spectroscopy (XPS) has a very small probe depth (<10 nm) and is often used to determine the coverage of an ultrathin film on a flat substrate in terms of measuring XPS signals of the substrate as a function of the amount of deposited film materials. However, XPS becomes less straightforward when the coverage on a curved substrate, such as a particle, is studied. Theoretical models based on XPS to evaluate the coverage of an ultrathin layer on a particle usually require an elaborate mathematical derivation with complex geometric considerations. This is particularly so for ultrathin films deposited on porous substrates composed of interconnected nanoparticles. The purpose of this study is to develop a multi-layers-C/S model, using XPS, to measure the coverage of shell layers on the nanoporous electrodes of DSSCs. The model treats only the zenith angle in the mathematic derivation in terms of spherical symmetry considerations, therefore the derivation is simpler compared with other models.

5.1.1 The Model for A Isolated Core/Shell Particle

Like several previous reported models [97~ 100] which relate the adsorbate coverage on a spherical particle to the XPS signal emitted from the particle, the basic concept of our core/shell model divides the nanoparticle, which is assumed to be spherical, into many small partitions, and considers separately the XPS signal emitted from each partition. In this model, numerous identical circular planes can be constructed from a sphere as shown in Fig. 5.1, in which the projections of three such circular planes at different azimuth angles (ϕ) are illustrated. The symmetrical geometry of the spherical particle allows us to exclude the participation of the ϕ angle in the derivation of the relation of the shell coverage with the XPS signal emitted from the core, thus only a circular plane at a fixed ϕ angle is taken into account to derive the relation. The circular plane is divided into 1000 strips with the long axis perpendicular to the sample surface. As shown in Fig. 5.1, the thickness of the shell (t_x) in a strip, e.g., strip x, depends on the strip angle (α_x) between the strip passing through the origin of the circle (O) and the line connecting point O with the intersecting point of strip x and the circle. Each strip is so thin that we may consider, within the strip, the surface of the core particle is flat. Because the hemispherical energy analyzer is located from the sample at a distance much larger than the sample size, we assume that electrons emitted from all the strips have the same emission angle, which is zero degree under the present analysis configuration.

In a previous study [53], we found that ALD- Al_2O_3 deposition on the porous TiO_2 electrode followed the island growth (Volmer-Weber) mode according to a plot of the growth per cycle vs the number of ALD reaction cycles. Based on Sitar's study [101], the dependence

of XPS signals of a flat substrate on the island coverage (θ_{island}) can be expressed as the following equation:

$$I_s/I_0 = (1 - \theta_{island}) + \theta_{island} \times e^{-na/\lambda} \quad (5-1)$$

where I_s and I_0 are the intensities of photoelectrons emitted from the substrate with and without the thin film material, respectively, n is the number of monolayers in an island, a is the thickness of each monolayer, and λ is the inelastic mean free path (IMFP) of electrons traveling in the overlayer. Assuming a uniform coverage, we replace θ_{island} with the coverage of the shell material (fractional coverage, θ) on the two ends of each strip, and introducing the strip angle (α_x) for the thickness calculation, and thus equation (5-1) can be converted into the following expression:

$$\Delta I/\Delta I_\alpha = (1 - \theta) + \theta \times e^{-t/(\lambda_{shell} \times \cos\alpha)} \quad (5-2)$$

where ΔI and ΔI_α are the intensities of photoelectrons emitted from a single strip with and without the shell layer, respectively, t is the thickness of the shell layer, α is the strip angle (from theta values 0 to 90°), and λ_{shell} is the inelastic mean free path (IMFP) of electrons traveling in the shell layer. We assume in this model that θ is the same for all the 1000 strips because of the homogenous deposition nature of ALD. By summing up the values of ΔI of all strips in terms of α (from $\theta = 0^\circ$ to 90°), we obtained an equation representing the total intensity (I) of photoelectrons emitted from the entire half part of the circular plane with the shell layer as follows:

$$I = \sum_{\alpha=0^{\circ}}^{90^{\circ}} \Delta I = \sum_{\alpha=0^{\circ}}^{90^{\circ}} \{ \Delta I_{\alpha} \times [(1 - \theta) + \theta e^{-t / (\lambda_{\text{shell}} \times \cos \alpha)}] \} \quad (5-3)$$

The value of ΔI_{α} can be calculated using the following equation [100]

$$\Delta I_{\alpha} = \Delta I_{\text{bulk}} \times [1 - e^{(-2r \cos \alpha / \lambda_{\text{core}})}] \quad (5-4)$$

where ΔI_{bulk} represents the intensity of the photoelectrons from a strip of infinite length (relative to λ_{core}), r is the radius of the circular plane, and λ_{core} is the IMFP of electrons traveling in the core particle. In this study, the radius of the core particle is around 10 nm.

Substituting equation (5-4) into equation (5-3), we obtain

$$I = \sum_{\alpha=0^{\circ}}^{90^{\circ}} \{ \Delta I_{\text{bulk}} \times [1 - e^{(-2r \cos \alpha / \lambda_{\text{core}})}] \times [(1 - \theta) + \theta e^{-t / (\lambda_{\text{shell}} \times \cos \alpha)}] \} \quad (5-5)$$

At the boundary conditions ($t = 0$; $\theta = 0$),

$$I = I_0 = \sum_{\alpha=0^{\circ}}^{90^{\circ}} \{ \Delta I_{\text{bulk}} \times [1 - e^{(-2r \cos \alpha / \lambda_{\text{core}})}] \} \quad (5-6)$$

where I_0 is the intensity of photoelectrons from half part of circular plane without the shell layers. Since ΔI_{bulk} is independent of angle α , equation (5-6) can be rewritten and converted into as:

$$\Delta I_{\text{bulk}} = I_0 \div \sum_{\alpha=0^\circ}^{90^\circ} [1 - e^{(-2r\cos\alpha/\lambda_{\text{core}})}] \quad (5-7)$$

Substituting equation (5-7) into equation (5-5), we obtain

$$\frac{I}{I_0} = \frac{\sum_{\alpha=0^\circ}^{90^\circ} \{ [1 - e^{(-2r\cos\alpha/\lambda_{\text{core}})}] \times [(1 - \theta) + \theta e^{-t/(\lambda_{\text{shell}} \times \cos\alpha)}] \}}{\sum_{\alpha=0^\circ}^{90^\circ} [1 - e^{(-2r\cos\alpha/\lambda_{\text{core}})}]} \quad (5-8)$$

The values of λ_{core} and λ_{shell} (nm) can be calculated using equations (5-9) and (5-10) [102]:

$$\lambda = 2170aE^{-2} + 0.72a^{3/2}E^{1/2} \quad (5-9)$$

$$a = \left(\frac{10^{27} M_W}{\rho n_A N_a} \right)^{1/3} \quad (5-10)$$

where E is the kinetic energy (eV) of the detected electron, M_W is the molecular weight of the core or shell material, ρ is the density, n_A is the number of the atoms in a molecule, and N_a is Avogadro's number.

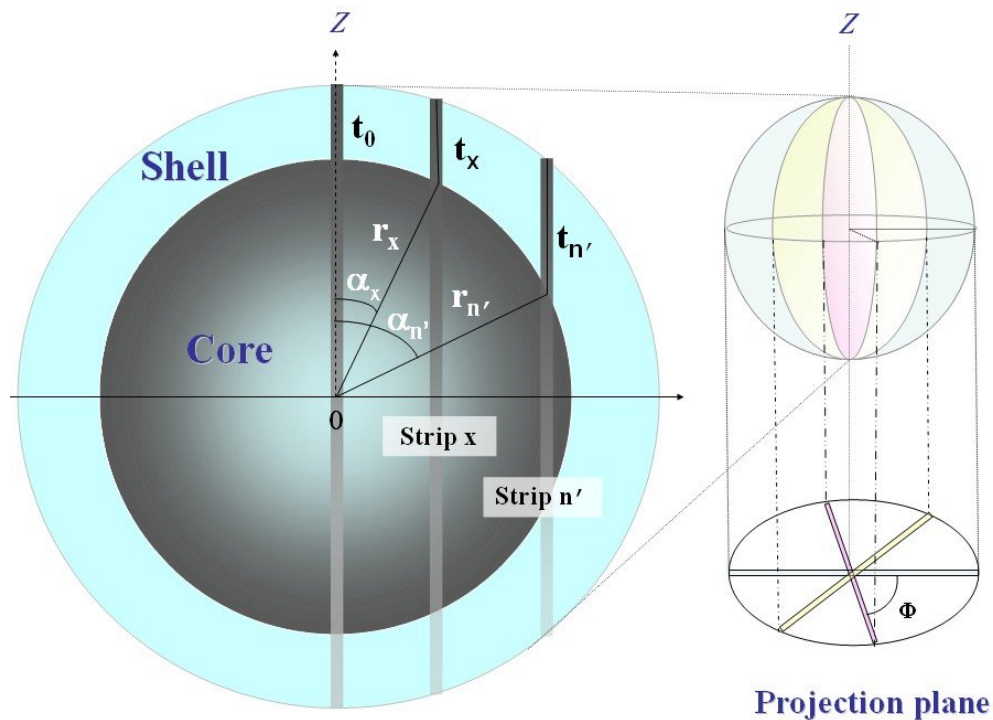


Figure 5.1 C/S model for calculating the fractional coverage (θ) of shell layers from an isolated C/S particle. The left circular plane is the cross-sectional plane which produces a projection line at a certain azimuth angle.

Although the I/I_0 ratio of Eq. 5-8 is derived for a single circular plane, it also equals to the XPS signal ratio of an entire core particle without and with the shell layer if homogeneous coverage is assumed, which is likely applicable to ALD deposition. This is because the model symmetrically divides a core particle into numerous identical circular planes.

5.1.2 The Model for Core/Shell Particles in Multi-Layers

Equation 5-8 is only good for the evaluation of the I/I_0 ratio for one C/S particle or samples with one-monolayer of C/S particles. To study the relation of the I/I_0 ratio with the fractional coverage, θ , for a multilayer sample, such as the porous DSSC electrode composed

of interconnected TiO₂/Al₂O₃ core shell nanoparticles, further modification for Eq. 5-8 is required. As shown in Fig. 5.2, photoelectrons emitted from C/S particles below the first monolayer can still escape from the sample surface if open space is available or the upper layer is thinner than the escape depth of photoelectrons. The total XPS signal intensity of the C/S structured thin film with (I^{total}) and without (I_0^{total}) the shell layer can be expressed by the following equations:

$$I_0^{\text{total}} = I_0^{\text{1st}} + I_0^{\text{2nd}} + I_0^{\text{3rd}} + I_0^{\text{4th}} + \dots + I_0^{\text{nth}} \quad (5-11)$$

$$I^{\text{total}} = I^{\text{1st}} + I^{\text{2nd}} + I^{\text{3rd}} + I^{\text{4th}} + \dots + I^{\text{nth}} \quad (5-12)$$

where I_0^{nth} and I^{nth} are the signal intensities of the nth layer before and after the shell coating, respectively (last n= total thickness of layers/2r, where r is the radius of the particle).

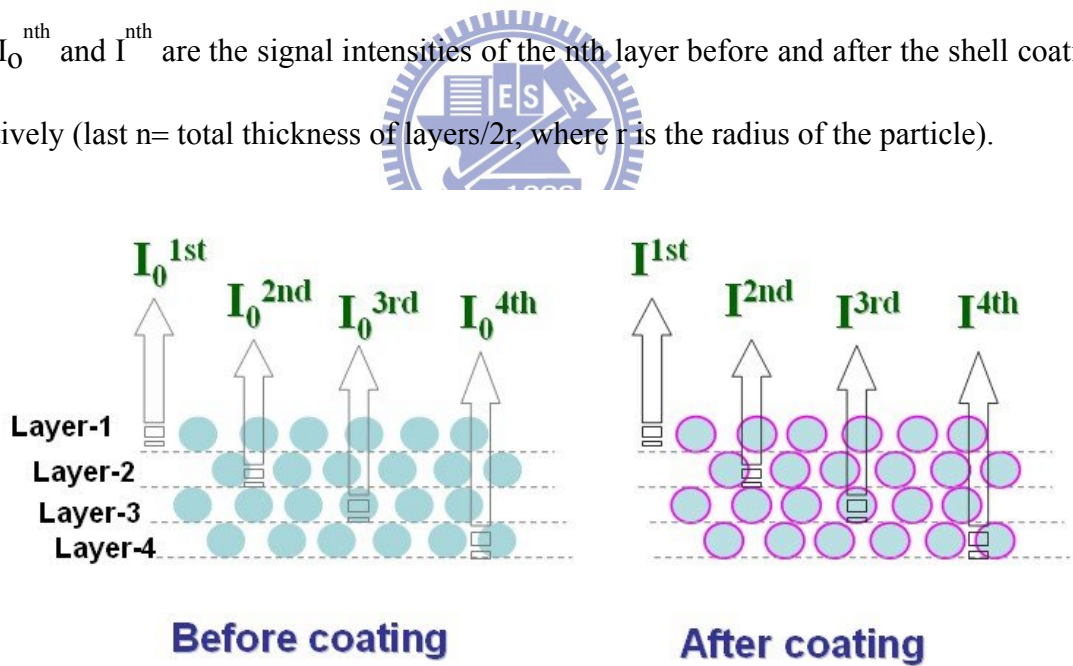


Figure 5.2 The multi-layers-C/S model for calculating the coverage of shell layers from each layer.

According to Fig. 5.2, all layers are regarded to have the same composition and thickness. Therefore, the original signal of electrons emitted from core particles of layer-2 presumably equals to that from layer-1 (denoted as I^{1st}). Due to the symmetrical geometry of the assumed spherical nanoparticle, only one half of the circular plane in layer-1 is considered for the derivation as illustrated in Fig. 5.3. The circular plane is constructed from a sphere as illustrated in Fig. 5.1. Because of the porosity nature of the porous film, electrons emitted from layer-2 can escape from the sample either by penetrating through the upper core particles and the shell-only region in layer-1 or by emitting into the open space.

To calculate the I^{2nd} , we assume the original signal intensities of layer-2 (I^{1st}) distributed uniformly over the volume of layer-2. Then, the region A in layer-2, which is located right below the half part of a circular plane in layer-1, has an intensity of aI^{1st} , where a is a fractional constant and is closely related to the size of the region. The region was divided into 1000 strips using the same method as that of Fig. 4.1; then, each strip can emit $\Delta I_{\alpha,a}$ as shown in Fig. 5.3. After penetrating through the upper nanoparticle vertically, the signal $\Delta I_{\alpha,a}$ decreases to a signal denoted as $\Delta(aI^{2nd})$ with the following expression:

$$\Delta(aI^{2nd}) = \Delta I_{\alpha,a} \times [(1-\theta) + \theta e^{-t/(\lambda_{Shell} \times \cos\alpha)}]^2 \times e^{(-2r\cos\alpha/\lambda_{Core})} \quad (5-13)$$

The signal $\Delta I_{\alpha,a}$, is proportional to the width ($W_{\alpha,a}$) of a strip, can be calculated using equation (S4):

$$\begin{aligned} \Delta I_{\alpha,a} &= aI^{1st} \times W_{\alpha,a}/r = aI^{1st} \times [r \times \sin(\alpha + \pi/2000) - r \times \sin\alpha]/r \\ &= aI^{1st} \times [\sin(\alpha + \pi/2000) - \sin\alpha] \end{aligned} \quad (5-14)$$

where α from 0 to $\pi/2$. Then the total signal aI^{1st} from layer-2 decreases to aI^{2nd} after penetrating vertically through layer-1.

$$\begin{aligned}
 aI^{2nd} &= \sum_{\alpha=0}^{\pi/2} \Delta(aI^{2nd}) \\
 &= aI^{1st} \times \sum_{\alpha=0}^{\pi/2} \left\{ [\sin(\alpha + \pi/2000) - \sin\alpha] \times [(1-\theta) + \theta e^{-t/(\lambda_{\text{Shell}} \times \cos\alpha)}]^2 \times e^{(-2r\cos\alpha/\lambda_{\text{Core}})} \right\} \\
 &= aI^{1st} \times \text{Sub-layer Factor-1 (SF-1)} \tag{5-15}
 \end{aligned}$$

$$I^{2nd} = I^{1st} \times \text{Sub-layer Factor-1 (SF-1)} \tag{5-16}$$

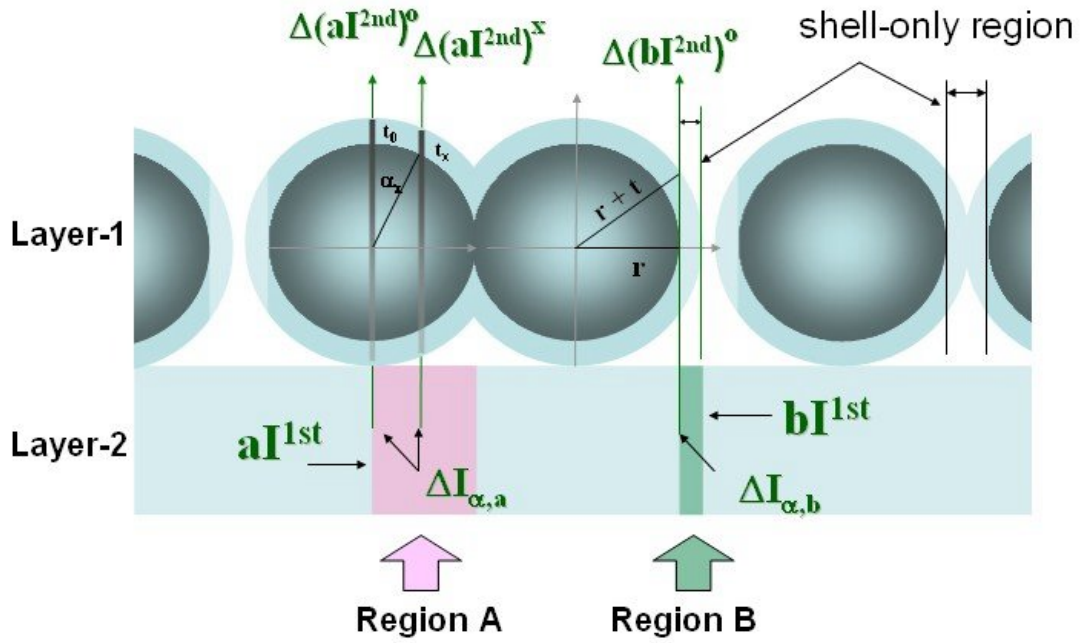


Figure 5.3 The illustration reveals the signals of layer-2 penetrating the upper core/shell particles.

Likewise, we can define the signal emerging out of the region B where only the shell layer block the passage of electrons emitted from layer-2 as bI^{1st} , where b is the fractional constant for the shell-only region, which is also divided into 1000 strips and each strip can

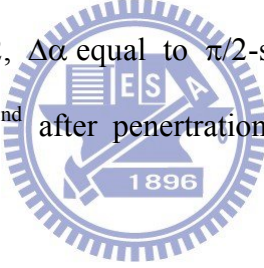
emit $\Delta I_{\alpha,b}$. The signals $\Delta I_{\alpha,b}$ decreases to $\Delta(bI^{2nd})$ and the signals bI^{1st} decreases to bI^{2nd} . Then, we obtain

$$\Delta(bI^{2nd}) = \Delta I_{\alpha,b} \times [(1-\theta) + \theta e^{-2\cos\alpha(r+t)/\lambda_{Shell}}] \quad (5-17)$$

The signal $\Delta I_{\alpha,b}$, is proportional to the width ($W_{\alpha,b}$) of a strip, can be calculated using equation (5-18):

$$\begin{aligned} \Delta I_{\alpha,b} &= bI^{1st} \times W_{\alpha,b}/t = bI^{1st} \times [(r+t) \times \sin(\alpha + \Delta\alpha/1000) - (r+t) \times \sin\alpha]/t \\ &= bI^{1st} \times [\sin(\alpha + \Delta\alpha/1000) - \sin\alpha] \times (r+t)/t \end{aligned} \quad (5-18)$$

where α from $\sin^{-1}[r/(r+t)]$ to $\pi/2$, $\Delta\alpha$ equal to $\pi/2 - \sin^{-1}[r/(r+t)]$. Then the total signal bI^{1st} from layer-2 decreases to bI^{2nd} after penetration.



$$\begin{aligned} bI^{2nd} &= \sum_{\alpha=\sin^{-1}[r/(r+t)]}^{\pi/2} \Delta(bI^{2nd}) \\ &= bI^{1st} \times \sum_{\alpha=\sin^{-1}[r/(r+t)]}^{\pi/2} \left\{ [\sin(\alpha + \Delta\alpha/1000) - \sin\alpha] \times [(1-\theta) + \theta e^{-2\cos\alpha(r+t)/\lambda_{Shell}}] \times (r+t)/t \right\} \\ &= bI^{1st} \times \text{Sub-layer Factor-2 (SF-2)} \end{aligned} \quad (5-19)$$

$$I^{2nd} = I^{1st} \times \text{Sub-layer Factor-2 (SF-2)} \quad (5-20)$$

It should be noted that the equation (5-16) and (5-20) are only applicable when signals emitted from layer-2 penetrate through upper core particles and through shell-only regions, respectively. To calculate the total signal emitted from layer-2 (I^{2nd}), we should also take the signal emerging from those areas without being blocked by nanoparticles of layer-1 into

account. Thus we include the term accounting for the signal emitted into the open space in the expression for I^{2nd} as follows:

$$\begin{aligned}
 I^{2nd} &= (1-A_{A, \text{core}} - A_{A, \text{shell}}) \times I^{1st} + A_{A, \text{core}} \times I^{1st} \times \text{SF-1} + A_{A, \text{shell}} \times I^{1st} \times \text{SF-2} \\
 &= I^{1st} \times (1-A_{A, \text{core}} - A_{A, \text{shell}} + A_{A, \text{core}} \times \text{SF-1} + A_{A, \text{shell}} \times \text{SF-2}) \quad (5-21)
 \end{aligned}$$

where $A_{A, \text{core}}$ is the projection area of the core particles in a layer, $A_{A, \text{shell}}$ is the projection area of the a shell-only-regions in a layer, and can be acquired from equation (5-22) and (5-23) [103]:

$$A_{A, \text{core}} = 1 - \exp\left[-\frac{V_{V, \text{core}}}{2} \times \frac{(D + 3t')}{D}\right] \quad (5-22)$$

$$A_{A, \text{shell}} = 1 - \exp\left[-\frac{V_{V, \text{shell}}}{2} \times \frac{(D' + 3t')}{D'}\right] - \left\{ 1 - \exp\left[-\frac{V_{V, \text{core}}}{2} \times \frac{(D + 3t')}{D}\right] \right\} \quad (5-23)$$

where $V_{V, \text{core}}$ is the volume fraction of the core particles in layer-2 and it is equal to $1-P$ for the C/S sample with a porosity P before coating, D is the diameter of the bare core particles, t' is the thickness of layer-2 ($t' = 2r$ by assumption), $V_{V, \text{shell}}$ is the volume fraction of the shell-only regions in layer-2 and it is equal to $1-P'$ for the C/S sample with a porosity P' after coating, D' is the diameter of the particles after coating. By defining the terms in the parenthesis in Eq. 5-21 as the Multi-layers Factor (M), we obtain the following expression for I^{2nd} :

$$I^{2nd} = I^{1st} \times M \quad (5-24)$$

As a result, using the same concepts and procedures as discussed from equations (5-17) to (5-23), we obtain I^{3rd} , I^{4th} ,, I^{nth} as follows:

$$\begin{aligned}
I^{3rd} &= [(1-A_{A, \text{core}} - A_{A, \text{shell}}) \times I^{1st} + A_{A, \text{core}} \times I^{1st} \times \text{SF-1} + A_{A, \text{shell}} \times I^{1st} \times \text{SF-2}] \\
&\quad \times (1-A_{A, \text{core}} - A_{A, \text{shell}} + A_{A, \text{core}} \times \text{SF-1} + A_{A, \text{shell}} \times \text{SF-2}) \\
&= I^{1st} \times (1-A_{A, \text{core}} - A_{A, \text{shell}} + A_{A, \text{core}} \times \text{SF-1} + A_{A, \text{shell}} \times \text{SF-2})^2 \\
&= I^{1st} \times M^2
\end{aligned} \tag{5-25}$$

$$\begin{aligned}
I^{nth} &= I^{1st} \times (1-A_{A, \text{core}} - A_{A, \text{shell}} + A_{A, \text{core}} \times \text{SF-1} + A_{A, \text{shell}} \times \text{SF-2})^{n-1} \\
&= I^{1st} \times M^{n-1}
\end{aligned} \tag{5-26}$$

The same concepts and procedures can be implemented to the calculation of I_o^{2nd} , I_o^{3rd} , I_o^{4th} , ..., I_o^{nth} as:

$$\begin{aligned}
I_o^{2nd} &= (1-A_{A, \text{core}}) \times I_o^{1st} + A_{A, \text{core}} \times I_o^{1st} \times \text{SF-1}(t=0) \\
&= I_o^{1st} \times [1-A_{A, \text{core}} + A_{A, \text{core}} \times \text{SF-1}(t=0)] \\
&= I_o^{1st} \times M(0)
\end{aligned} \tag{5-27}$$

$$\begin{aligned}
I_o^{3rd} &= [(1-A_{A, \text{core}}) \times I_o^{1st} + A_{A, \text{core}} \times I_o^{1st} \times \text{SF-1}(t=0)] \times [1-A_{A, \text{core}} + A_{A, \text{core}} \times \text{SF-1}(t=0)] \\
&= I_o^{1st} \times [1-A_{A, \text{core}} + A_{A, \text{core}} \times \text{SF-1}(t=0)]^2 = I_o^{1st} \times M(0)^2
\end{aligned} \tag{5-28}$$

$$\begin{aligned}
I_o^{nth} &= I_o^{1st} \times [1-A_{A, \text{core}} + A_{A, \text{core}} \times \text{SF-1}(t=0)]^{n-1} \\
&= I_o^{1st} \times M(0)^{n-1}
\end{aligned} \tag{5-29}$$

Substituting equation (5-21) and equation (5-24~5-29) into equation (5-11) and (5-12), we obtain

$$\frac{I^{total}}{I_o^{total}} = \frac{I^{1st} + I^{1st} \times M + I^{1st} \times M^2 + I^{1st} \times M^3 \dots + I^{1st} \times M^{n-1}}{I_o^{1st} + I_o^{1st} \times M(0) + I_o^{1st} \times [M(0)]^2 + I_o^{1st} \times [M(0)]^3 \dots + I_o^{1st} \times [M(0)]^{n-1}}$$

$$\begin{aligned}
&= \frac{I^{1st} \times [1 + M + M^2 + M^3 \dots + M^{n-1}]}{I_o^{1st} \times \{1 + M(0) + [M(0)]^2 + [M(0)]^3 \dots + [M(0)]^{n-1}\}} \\
&= \frac{I}{I_o} \times \frac{1 + M + M^2 + M^3 \dots + M^{n-1}}{1 + M(0) + [M(0)]^2 + [M(0)]^3 \dots + [M(0)]^{n-1}} \quad (5-30)
\end{aligned}$$

Ideally, the ratio (I^{total}/I_o^{total}) in equation (4-30) should be the same ratio as that obtained experimentally; i.e., we can substitute I^{total} by the intensity of detected electrons from the core particles possessing shell layers and substitute I_o^{total} by the intensity of detected electrons from the core particles lacking shell layers. The fractional coverage of the C/S thin film with various shell thicknesses can thus be estimated by XPS or AES analysis.

Although equations derived above are based on the concept of the escape depth of photoelectrons, equations 5-8 and 5-30 are also applicable to Auger electrons, which have a similar inelastic scattering behavior in solids as photoelectrons. In this study, we use XPS to estimate the fractional coverage of ALD Al_2O_3 deposited on the porous electrode composed of interconnected TiO_2 nanoparticles in terms of equations 30, and study the dependence of the DSSC performance on the coverage of the Al_2O_3 shell layer.

5.2 Samples Description

The procedures of samples fabrication have been revealed at chapter 3. The high resolution TEM (HRTEM) image in Fig. 5.4(a) displays the nanocrystalline TiO_2 core particles prepared without the Al_2O_3 shell layer; Fig. 5.4(b)–(d) present HRTEM images of the crystalline TiO_2 particles prepared with Al_2O_3 shell layers using two to 10 cycles of ALD. All of the samples featured spherical-like, uniform, interconnected TiO_2 particles that were ca. 20

nm in size. Table 5-1 lists the thicknesses of the Al_2O_3 over-layers prepared using 1–30 ALD cycles, as determined by TEM. Each listed thickness is the average value of ten thickness measurements for the Al_2O_3 over-layer. The thickness values indicate a significant discrepancy in the deposition rates (nm/cycle) for the various reaction cycles. For a layer-by-layer growth process, a rate of deposition equivalent to one monolayer of the film per ALD cycle is ideal; i.e., ~ 0.18 nm/cycle for Al_2O_3 [104]. To better examine the distribution of the ALD- Al_2O_3 deposit on the anatase nanoparticles, Figs. 5.5 shows HRTEM images of the shell material deposited on a local area of the core particles before and after the first and the fifth deposition cycles. The HRTEM images clearly show that the distribution of the ALD Al_2O_3 deposit is not uniform on the core particles, indicating that the ALD deposition is via an island growth process.

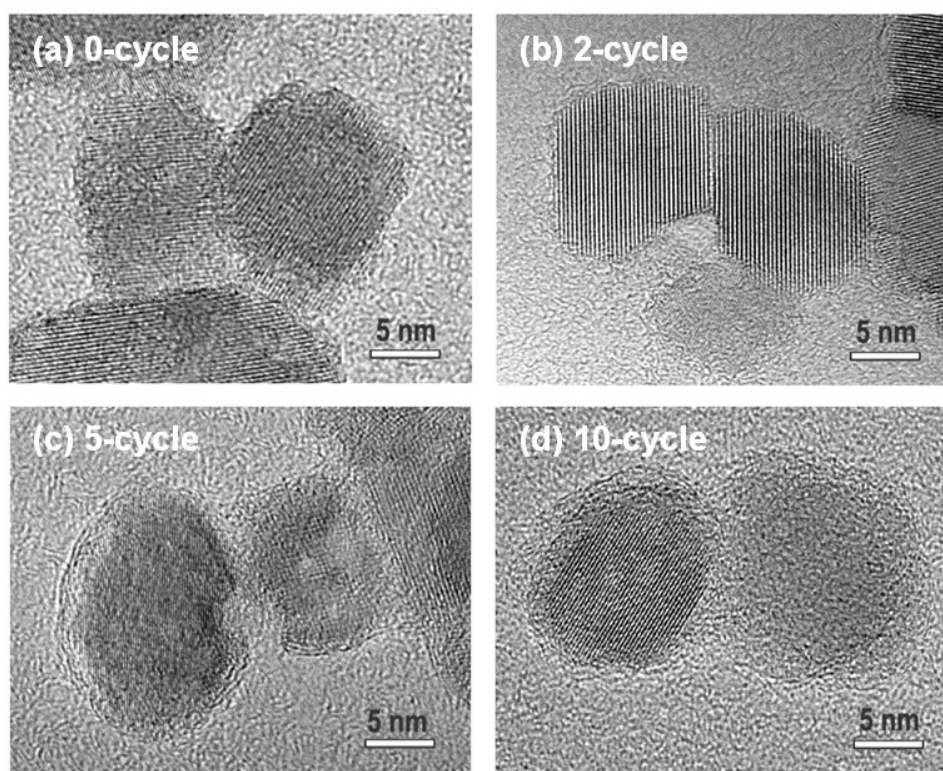


Figure 5.4 TEM images of nanocrystalline TiO_2 core particles prepared (a) without an Al_2O_3 shell layer, (b) with a two-cycle-ALD Al_2O_3 shell layer, (c) with a five-cycle-ALD Al_2O_3 shell layer, and (d) with a 10-cycle-ALD Al_2O_3 shell layer.

Table 5-1 Thickness and deposition rate of the ALD Al₂O₃ shell layers on TiO₂ electrodes.

Sample:	0-cycle	1-cycle	2-cycle	5-cycle	10-cycle	15-cycle	20-cycle	30-cycle
Al₂O₃ shell layers								
Thickness (nm)*	0	0.2±0.1	0.5±0.2	1±0.4	1.9±0.3	2.5±0.4	2.8±0.5	4.5±0.5
Deposition rate (nm/cycle)	–	0.2±0.1	0.25±0.1	0.2±0.08	0.19±0.03	0.17±0.02	0.14±0.02	0.15±0.02

* The thickness listed in the table is the average value of ten TEM measurements at different locations of the C/S nanoparticles.

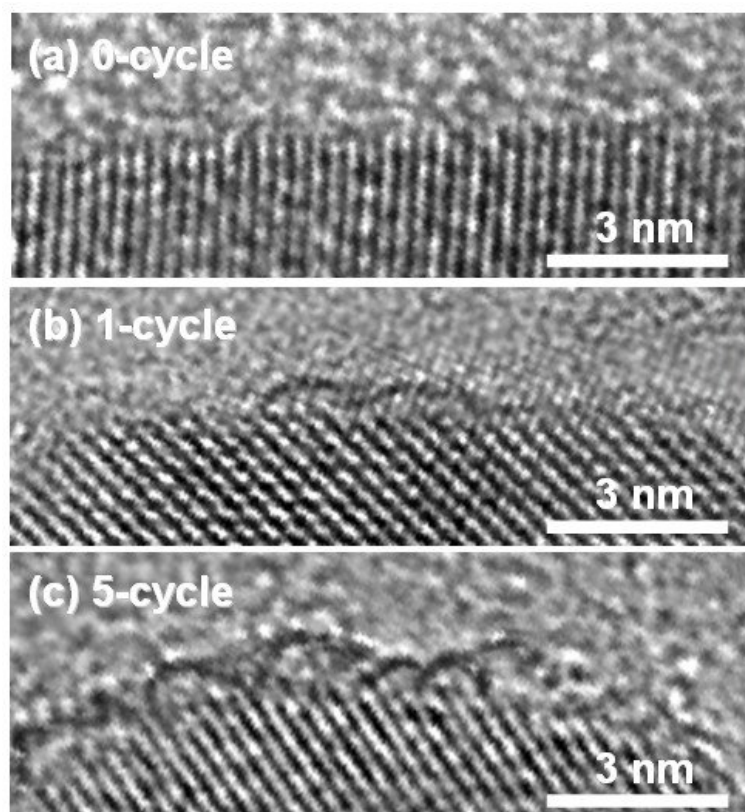


Figure 5.5 The enlarged TEM images show the TiO₂ core particles (a) without an Al₂O₃ shell layer, (b) with a one-cycle-ALD Al₂O₃ shell layer, (c) with a five-cycle-ALD Al₂O₃ shell layer.

5.3 Application of the Core/Shell Model on Nanoporous Electrode

Figure 5.6 shows the Ti 2p_{3/2} XPS spectrum of the as-received TiO₂ electrodes, indicating that the Ti 2p_{3/2} core level of the nanoporous TiO₂ electrodes was located at 458.9 eV, i.e., within the range from 458.8 to 459.4 eV reported for TiO₂ in the literature [84]. Following ALD of the first Al₂O₃ overlayer, the binding energy of the Ti 2p_{3/2} core level of the TiO₂ layers shifted by -0.5 eV to 458.4 eV; after 30 cycles, it shifted by +0.5 eV to 458.9 eV. These shifts in the Ti 2p_{3/2} core levels indicate that the Ti–O bond strength decreased within the 0.2-nm thick Al₂O₃ shell layer. The binding energy shift of the Ti 2p_{3/2} electron from -0.5 eV to +0.5 eV with increasing the thickness of the Al₂O₃ overlayers can be partly attributed to the change in the work function of the Al₂O₃-TiO₂ electrode. According to our previous study, the work function (WF) of the electrode increases from 4.7 eV to 5.1 eV after the first ALD cycle, followed by decreases with increasing the thickness of the Al₂O₃ overlayers (4.3 eV after 10 cycles of ALD) [53]. The magnitude and direction of the core level shifts observed in the XPS spectra are in good agreement with the change of WF with increasing the thickness of the Al₂O₃ overlayer.

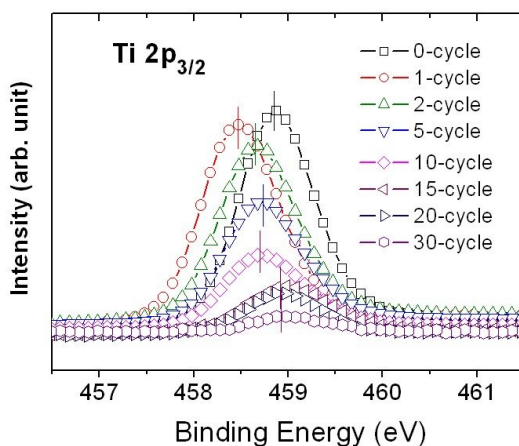


Figure 5.6 XPS spectra of the Ti 2p_{3/2} peaks from the nanoporous TiO₂ electrodes.

Figure 5.7 displays the $I_{\text{total}}/I_{\text{total}}^0$ ratio measured by XPS as a function of the thickness of the Al_2O_3 shell layer on the TiO_2 electrode. Each datum of the $I_{\text{total}}/I_{\text{total}}^0$ ratio is the average value of 5 measurements, with a deviation smaller than 3%. The solid curves are the theoretical curves, derived from the C/S model, for the $I_{\text{total}}/I_{\text{total}}^0$ ratio as a function of the shell thickness at various coverages (θ). When the number of ALD reaction cycles is smaller than 15, the measured $I_{\text{total}}/I_{\text{total}}^0$ ratio falls on the curves for $\theta < 1$, revealing the presence of bare TiO_2 surface areas. This is in agreement with the HRTEM images shown in Fig. 5.5, which show an uneven distribution of the ALD- Al_2O_3 deposits on the TiO_2 nanoparticles, and suggests that the deposition of the ALD Al_2O_3 film on TiO_2 nanoparticles is via the island growth mode. For an island film growth, growth and coalescence of deposited islands proceed during the ALD reaction, and a continuous island film will eventually develop. According to Fig. 5.7, the measured $I_{\text{total}}/I_{\text{total}}^0$ ratios for the shell layers deposited by more than 15 reaction cycles fall on the curve for $\theta = 1$, indicating that the nanoporous TiO_2 electrode was completely covered by the Al_2O_3 shell layer, i.e. a continuous Al_2O_3 film is formed.

Because XPS is very surface sensitive with the probe depth smaller than 10 nm, a conclusive determination of the $I^{\text{total}}/I_0^{\text{total}}$ ratio through the 12 μm -thick porous TiO_2 thin film electrode simply by the XPS analysis is questionable. To clarify this issue, we used AES to analyze the cross section of a 22 μm -thick nanoporous TiO_2 layer with 10 cycles of ALD Al_2O_3 over-layer. The AES analysis showed that the variation of the Al(KLL) signal was less than 1.8% through the cross section, suggesting that the ALD Al_2O_3 layer was evenly deposited inside the porous electrode. This result suggests that using XPS to study the Al_2O_3 coverage on the nanoporous electrodes of DSSCs in terms of the C/S model is justified.

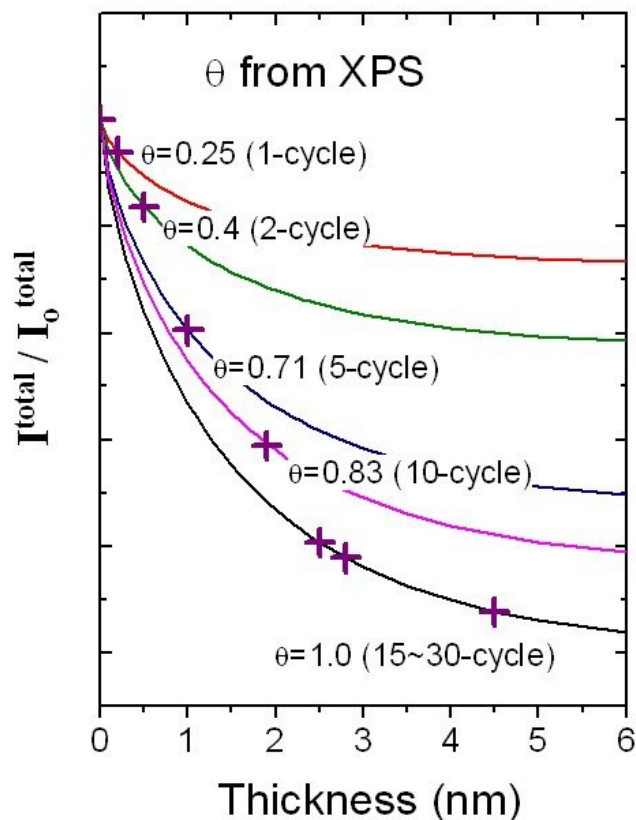


Figure 5.7 Coverages (θ) of Al_2O_3 shell layers on TiO_2 electrodes, obtained from XPS analyses. The experimental data (crosses) match the corresponding theoretical curves from our C/S model.

According to Fig. 5.7 the ALD deposition with one, two, five and 10 cycles results in a Al_2O_3 coverage of 0.25, 0.40, 0.71 and 0.83, respectively. However, the fitted coverage values are likely to have significant deviations from the true values because of several limitations bound to the application of the C/S model to the nanoporous DSSC electrodes. First, the C/S model assumes that the particle has a spherical shape. But the TiO_2 nanoparticles in the DSSC electrodes exhibit various rounding shapes, which are far from a perfect spherical geometry. Second, the C/S model considers only those photoelectrons emitting from nanoparticles in the direction perpendicular to the sample surface. Although the line of sight of the input lens of the electron energy analyzer is perpendicular to the sample surface and the distance between

the sample and the input aperture is considered to be infinitive compared with the nanoparticle diameter, detection of stray electrons emitting from other emission angles by the analyzer is inevitable. Third, the C/S model assumes a uniform island growth during the film deposition, that is, all islands developing on the substrate have the same thickness. However, this seems not to be true for the case of ALD- Al_2O_3 deposition on TiO_2 nanoparticles according to the TEM analysis. Each datum shown in Fig. 5.7 is the average value of 10 thickness measurements, and the average thickness will certainly deviate from the theoretical value for a particular coverage. Despite the above described limitations of the C/S model, Fig. 5.7 shows a reasonable trend in the coverage increase upon the increase in the number of ALD cycles. Therefore, we believe that the C/S model is applicable in the evaluation of the ALD- Al_2O_3 coverage.

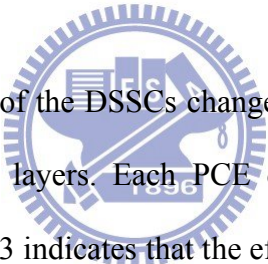


Figure 5.8 shows that the PCEs of the DSSCs changed upon varying the number of ALD reaction cycles of the Al_2O_3 shell layers. Each PCE datum in the figure is the average efficiency of 20 solar cells. Table 4-3 indicates that the efficiency increased initially by $\sim 13\%$ at an Al_2O_3 layer thickness of ca. 0.2 nm, but then it dropped dramatically to almost 0% upon further increasing the thickness. The initial increase of J_{sc} at ~ 0.2 -nm thickness of Al_2O_3 layer maybe attributed in part to the reduction of recombination [11, 12, 63]. On the other hand, the drop of the PCE is likely due to the tunneling effect [94], which will exponentially decrease the current from dye to TiO_2 electrode with increasing the thickness of Al_2O_3 overlayer as indicated by the short-circuit current (J_{sc}) listed in Table 4-3. The initial increase in the value of V_{oc} is suggested to result from that the high work function of the optimal ALD Al_2O_3 layer thickness, as discussed above, provided a positive built-in potential (eV_{bi}) at the Al_2O_3 - TiO_2 interface [53]. Thus, increasing the coverage of the optimal ALD Al_2O_3 overlayer on the nanoporous TiO_2 electrodes should enhance the PCE proportionally.

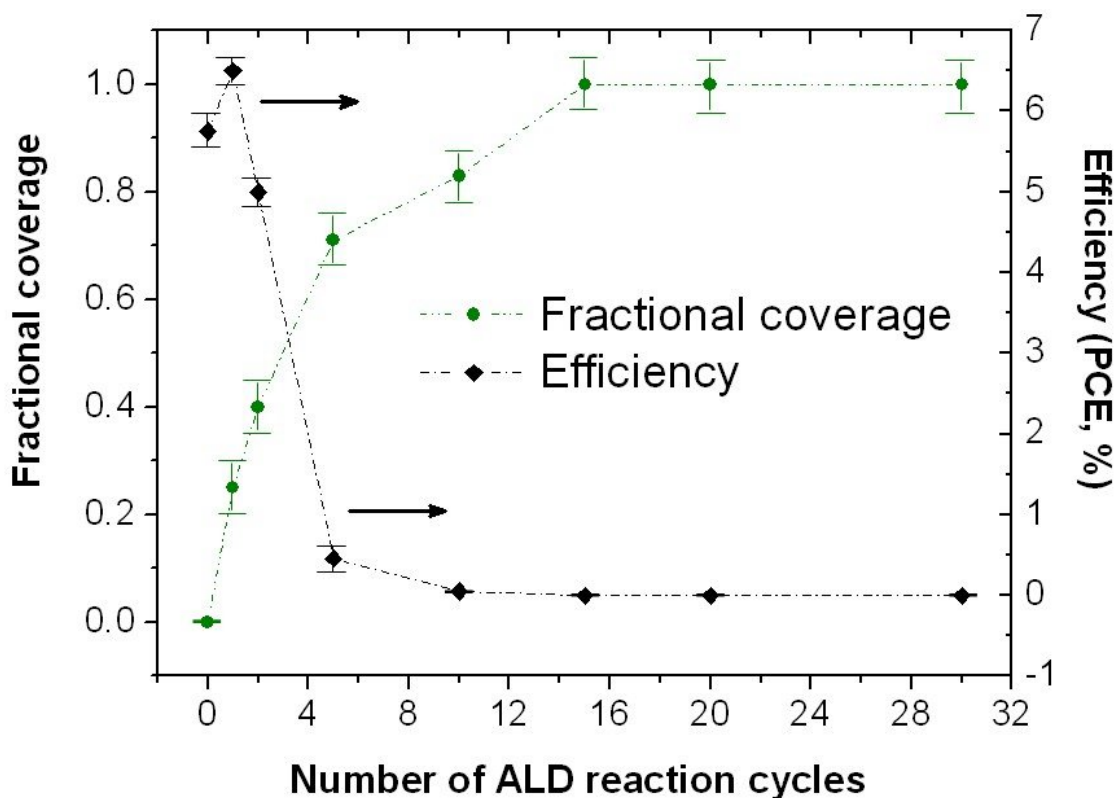


Figure 5.8 Changes in the PCE and coverage, plotted with respect to the number of ALD reaction cycles for Al₂O₃ shell layers on TiO₂ electrodes.

The optimal ALD Al₂O₃ layer thickness is one monolayer, or 0.2 nm, which is considerably thinner than the reported 0.9-2.5 nm thicknesses of Al₂O₃ films derived using sol-gel techniques [14, 63~65]. As discussed in previous studies [14, 66], the thickness of the sol-gel films can only be altered with a resolution down to ~1 nm, i.e., the minimum achievable Al₂O₃ thickness is ca. 1 nm. The poorer infiltrating ability of the liquid precursors during sol-gel processing, generally resulting in overestimation of the Al₂O₃ thickness (i.e., the sol-gel films may accidentally be thinner falling into the desirable range of Al₂O₃ layer thicknesses on electrode surfaces that are more difficult for the precursors to reach). Nevertheless, the ALD approach may not have much of an advantage over high-temperature sol-gel techniques, due in part to the low coverage of ALD Al₂O₃ overlayers on nanoporous

TiO₂ electrodes at the optimal over-layer thickness. Ideally, at the optimal thickness of the ALD Al₂O₃ overlayer, the PCE of the electrode is proportional to the fractional coverage of the overlayer. According to Fig. 5.8 and Table 4-3, the PCE is improved from 5.75% to 6.50% (i.e., an enhancement of 13.0%) if the nanoporous TiO₂ electrode is coated by the Al₂O₃ overlayer with a coverage of 0.25. Accordingly, as the coverage of the Al₂O₃ overlayer approaches one, the PCE of the electrode would have a PCE enhancement of more than 52%. However, under the present ALD deposition condition, the high PCE enhancement cannot be realized because of the island growth mode. If optimal ALD deposition conditions, such as the substrate temperature and precursor flow rate, can be successfully selected to increase the coverage for the first ALD deposition cycle, we believe that a better PCE for the ALD-Al₂O₃-TiO₂ C/S DSSCs is achievable.

5.4 Summary



We established a C/S model, using XPS electron spectroscopy data, to calculate the surface coverage of shell layers. A relation of the XPS signal of a nanoporous substrate featuring interconnected nanoparticles with the fractional coverage of the shell layer on the nanoparticles can be extracted from the model. We used the model to estimate the coverage of the ALD-Al₂O₃ shell layer deposited on the nanoporous TiO₂ electrodes of DSSCs as a function of the number of ALD reaction cycles. The coverage increased from 0.25 to 1.0 upon increasing the thickness of the Al₂O₃ shell layers, indicating the ALD-Al₂O₃ deposition on the nanoporous electrode was via the island growth mode. The PCE of the DSSCs was highest after the first ALD reaction cycle for the Al₂O₃ shell layers. On the basis of the coverage analysis, we predict that improvement in the PCE of ~52% is ideally obtainable when a single

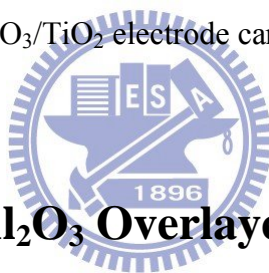
monolayer of ALD- Al_2O_3 (i.e. at the coverage of 1.0) deposited on the nanoporous TiO_2 electrode.



Chapter 6

Growth of Al₂O₃ Deposited on TiO₂ Electrodes of Dye-Sensitized Solar Cells

The ALD process may not provide much of an advantage over high-temperature sol-gel techniques because of the low coverage of ALD Al₂O₃ overlayers on nanoporous TiO₂ electrodes. This situation arises from the island-mode growth mechanism of the ALD Al₂O₃ overlayers, which can result in a low coverage of overlayers on nanoporous TiO₂ electrodes. Therefore, in this chapter, we are interested in investigating the growth mode and determining the optimal thickness of Al₂O₃ overlayers on the porous TiO₂ electrode so that the PCE of DSSCs featuring the Al₂O₃/TiO₂ electrode can be further optimized.

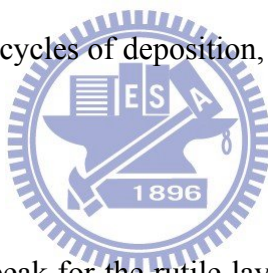


6.1 Deposition of the Al₂O₃ Overlayers

By using Al(CH₃)₃ and H₂O as the precursors, there are two consecutive stages for atomic layer depositing Al₂O₃ over-layers on a TiO₂ substrate: (1) aluminum hydroxide formation on the TiO₂ surface and (2) continuous Al₂O₃ growth. The first stage can be represented by the reactions (2-4) and (2-5). Likewise, the continuing growth of the Al₂O₃ overlayer can be summarized by the two consecutive reactions (2-6) and (2-7) [71]. According to the above reaction equations, at the end of each ALD reaction cycle, the sample is covered by hydroxyl surface groups.

We used XPS to study the change in the chemical state of surface species on the porous TiO₂ layers before and after the ALD reaction. Figure 6.1 shows the Ti 2P_{3/2} and the Al 2p

XPS spectra of the ALD- $\text{Al}_2\text{O}_3/\text{TiO}_2$ electrode layers as a function of the ALD reaction cycles. The XPS spectrum of the as-prepared porous TiO_2 layers shown in Fig. 6.1(a) indicates that the Ti $2p_{3/2}$ core level was located at 458.9 eV for the anatase layer and 458.8 eV for the rutile layer. Both the peak positions fall within the range reported for TiO_2 , which is between 458.8 and 459.4 eV [84]. Following the ALD process, the binding energy of the Ti $2p_{3/2}$ core level of the anatase layer first red-shifted to 458.4 eV at the first deposition cycle of the Al_2O_3 overlayer, and then gradually blue-shifted to 458.9 eV with increasing the cycle number up to 30-cycles. These shifts suggest that an interfacial reaction occurred on the anatase nanoparticles during the deposition of the ALD- Al_2O_3 overlayer. Evidence for this interfacial reaction on the anatase layer is more apparent in the Al 2p spectra shown in Figure 6.1(b). The Al 2p peak after one cycle of deposition was situated at 74.1 eV for the anatase layer, and the peak shifted to 74.7 eV after 30 cycles of deposition, which is consistent with the reported energy for Al_2O_3 [84].



On the other hand, the Al 2p peak for the rutile layer was situated around 74.1 eV after the first ALD cycle and varied little in the energy position through the 30 cycles of ALD- Al_2O_3 deposition. We have previously shown that the formation of Ti-O-Al(OH)_2 surface species in the anatase layer is the causes of these binding energy shifts [19, 53]. The Ti-O-Al(OH)_2 species are produced when TMA and H_2O react sequentially with the hydroxylated surface of the anatase nanoparticles as described by Eq. (2-5). Chemical structures of the type Ti-O-Al(OH)-O-Ti should also be formed on the sample surface during the initial stage of the ALD reaction, and they must be responsible for the energy shift of Ti $2p_{3/2}$ electrons as well.

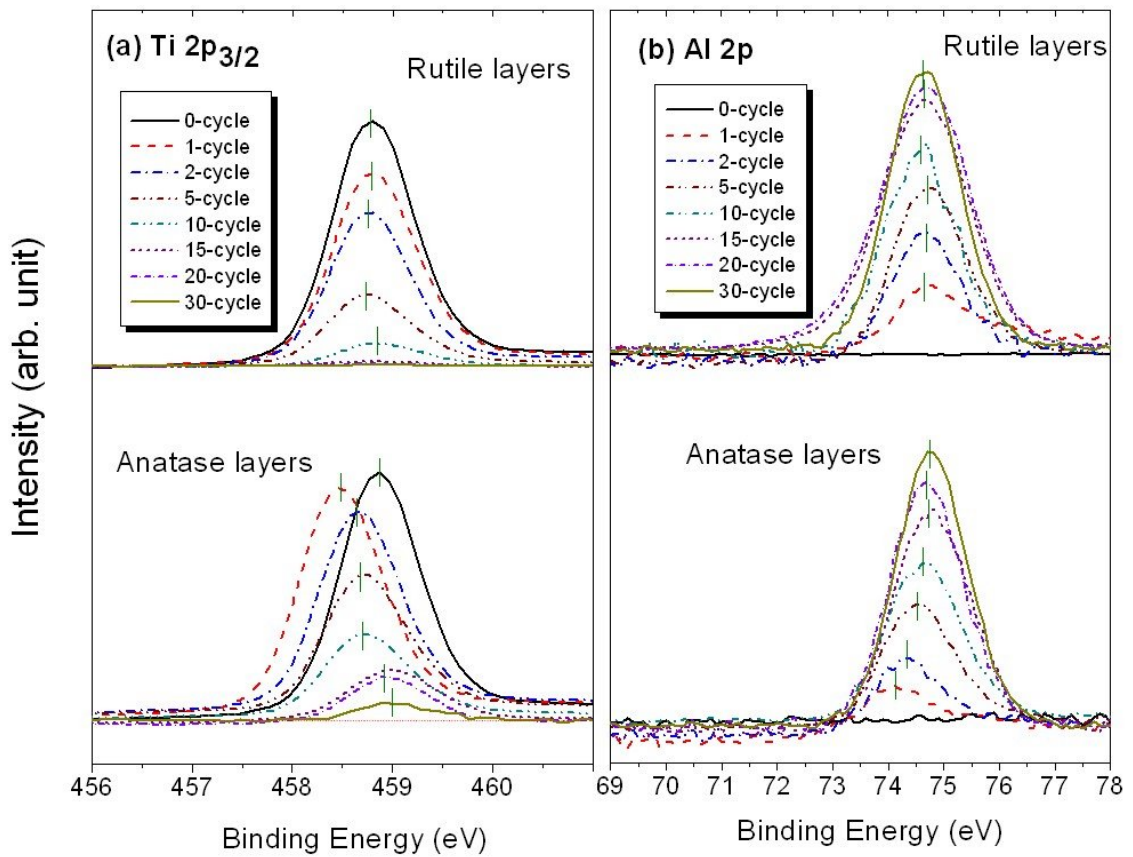


Figure 6.1 XPS data for the (a) Ti 2p_{3/2} and (b) Al 2p core level photoelectron peaks from ALD Al₂O₃-coated TiO₂ electrodes.

The TEM images in Fig. 6.2(a) and (b) show TiO₂ particles separated from the anatase and the rutile layers, respectively, featuring a 10-cycle ALD Al₂O₃ overlayer. These samples contain interconnected TiO₂ particles, which had a diameter of ca. 20 nm for the anatase layers and ca. 300 nm for the rutile layers. The presence of over-coated Al₂O₃ layers is evident in these TEM images. We used TEM to determine the average thicknesses of the ALD Al₂O₃ overlayers prepared with different ALD cycles (Table 6-1). Each thickness value listed in the table is the average value of ten TEM measurements at different locations on a TiO₂ particle. There was a significant discrepancy in the deposition rate (nm/cycle) for the two types of TiO₂ phases: that on the rutile particles (0.46–0.52 nm/cycle) were higher than that on anatase nanoparticles (0.14–0.25 nm/cycle).

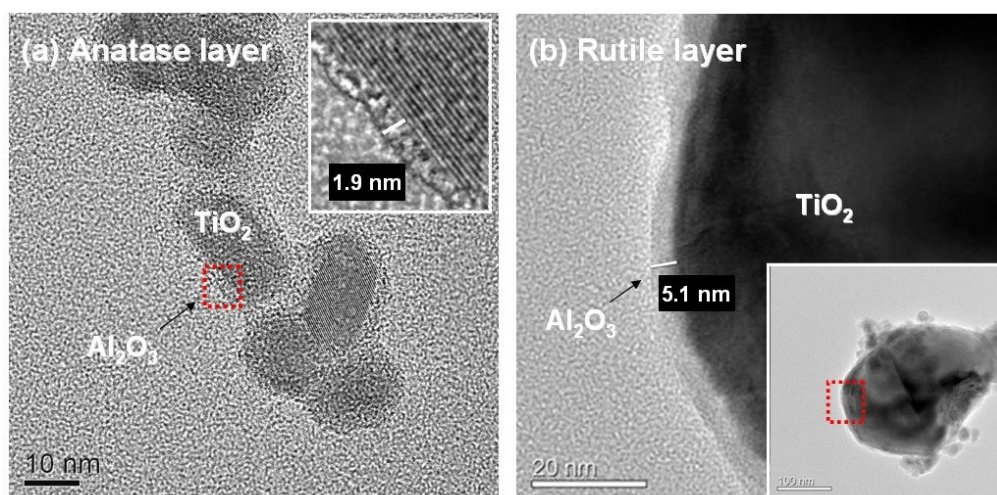


Figure 6.2 (a) TEM images of the anatase TiO_2 nanoparticles featuring a 10-cycle ALD Al_2O_3 overlayer. Inset in (a) shows the high-magnification image of a selected area of the marked area. (b) TEM images of the marked area of a rutile TiO_2 particles (shown in the inset) featuring a 10-cycle ALD Al_2O_3 overlayer.

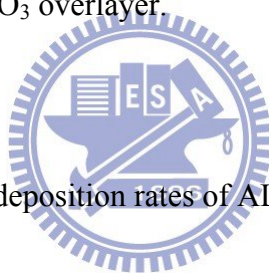


Table 6-1 Average thicknesses and deposition rates of ALD Al_2O_3 overlayers on TiO_2 electrodes.

Samples		0-	1-	2-	5-	10-	15-	20-	30-
		cycle	cycle	cycle	cycle	cycle	cycle	cycle	cycle
Anatase	Thickness (nm)	0	0.2	0.5	1	1.9	2.5	2.8	4.5
	Deposition rate (nm/cycle)	–	0.2	0.25	0.2	0.19	0.17	0.14	0.15
Rutile	Thickness (nm)	0	0.5	1	2.6	5.1	7.5	9.8	13.8
	Deposition rate (nm/cycle)	–	0.5	0.5	0.52	0.51	0.5	0.49	0.46

6.2 Growth-Per-Cycle of the Al₂O₃ Overlayers

The growth mode can be described in terms of the growth-per-cycle (ΔC_m) of the ALD Al₂O₃ layer, as defined using the following equation [81]:

$$\Delta C_m = \Delta h \times (\rho N_A / M) \quad (6-1)$$

where ΔC_m is the number of atom *m* (in this case, Al) adsorbed per unit surface area per cycle, Δh is the thickness increment per cycle, ρ is the density of the layer, N_A is the number of atoms per mole ($6.02214 \times 10^{23} \text{ mol}^{-1}$), and M is the molar mass of AlO_{1.5}. After substituting the values of M (50.98 g/mol) and ρ ($2.9 \times 10^{-21} \text{ g/nm}^3$) into equation 6-1 [68, 81], the growth-per-cycle (ΔC_{Al}) of the Al₂O₃ overlayer as a function of the number of ALD reaction cycles is shown in Figure 6.3. The growth-per-cycle increased to a maximum and then decreased to a steady value. This growth process is typical of substrate-inhibited growth of the ALD Al₂O₃ layer as reported by Puurunen [82]; island growth is the origin of this type of substrate-inhibited growth.

According to Figure 6.3, island growth on the rutile layer was less prevalent than on the anatase layer before 5 cycles of the ALD reaction, and layer-by-layer growth replaced island growth to become the main growth mode after 10 cycles of the ALD reaction on both types of TiO₂ particles.

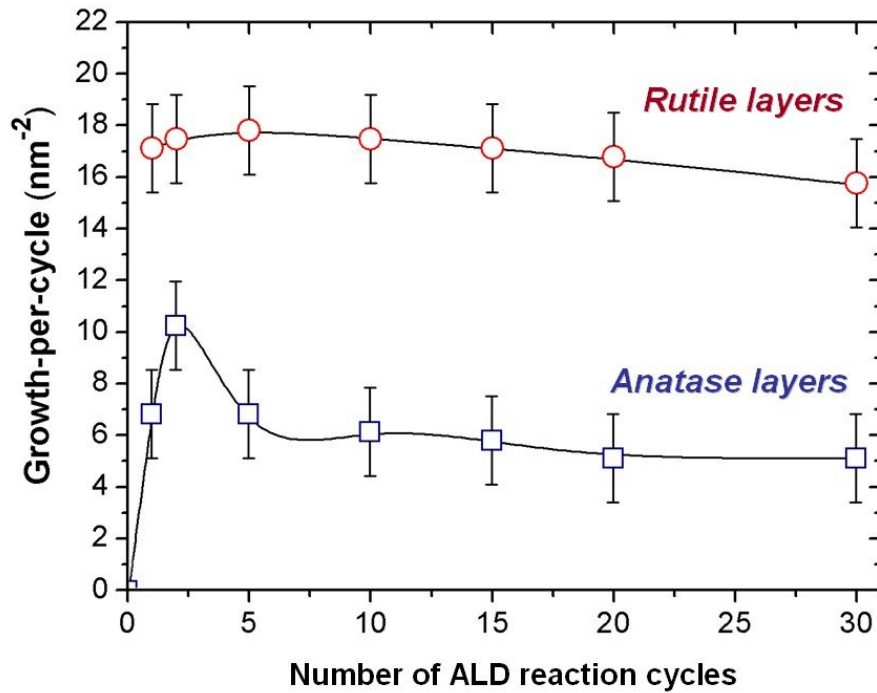


Figure 6.3 Growth-per-cycle of the Al₂O₃ overlayers as a function of the number of ALD reaction cycles.



Although the result of Figure 6.3 reveals that the growth mode changed from island growth to layer-by-layer growth on both porous TiO₂ electrode layers, it is still unclear why the growth mode transition occurred during the ALD process. According to a previous study [101], the transition of the growth mode is based on the surface energies of the substrate and the overlayer as described by the following formula:

$$\sigma_s < \sigma_o + \sigma_i + \sigma_{st} \quad (6-2)$$

$$\sigma_s > \sigma_o + \sigma_i + \sigma_{st} \quad (6-3)$$

where σ_s is the surface energy of the substrate, σ_o is the surface energy of the overlayer, σ_i is the interfacial energy, and σ_{st} is the accumulated strain energy. When σ_s is less than the sum

of σ_o , σ_l , and σ_{st} , film growth occurs in the island growth mode; when σ_s is greater than the sum of σ_o , σ_l , and σ_{st} , film growth occurs in layer-by-layer mode. Usually, the accumulated strain energy is the main factor to reverse the inequality in the formula.

6.3 Lattice Volumes of TiO₂ Electrodes

To study the effect of lattice strain on the transition in the Al₂O₃ growth mode, we used XRD to study the variation in lattice constants of the anatase and rutile layers as a function of the ALD reaction cycle. The XRD samples were prepared by depositing separately the anatase and the rutile layers on two different FTO glass substrates. Figure 6.4 shows the XRD spectra of the two samples over a scan range from 24 to 28°. The Bragg's angles of the (101) plane of standard anatase (JCPDS Card Number 21-1272) and the (110) plane of standard rutile (JCPDS Card Number 21-1276) are also provided as marked by the vertical dashed-dotted lines. When the thickness of the Al₂O₃ overlayers increased, the (101) diffraction peaks for the anatase sample shifted to lower angles, whereas the (110) diffraction peaks for the rutile sample remained unchanged. The diffraction peaks for both samples were located at higher angles than those of the standard samples, suggesting that the TiO₂ lattice might suffer from the stress of contraction. Table 6-2 lists the lattice constants and lattice volumes of the TiO₂ particles with respect to the number of the ALD Al₂O₃ deposition cycle. The lattice constant a of the anatase nanocrystals remained almost unchanged through the 30 cycles of ALD deposition, whereas the lattice constant c increased with the cycle number.

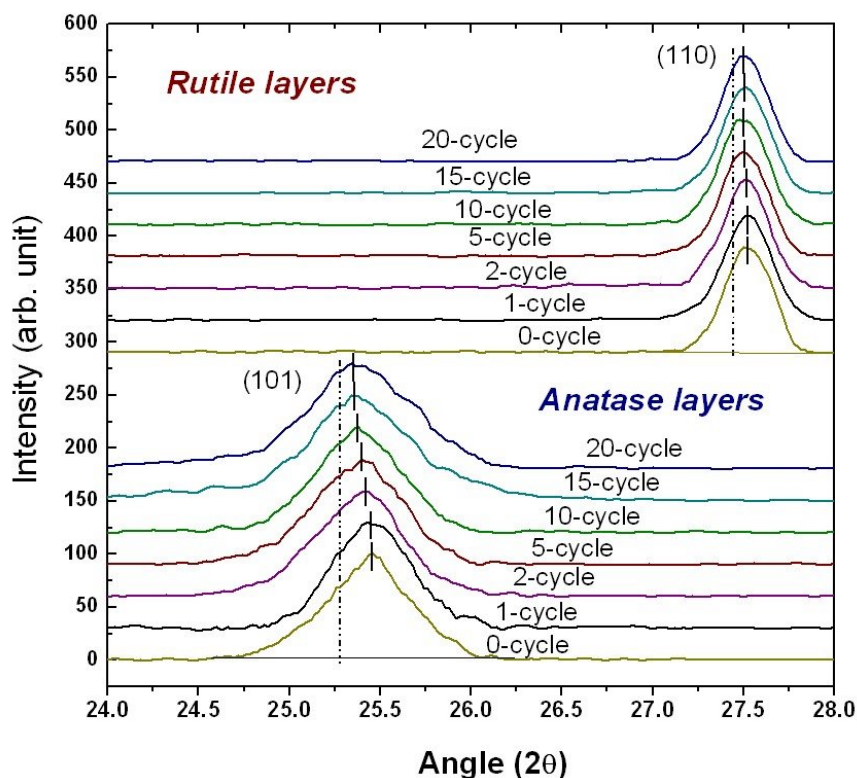


Figure 6.4 XRD spectra of the anatase electrode layer (a) and the rutile electrode layer (b) with respect to the number of ALD deposition cycles of the Al₂O₃ overlayer.

Table 6-2 Lattice constants and lattice volumes of TiO₂ electrodes for various numbers of ALD Al₂O₃ deposition cycles.

Sample		0- cycle	1- cycle	2- cycle	5- cycle	10- cycle	15- cycle	20- cycle
Anatase	Lattice constants <i>a/c</i> (Å)	3.77/ 9.41	3.78/ 9.44	3.77/ 9.46	3.78/ 9.47	3.77/ 9.49	3.77/ 9.51	3.77/ 9.51
	Lattice volume (Å ³)	134.3	134.9	135.0	135.3	135.4	135.5	135.7
Rutile	Lattice constants <i>a/c</i> (Å)	4.58/ 2.95	4.58/ 2.95	4.58/ 2.95	4.58/ 2.94	4.58/ 2.95	4.58/ 2.94	4.58/ 2.95
	Lattice volume (Å ³)	62.0	61.9	62.1	61.9	62.1	62.0	62.0

Based on the lattice constants derived from the XRD data, the lattice volume of the anatase and the rutile crystals as a function of the ALD cycle number is shown in Figure 6.5. The standard lattice volumes of the anatase and rutile phases (JCPDS data) are also provided as marked by the horizontal dashed-dotted lines. For the rutile electrode layer, the lattice volume varies little with respect to the ALD cycle number. On the other hand, the lattice volume of the anatase electrode layer increases with increasing the ALD cycle number until a saturated volume is reached at the 15th ALD reaction cycle. The difference between the saturated lattice volume of the anatase and rutile layers and the lattice volume of the corresponding standard TiO₂ phases can be attributed to the contractive stress induced by the oxygen deficiency of the TiO₂ particles [105~ 107]. Observing a large contractive strain in TiO₂ anatase nanocrystals, Li et al. [108] suggested that extensive surface hydration forming Ti-OH surface species was the primary reason why the anatase nanocrystals had a smaller lattice volume than their bulk phase. Likewise, in this study, Ti-OH surface groups on the as-prepared TiO₂ nanoparticles can induce lattice contraction in the nanoparticles. The island growth of the Al₂O₃ overlayer on the TiO₂ nanoparticles at the initial stage of the ALD deposition can be attributed to the large lattice strain as discussed above. The amount of the Ti-OH species on the anatase nanoparticles can be reduced through the ALD Al₂O₃ deposition, which produces Ti-O-Al(OH)₂ surface groups as described in Eq. (2-5). As a result, the strain energy of the anatase TiO₂ nanocrystals decreases upon increasing the number of the Al₂O₃ deposition cycle, leading to a transition from island growth to layer-by-layer growth, as revealed by Fig. 6.3. The large difference in the dependence of the lattice volume on the ALD cycle number between the anatase and the rutile electrode layers can be ascribed to the large difference in the surface to volume ratio. The contractive surface stress should primarily affect the surface lattice of a few atomic layers and, therefore, particles of larger size must have a smaller lattice contraction in the particles. Because the anatase nanoparticles have a

much smaller size (~ 20 nm) than the rutile particles (~ 200 - 400 nm), the surface hydration produces a larger surface stress on the anatase nanoparticles. In addition to the difference in the growth mode transition between the two TiO_2 electrode layers, the lattice contraction may also affect the ALD- Al_2O_3 deposition rate on the two layers. As discussed above, the Al_2O_3 deposition rate on the anatase layer is much smaller than that on the rutile layer before the tenth ALD cycle. Compared with the rutile particles, the anatase nanoparticles have a much larger contractive strain during the first few cycles of the ALD deposition, implying that the first few atomic layers of Al_2O_3 on the anatase nanoparticles are subject to a higher stress, and thus the deposition of these highly stressed atomic layers is energetically unfavorable. As a result, the ALD reaction rate is slower on the anatase nanoparticle than on the rutile particles, leading to a smaller Al_2O_3 deposition rate on the anatase electrode layer.

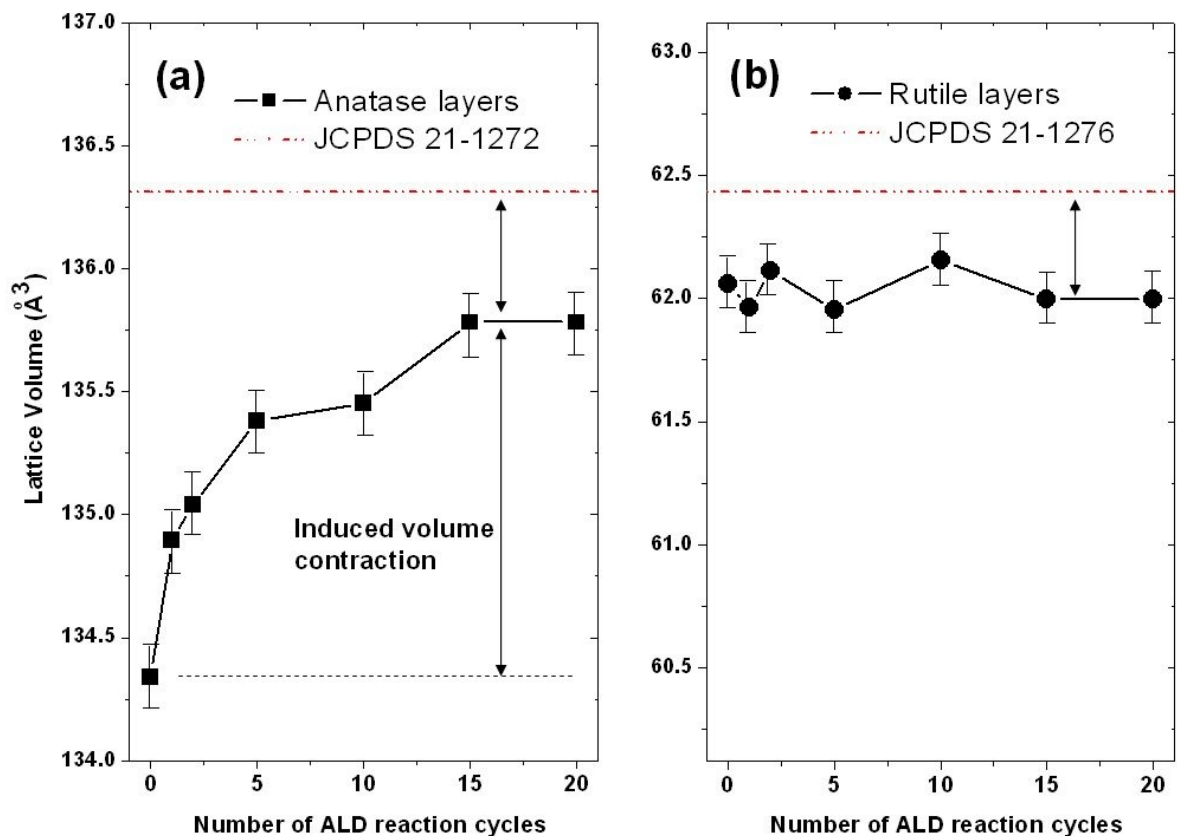


Figure 6.5 Lattice volumes of TiO_2 crystals in (a) the anatase and (b) in the rutile electrode layers, plotted with respect to the number of ALD reaction cycles of the Al_2O_3 overlayer.

According to our previous study, the DSSCs using the porous TiO₂ electrodes had a maximum PCE (6.6%) when the anatase nanoparticles was coated by the Al₂O₃ overlayer with a coverage of 0.25, which was achieved after the first ALD deposition cycle. The cause of the low coverage was ascribed to a result of the prevailing island growth mode during the ALD deposition. Island growth of the Al₂O₃ overlayer resulted in a low coverage and a non-uniform thickness of the overlayer, and thus greatly degraded the PCE of the DSSCs. Because the contractive strain increases with decreasing the size of TiO₂ particles, it is likely that we can obtain a better PCE for the DSSCs featuring the porous TiO₂ electrode if the size of the anatase nanoparticle is properly increased. When the size of the anatase nanoparticles is correctly chosen to minimize the surface contractive strain, we may obtain a uniform Al₂O₃ overlayer of higher coverage on the anatase electrode during the first ALD cycles, and thereby the DSSCs may exhibit a much better PCE performance compared with those using the present electrode structure featuring anatase nanoparticle of ~20 nm in size.



6.4 Summary

We have used a low-temperature (150°C) ALD process to grow ultra-thin Al₂O₃ overlayers on TiO₂ electrodes in dye-sensitized solar cells. Island growth on the anatase layers was more pronounced than on the rutile layers at the initial deposition stage, and layer-by-layer growth replaced island growth to become the main growth mode after the 5th ALD cycle. The origin of the island growth process is ascribed to the presence of the high surface stress resulting from surface hydration on the TiO₂ nanoparticle at the beginning of the ALD Al₂O₃ deposition. The island growth resulted in a non-uniform ALD Al₂O₃ overlayer of low coverage on the nanoporous TiO₂ electrodes during the first few ALD

reaction cycles. The study suggests that a better PCE of the DSSCs may be obtained if the size of anatase nanoparticles of the DSSC electrodes can be correctly chosen to minimize the surface lattice strain.



Chapter 7

Conclusions and Future Works

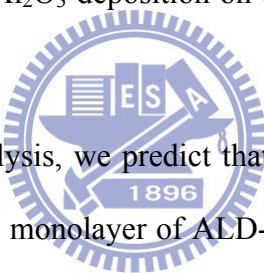
7.1 Conclusions

Ultra-thin Al_2O_3 films were deposited on nanoporous TiO_2 electrodes of dye-sensitized solar cells (DSSCs) by atomic-layer-deposition (ALD). The power conversion efficiency (PCE) of the DSSCs increases from 5.75% to 6.5%, an improvement of 13%, when the Al_2O_3 overlayer reaches an average thickness of ~ 0.2 nm. We investigated the energy level, surface coverage and growth mode of the ALD- Al_2O_3 overlayer on the core/shell electrodes and concluded the results as follows.

- a. The formation of Ti-O-Al(OH)_2 and interfacial dipole layers exhibited a strong influence on the work function of the Al_2O_3 overlayers, while the thicker Al_2O_3 overlayers caused the values of valence band maximum and band gap to approach the values associated with pure Al_2O_3 .
- b. A work function difference of 0.4 eV and a recombination barrier height of 0.1 eV were associated with the highest PCE achieved by the first monolayer of Al_2O_3 layer. Thicker Al_2O_3 overlayers, however, caused significant reduction of PCE with negative and increased interfacial energy barrier height between the N719 dyes and TiO_2 electrodes.
- c. We found that the paths of electron transfer from dye into TiO_2 without any energy barrier and therefore improve the cells PCE due to the proper ultra-thin Al_2O_3 energy levels. The PCE of the DSSCs may correlates with work function difference, recombination barrier height, and interfacial barrier height resulting from various thicknesses of the Al_2O_3 overlayers and that interfacial reactions, such as the

formation of Ti-O-Al(OH)₂ and dipole layers, play an important role in determining the interfacial energy levels required to achieve optimal performance of dye-sensitized TiO₂ solar cells.

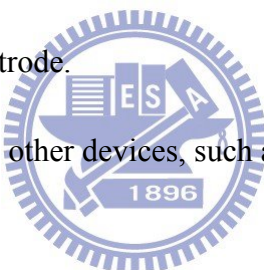
- d. We established a core/shell (C/S) model which evaluates the surface coverage of an overlayer deposited on nanoparticles in terms of X-ray photoelectron spectroscopy signals of the nanoparticles. We used the model to estimate the coverage of Al₂O₃ shell layers, which were deposited on the nanoporous TiO₂ electrodes of dye sensitized solar cells (DSSCs) by atomic layer deposition (ALD), as a function of the number of ALD reaction cycles.
- e. The coverage increased from 0.25 to 1.0 upon increasing the thickness of the Al₂O₃ shell layers, indicating the ALD-Al₂O₃ deposition on the nanoporous electrode was via the island growth mode.
- f. On the basis of the coverage analysis, we predict that improvement in the PCE of ~52% is obtainable when a single monolayer of ALD-Al₂O₃ (i.e. at the coverage of 1.0) deposited on the nanoporous TiO₂ electrode.
- g. The growth mode of the ALD-Al₂O₃ overlayers is changed from island growth to layer-by-layer growth after the first 5 ALD reaction cycles, and the growth mode transition is much more pronounced for the anatase electrode layer.
- h. We suggest that the growth transition of ALD-Al₂O₃ overlayers is correlated with the reduction in the lattice strain of the TiO₂ nanoparticles.
- i. The contractive lattice strain in the hydroxylated TiO₂ nanoparticles is progressively decreased during the ALD Al₂O₃ deposition, resulting in the growth mode transition.



7.2 Future Works

The study has clearly confirmed the fact that the energy level, surface coverage and growth mode of the core/shell electrodes play three important roles to enhance the efficiency of DSSCs. However, we may not complete the whole research of these topics. Some suggestions are listed below for future works

- a. The interfacial energy levels at electrolyte/dye/shell/core interfaces should be further studied.
- b. The mechanism of formation of dipole layers at electrolyte/dye/shell/core interfaces is important to investigate
- c. Multi-shells and sintering model should be established for evaluating the coverage of electrolyte/dye/shell/core electrode.
- d. The coverage model may apply to other devices, such as the electrode of Li-battery or quantum-dot solar cell.
- e. Other kind of core/shell electrodes should be developed with the same analysis of the energy level, surface coverage and growth mode to enhance the efficiency of DSSCs.
- f. The accuracy of the coverage and the energy levels measurements need to be confirmed. If the coverage in this study is confirmed to be less than 1, the energy levels should be modified accordingly.



References

1. *Energy in Japan 2010*, p13, published by Agency for Natural Resources and Energy, Japan.
2. 田大昌, 材料世界網, **7**, 28, (2010).
3. M. Grätzel, *Inorg. Chem.*, **44**, 6841 (2005).
4. 田大昌, 材料世界網, **8**, 27, (2008).
5. M. Grätzel, *Nature*, **414**, 338 (2001).
6. A. Hagfeldt, G. Boschloo, L. Sun, L. Kloo, H. Petterson, *Chem. Rev.*, **110**, 6595 (2010).
7. 童永樑, 工業材料雜誌, **285**, 156 (2010).
8. C. M. Elliott, *Nature Chem.*, **3**, 188 (2011).
9. DSSC Technology Trend and Market Forecast (2008~2015), Solar & Energy co. press, (2011).
10. B. O'Regan, M. Grätzel, *Nature*, **353**, 737 (1991).
11. A. Zaban, S. G. Chen, S. Chappel, B. A. Gregg, *Chem. Commun.*, 2231 (2000).
12. S. G. Chen, S. Chappel, Y. Diamant, A. Zaban, *Chem. Mater.*, **13**, 4629 (2001).
13. Z. S. Wang, C. H. Huang, Y. Y. Huang, Y. J. Hou, P. H. Xie, B. W. Zhang, H. M. Cheng, *Chem. Mater.*, **13**, 678 (2001).
14. E. Palomares, J. N. Clifford, S. A. Haque, T. Lutz, J. R. Durrant, *Chem. Commun.*, 1464 (2002).
15. E. Palomares, J. N. Clifford, S. A. Haque, T. Lutz, J. R. Durrant, *J. Am. Chem. Soc.*, **125**, 475 (2002).
16. Z. S. Wang, M. Yanagida, K. Sayama, H. Sugihara, *Chem. Mater.*, **18**, 2912 (2006).
17. S. Wu, H. Han, Q. Tai, J. Zhang, S. Xu, C. Zhou, Y. Yang, H. Hu, B. Chen, B. Sebo, X. Z. Zhao, *Nanotechnology*, **19**, 215704 (2008).
18. R. H. Lee, Y. W. Huang, *Thin Solid Films*, 517, 5903 (2009).

19. C. Lin, F. Y. Tsai, M. H. Lee, C. H. Lee, T. C. Tien, L. P. Wang, S. Y. Tsai, *J. Mater. Chem.*, **19**, 2999 (2009).
20. M. Shanmugam, M. F. Baroughi, D. Galipeau, *Thin Solid Films*, **518**, 2678 (2010).
21. V. Ganapathy, B. Karunakaran, S. W. Rhee, *J. Power Sources*, **195**, 5138 (2010).
22. M. Shanmugam, B. Bills, M. F. Baroughi, *Mater. Res. Soc. Symp. Proc.*, **1260**, 5 (2010).
23. J. T. Kim, S. H. Kim, *Sol. Energy Mater. Sol. Cells*, **95**, 336 (2010).
24. G. R. R. A. Kummara, K. Tennakone, V. P. S. Perera, A. Konno, S. Kaneko, M. Okuya, *J Phys. D*, **34**, 868 (2001).
25. A. Kay, M. Grätzel, *Chem. Mater.*, **14**, 2930 (2002).
26. N. G. Park, M.G. Kang, K. M. Kim, K. S. Ryu, S. H. Chang, *Langmuir*, **20**, 4246 (2004).
27. Z. Liu, K. Pan, M. Liu, M. Wang, Q. Lu, J. Li, Y. Bai, T. Li, *Electrochim. Acta*, **50**, 2583 (2005).
28. E. Ramasamy, J. Lee, *J. Phys. Chem.*, **114**, 22032 (2010).
29. H. J. Snaith, C. Ducati, *Nano Lett.*, **10**, 1259 (2010).
30. C. Prasittichai, J. T. Hupp, *J. Phys. Chem. Lett.*, **1**, 1611 (2010).
31. K. A. T. A. Perera, S. G. Anuradha, G. R. A. Kumara, M. L. Paranawitharana, R. M. G. Rajapakse, H. M. N. Bandara, *Electrochim. Acta*, doi: 10.1016/j.electacta. 2011.01.110 (2011).
32. Y. J. Shin, K. S. Kim, N. G. Park, K. S. Ryu, S. H. Chang, *Bull. Korean Chem. Soc.*, **26**, 1929 (2005).
33. Y. J. Shin, J. S. Lee, J. H. Park, N. G. Park, *Chem. Lett.*, **36**, 1506 (2007).
34. Y. Y. Xi, Y. F. Hsu, A. B. Djurisic, W. K. Chan, *J. Electrochem. Soc.*, **155**, D595 (2008).
35. S. Ueno, S. Fujihara, *Eur. J. Inorg. Chem.*, 2165 (2010).
36. K. Park, Q. Zhang, B. B. Garcia, X zhou, Y. H. Jeong, G. Cao, *Adv. Mater.*, **22**, 2329 (2010).

37. S. Ueno, S. Fujihara, *Electrochim. Acta*, **56**, 2906 (2011).
38. H. Lia, Y. Liana, X. Wanga, W. Maa, L. Zhaob, *Energy*, **36**, 1785 (2011).
39. <http://rredc.nrel.gov/solar/spectra/am1.5>
40. M. Grätzel, *Acc. Chem. Res.*, **42**, 1788 (2009).
41. V. Shrotriya, G. Li, Y. Yao, T. Moriarty, K. Emery, Y. Yang, *Adv. Funct. Mater.*, **16**, 2016 (2006).
42. H. Vogel, *Photogr. Sci. Eng.*, **18**, 35 (1874).
43. J. Moser, *Monatsh. Chem.*, **8**, 373 (1887).
44. H. Meier, *J. Phys. Chem.*, **69**, 719 (1965).
45. H. Tributsch, M. Calvin, *Photochem. Photobiol.*, **17**, 95 (1971).
46. H. Gerischer, *Photochem. Photobiol.*, **16**, 243 (1972).
47. C. W. Tang, *Appl. Phys. Lett.*, **48**, 183 (1986).
48. C. Y. Chen, M. Wang, J. Y. Li, N. Pootrakulchote, L. Alibabaei, C. H. Ngoc-le, J. D. Decoppet, J. H. Tsai, C. Grätzel, C. G. Wu, S. M. Zakeeruddin and M. Grätzel, *ACS Nano*, **3**, 3103 (2009).
49. M. Grätzel, *Acc. Chem. Res.*, **42**, 1790 (2009).
50. N. J. Cherepy, G. P. Smestad, M. Gratzel, J. Z. Zhang, *J. Phys. Chem. B*, **101**, 9342 (1997).
51. Q. Dai, J. Rabani, *New J. Chem.*, **26**, 421 (2002).
52. I. Hod, M. Shalom, Z. Tachan, S. Ruhle, A. Zaban, *J. Phys. Chem. C*, **114**, 10015 (2010).
53. T. C. Tien, F. M. Pan, L. P. Wang, C. H. Lee, Y. L. Tung, S. Y. Tsai, C. Lin, F. Y. Tsai, S. J. Chen, *Nanotechnology*, **20**, 305201 (2009).
54. Q. Zhang, G. Cao, *Nano Today*, **6**, 91 (2011).
55. Y. Diamant, S. Chappel, S. G. Chen, A. Zaban, *Coordin. Chem. Rev.*, **248**, 1271 (2004).
56. A. Hagfeldt, M. Grätzel, *Chem. Rev.*, **95**, 49 (1995).

57. B. B. Ma, R. Gao, L. D. Wang, Y. F. Zhu, Y. T. Shi, Y. Geng, H. P. Dong, Y. Qiu, *Sci. China Chem.*, **53**, 1669 (2010).
58. P. Wang, L. D. Wang, B. B. Ma, B. Li, Y. Qiu, *J Phys Chem B*, **110**, 14406 (2006).
59. B. B. Ma, F. Luo, L. D. Wang, X. M. Wu, C. Zhan, Y. S. Qiu, *Jpn J App Phys*, **46**(12), 7745 (2007).
60. G. Ramakrishna, A. K. Singh, D. K. Palit, H. N. Ghosh, *J Phys Chem B*, **108**, 1701 (2004).
61. D. Menzies, Q. Dai, Y. B. Cheng, G. P. Simon, L. Spiccia, *Mater. Lett.*, **59**, 1893, (2005).
62. S. J. Roh, R. S. Mane, S. K. Min, W. J. Lee, C. D. Lokhande, S. H. Han, *Appl. Phys. Lett.*, **89**, 253512 (2006)
63. S. Chappel, S. G. Chen, A. Zaban, *Langmuir*, **18**, 3336 (2002).
64. S. Ito, N. L. C. Ha, G. Rothenberger, P. Liska, P. Comte, S. M. Zakeeruddin, P. Péchy, M. K. Nazeeruddin, M. Grätzel, *Chem. Commun.*, 4004 (2006).
65. S. A. Haque, E. Palomares, H. M. Upadhyaya, L. Otley, R. J. Potter, A. B. Holmes, J. R. Durrant, *Chem. Commun.*, 3008 (2003).
66. K. M. P. Bandaranayake, S. M. K. Indika, W. P. Prasad, K. Tennakone, *Coord. Chem. Rev.*, **248**, 1277 (2004).
67. M. Scharrer, X. Wu, A. Yamilov, H. Cao, R. P. H. Chang, *Appl. Phys. Lett.*, **86** 151113 (2005).
68. M. D. Groner, F. H. Fabreguette, J. W. Elam, S. M. George, *Chem. Mater.*, **16**, 639 (2004).
69. M. Ritala, M. Leskelä, *Nanotechnology*, **10**, 19 (1999).
70. L. Niinistö, J. Päiväsaari, J. Niinistö, M. Putkonen, M. Nieminen, *Phys. Stat. Sol. (a)*, **201**, 1443 (2004).
71. C. A. Wilson, R. K. Grubbs, S. M. George, *Chem. Mater.*, **17**, 5625 (2005).

72. S. Y. Huang, G. Schlichthorl, A. J. Nozik, M. Graetzel, A. J. Frank, *Phys. Chem. B*, **101**, 2576 (1997).
73. G. Liu, W. Jaegermann, J. He, V. Sundstrom, L. Sun, *J. Phys. Chem. B*, **106**, 5814 (2002).
74. J. H. Snook, L. A. Samuelson, J. Kumar, Y. G. Kim, J. E. Whitten, *Organic Electron.*, **6**, 55 (2005).
75. F. D. Angelis, S. Fantacci, A. Selloni, *Nanotechnology*, **19**, 424002 (2008).
76. H. Ishii, K. Sugiyama, E. Ito, K. Seki, *Adv. Mater.*, **8**, 605 (1999).
77. W. Song, M. Yoshitake, *Appl. Surf. Sci.*, **251**, 14 (2005).
78. H. Lindstrom, H. Rensmo, S. Sodergren, A. Solbrand, S. E. Lindquist, *J. Phys. Chem. B*, **100**, 3084 (1996).
79. M. K. Nazeeruddine, A. Kay, I. Rodicio, R. Humphry-Baker, E. Muller, P. Liska, N. Vlachopoulos, M. Graetzel, *J. Am. Chem. Soc.*, **115**, 6382 (1993).
80. T. C. Tien, F. M. Pan, L. P. Wang, F. Y. Tsai, C. Lin, *J. Phys. Chem. C*, **114**, 10048 (2010).
81. R. L. Puurunen, *Chem. Vap. Deposition*, **9**, 327 (2003).
82. R. L. Puurunen, W. Vandervorst, *J. Appl. Phys.*, **96**, 7686 (2004).
83. G. Liu, W. Jaegermann, J. He, V. Sundstrom, L. Sun, *J. Phys. Chem. B*, **106**, 5814 (2002).
84. J. F. Moulder, W. F. Stickle, P. E. Sobol, K. D. Bomben, *Handbook of X-ray Photoelectron Spectroscopy*, Perkin-Elmer Press: Eden Prairie, MN, 45-73 (1962).
85. A. J. Gonzalez, D. Schmeisser, *Surf. Sci.*, **250**, 59 (1991).
86. W. Song, M. Yoshitake, *Surf. Interf. Anal.*, **38**, 793 (2006).
87. T. Toyoda, I. Tsuboya, *Rev. Sci. Instrum.*, **74**, 782 (2003).
88. D. D. Claudio, A. R. Phani, S. Santucci, *Optical Materials*, **30**, 279 (2007).
89. P. J. Potts, *A Handbook of Silicate Rock Analysis*, Chapman & Hall press, p.336 (1987).
90. B. Ealet, M. H. Elyakhloufi, E. Gillet, M. Ricci, *Thin Solid. Film*, **250**, 92 (1994).

91. I. Costina, R. Franchy, *Appl. Phys. Lett.*, **78**, 4139 (2001).
92. M. Brause, S. Skordas, V. Kempter, *Surf. Sci.*, **445**, 224 (2000).
93. F. D. Angelis, S. Fantacci, A. Selloni, *Nanotechnology*, **19**, 424002 (2008).
94. S. M. Sze, *Physics of Semiconductor Devices*, John Wiley & Son press, p97 (1983).
95. D. A. Neamen, *Semiconductor Physics and Devices*, McGraw-Hill press p349~p358 (2003).
96. J. Zhang, A. Zaban, *Electrochimica Acta.*, **53**, 5670 (2008).
97. J. N. Gillet, M. Meunier, *J. Phys. Chem. B*, **109**, 8733 (2005).
98. J. E. Martin, A. A. Herzing, W. Yan, X. Q. Li, B. E. Kobel, C. J. Kiely, W. X. Zhang, *Langmuir*, **24**, 4329 (2008).
99. O. Renault, R. Marlier, N. T. Barrett, E. Martinez, T. Baron, M. Gely, B. De Salvo, *Surf. Interface Anal.*, **38**, 486 (2006).
100. M. Mohai, I. Bertoti, *Surf. Interface Anal.*, **36**, 805 (2004).
101. Z. Sitar, L. L. Smith, R. F. Davis, *J. Crystal Growth*, **141**, 11 (1994).
102. S. Tanuma, C. J. Powell, D. R. Penn, *Surf. Interface Anal.*, **11**, 577 (1988).
103. E. E. Underwood, *Quantitative Stereology*, Addison-Wesley publication: Massachusetts, 178 (1962).
104. L. G. Gosset, J. F. Damlencourt, O. Renault, D. Rouchon, P. Holliger, A. Ermolieff, I. Trimaille, J. J. Ganem, F. Martin, M. N. Semeria, *J. Non-Cryst. Solids*, **303**, 17 (2002).
105. P. P. Ahonen, E. I. Kauppinen, *J. Mater. Res.*, **14**, 3938 (1999).
106. J. C. Parker, R. W. Siegen, *J. Mater. Res.*, **5**, 1246 (1990).
107. E. H. Poniatowski, R. R. Talavera, M. C. Heredia, O. C. Corona, R. A. Murillo, *J. Mater. Res.*, **9**, 2102 (1994).
108. G. Li, L. Li, J. Boerio-Goates, F. Woodfield, *J. Am. Chem. Soc.*, **127**, 8659 (2005).

Vita

- 基本資料

姓名：田大昌

性別：男

出生年月：民國 57 年 10 月

電子信箱：tien@itri.org.tw



- 學歷

國立交通大學材料科學與工程學研究所博士班(2004.9~2011.6)

國立台灣大學材料科學與工程學研究所碩士班(1992.9~1994.6)

國立台灣大學地質學系(1988.9~1992.6)

- 經歷

工研院材料所副研究員(1994~1999)

工研院材料所研究員(1999~至今)

工研院奈米中心兼任技術經理(2007~2011)

美國化學學會 Langmuir、ACS Appl. Mater. Interfaces 期刊評論員
(2009~至今)

- 專長：介面能階分析、核/殼材料覆蓋率分析、薄膜化態分析等。

- 著作

- 國際期刊論文

1. T. C. Tien, F. M. Pan, L. P. Wang, F. Y. Tsai, C. Lin, Coverage analysis for the core/shell electrode of dye-sensitized solar cells, *J. Phys. Chem. C*, **114**,

- 10048 (2010).
2. T. C. Tien, L. C. Lin, L. S. Lee, C. J. Hwang, S. Maikap, Y. Shulga, Analysis of weakly bonded oxygen in HfO₂/SiO₂/Si stacks by using HRBS and ARXPS, *J. Mater. Sci.: Mater. Electron.*, **21**, 475 (2010).
 3. A. Das, S. Maikap, C. H. Lin, P. J. Tzeng, T. C. Tien, T. Y. Wang, L. B. Chang, J. R. Yang, M. J. Tsai, Ruthenium oxide metal nanocrystal capacitors with high-k dielectric tunneling barriers for nanoscale nonvolatile memory device applications, *Microelectronic Engineering*, **87**, 1821 (2010).
 4. T. C. Tien, F. M. Pan, L. P. Wang, C. H. Lee, Y. L. Tung, S. Y. Tsai, C. Lin, F. Y. Tsai, S. J. Chen, Interfacial energy levels and related properties of atomic-layer-deposited Al₂O₃ films on nanoporous TiO₂ electrodes of dye-sensitized solar cells, *Nanotechnology*, **20**, 305201 (2009).
 5. C. P. Chen, T. C. Tien, B. T. Ko, Y. D. Chen, C. Ting, Energy level alignment at the anode of poly(3-hexylthiophene)/fullerene-based solar cells, *ACS Appl. Mater. Interfaces*, **1**(4), 741 (2009).
 6. T. M. Chen, J. Y. Hung, F. M. Pan, L. Chang, S. C. Wu, T. C. Tien, Pulse electrodeposition of iridium oxide on silicon nanotips for field emission study, *J. Nanosci. Nanotech.*, **9**(5), 3264 (2009).
 7. C. Lin, F. Y. Tsai, M. H. Lee, C. H. Lee, T. C. Tien, L. P. Wang, S. Y. Tsai, Enhanced performance of dye-sensitized solar cells by an Al₂O₃ charge-recombination barrier formed by low-temperature atomic layer deposition, *J. Mater. Chem.*, **19**, 2999 (2009).
 8. S. Maikap, A. Das, T. Y. Wang, T. C. Tien, L. B. Chang, High-k HfO₂ Nanocrystal Memory Capacitors Prepared by Phase Separation of Atomic-Layer-Deposited HfO₂/Al₂O₃ Nanomixtures, *J. Electrochem. Soc.*, **156**, 3, K28 (2009).
 9. S. Maikap, S. Z. Rahaman, T. C. Tien, Nanoscale nonvolatile memory

- characteristics using n-Si/SiO₂/HfAlO nanocrystal/Al₂O₃/Pt capacitors, *Nanotechnology*, **19**, 435202 (2008).
10. Y. M. Shulga, T. C. Tien, C. C. Huang, S. C. Lo, V. E. Muradyan, N. F. Polyakova, Y. C. Ling, R. O. Loutfy, A. P. Moravsky, XPS study of fluorinated carbon multi-walled nanotubes, *J. Electron Spectroscopy*, **160**, 22 (2007).
 11. S. Maikap, T. Y. Wang, P. J. Tzeng, T. C. Tien, L. S. Lee, J. R. Yang, M. J. Tsai, Band offsets and charge storage characteristics of atomic layer deposited high-k HfO₂/TiO₂ multilayers, *Appl. Phys. Lett.*, **90**, 262901 (2007).
 12. S. Maikap, P. J. Tzeng, H. Y. Lee, C. C. Wang, T. C. Tien, L. S. Lee, M. J. Tsai, Physical and electrical characteristics of atomic layer deposited TiN nanocrystal memory capacitors, *Appl. Phys. Lett.*, **91**, 043114 (2007).
 13. W. H. Tuan, T. C. Tien, Effect of addition of a small amount of silver on the microstructure and mechanical properties of YBa₂Cu₂O_{7-x}, *Mater. Chem. Phys.*, **39**, 72 (1994).
 14. W. H. Tuan, T. C. Tien, Mechanical performance of YBa₂Cu₃O_{7-x}-Ag composites, *J. Mater. Sci. Lett.*, **13**, 1019 (1994).

➤ 研討會論文

1. Ta-Chang Tien, Yu-Ming Wang, Jun-Chin Liu, C. S. Chou, New development in nanotechnology for solar cells, International nanotechnology exhibition and conference (Nano Tech 2010).
2. Ta-Chang Tien, Fu-Ming Pan, Lih-Ping Wang, Song-Yeu Tsai, Ching Lin,

- Feng-Yu Tsai, 染料敏化太陽電池之殼/核電極之覆蓋率模型, 奈米元件技術研討會 (SNDT 2010).
3. Lih-Ping Wang, Ta-Chang Tien, Fu-Ming Pan, Song-Yeu Tsai, Ching Lin, Feng-Yu Tsai, 氧化鋁於染料敏化太陽能電池 ALD 成長分析, 奈米元件技術研討會 (SNDT 2010).
4. Ta-Chang Tien, Lih-Ping Wang, Chia-Hua Lee, Yung-Liang Tung, Song-Yeu Tsai, Ching Lin, Feng-Yu Tsai and Su-Jen Chen, 能帶對準在染料敏太電之 ALD $\text{Al}_2\text{O}_3/\text{TiO}_2$ 電極之研究, 第十三屆奈米工程暨微系統研討會 (2009).
5. Ta-Chang Tien, Fu-Ming Pan, Chi-Chen Huang, Lih-Ping Wang, Chia-Hua Lee, Chih-Ping Chen, Energy Level Alignment in Organic Solar Cells using Electron Spectroscopy, 表面特性分析在奈米科技和材料研發的現況與進展研討會 (2008).
6. Lih-Ping Wang, Ta-Chang Tien, Chia-Hua Lee, Ching Lin, Feng-Yu Tsai, Yung-Liang Tung, Song-Yeu Tsai, Thickness dependence of energy levels for ultrathin Al_2O_3 -coated TiO_2 mesoporous films, 中國化學會年會 (2008).

